Influence of Microstructure on Mechanical Properties and Damage Initiation of Bainitic Steels in Railway Applications

Hajizad, O.

DOI
10.4233/uuid:06d15862-66ba-4872-95c8-76c2a3361a72

Publication date
2021

Document Version
Final published version

Citation (APA)
Hajizad, O. (2021). *Influence of Microstructure on Mechanical Properties and Damage Initiation of Bainitic Steels in Railway Applications*. [Dissertation (TU Delft), Delft University of Technology]. https://doi.org/10.4233/uuid:06d15862-66ba-4872-95c8-76c2a3361a72

Important note
To cite this publication, please use the final published version (if applicable).
Please check the document version above.

Influence of Microstructure on Mechanical Properties and Damage Initiation of Bainitic Steels in Railway Applications

Dissertation

for the purpose of obtaining the degree of doctor
at Delft University of Technology
by the authority of the Rector Magnificus Prof.dr.ir. T.H.J.J van der Hagen,
chair of the Board for Doctorates
to be defended publicly on
Tuesday 15 June 2021 at 10:00 o'clock

by

Omid HAJIZAD

Master of Science in Computational Mechanics,
Technical University of Munich, Germany
born in Urmia, Iran

This dissertation has been approved by the promoters.

Composition of the doctoral committee:

Rector Magnificus,	chairperson
Prof.dr. Z. Li	Delft University of Technology, promoter
Prof.dr.ir. R.P.B.J. Dollevoet	Delft University of Technology, promoter

Independent members:

Prof.dr.ir. J. Sietsma	Delft University of Technology
Prof.dr.ir. R.H. Petrov	Ghent University, Delft University of Technology
Prof.dr.ir. H.E.J.G. Schlangen	Delft University of Technology
Prof.dr. H. Li	University of Wollongong, Australia
Dr. I.Y. Shevtsov	ProRail B.V., Netherlands

This doctoral research has been part of the project named "Sustainable switch - The interaction between macroscopic loading modes and micro-scale mechanisms in railway switches" which was carried out under project number T91.1.12475a in the framework of the research program of the Materials innovation institute M2i (www.m2i.nl). The funding was received from Dutch railway infrastructure manager ProRail and Delft University of Technology.

Keywords: Bainitic steel, Pearlitic steel, Isothermal heat treatment, Microstructure, Mechanical properties, Carbide free bainitic steel, Damage initiation, Microstructural modelling, Crystal plasticity finite element method (CPFEM), Crystal plasticity fast Fourier transform (CPFFT)

ISBN xxxxxxxxxxxxxx
An electronic version of this dissertation is available at
http://repository.tudelft.nl/

Dedicated to

My parents and my sister

for their endless love, support and encouragement

Acknowledgement

These past years were a memorable chapter in my life and I will remember all the sweet memories, challenges and valuable lessons. It was a privilege for me to be a part of a leading research group and meet and collaborate with notable scholars. For this I am thankful to the Railway Engineering group and my promoters Prof. Zili Li and Prof. Rolf Dollevoet for their trust in me. Prof. Zili Li as my daily supervisor has patiently guided me during my research. He was very respectful, supportive and always capable of formulate a clear path towards solving any research question. Prof. Rolf Dollevoet is an experienced expert and proficient leader in railway infrastructure research with a very supportive attitude towards his team.

I would like to thank Prof. Jilt Sietsma, Prof. Roumen Petrov and Dr. Ankit Kumar from Material Science and Engineering group of TU Delft for their cooperation and detailed feedbacks for my research and publications. I definitely learned a lot about the material aspects of railway steels from all of them. It was a great experience to be a part of this cooperative research involving railways, computational mechanics and material science which would have not been possible without their consultations.

The sustainable switch project was carried out in the framework of a research program from the Materials innovation institute (M2i). This project also involved the Dutch railway infrastructure manager (ProRail) as the industry partner. Their supports for my research are greatly acknowledged. I would like to thank Dr. Viktoria Savran (from M2i) as the project manager and Dr. Ivan Shevtsov (ProRail) for their supports and valuable feedbacks. Extra thanks to Dr. Ivan Shevtsov for organizing various meetings at ProRail for the PhD researchers involved in this project, including me, Ankit Kumar and Martin Hiensch from TU Delft and Matthijs Oomen from University of Twente. Many thanks to Ruud van Bezooijen (from Id2 B.V.) for being very supportive and for sharing his experience of the Dutch railway industry during those meetings.

Yearly M2i conferences were great place to meet a lot of prominent researchers from all over Europe which were working on research fields involving various materials types. I would like to thank all the organizers from M2i. I met Kok Piet from Tata Steel in one of these conferences and I appreciate his help for providing me a software which was used to build the Voronoi diagrams for steel microstructure geometry definition.

I would like to express my gratitude to my colleagues and friends in the Railway Engineering group as well, Meysam Naeimi and Ali Jamshidi which were always up for a coffee break and helped me to feel like welcomed from the first day, Dr. Michael Steenbergen, Dr. Valerie Markine, Dr. Alfredo Nunez, Jacqueline Baarnhoorn, Ellard Groenewegen, Siamak Hajizadeh, Siamand Rahimi, Shaoguang Li, Hongrui Wang, Pan Zhang, Evert van Veldhuizen, Jurjen Hendriks, Xiangming Liu, Haoyo Wang, Zilong Wei, Zhen Yang, Xiangyun Deng, Chen Shen, Joris van Dijk, Chang Wan, Yuwei Ma, Harm Visser and many others which I may have forgotten. We spent thousands of hours together as colleagues and friends and I am grateful to each of you for all the unforgettable memories.

Most importantly, I would like to thank my family, my loving mother Vajiheh, my supportive father Hossein and my lovely sister Bahar in Iran which during all these years have given me unconditional counsel, love and support and therefore deserve my highest gratitude.

Omid Hajizad

May, 2021

The Hague, Netherlands

Table of Contents

Acknowledgement v
Summary xi
Samenvatting xiii
1 Introduction 1
1.1 Industrial aim and application of the project 1
1.2 Research objective 2
1.3 Outline 3
2 Damage in railway steels 5
2.1 Rolling Contact Fatigue 5
2.2 Switches and crossings 6
2.3 Steel grades used in railway crossings 7
2.3.1 Cast Hadfield austenitic Mn-steel 7
2.4 Material selection for crossings 9
2.5 References 10
3 Influence of Microstructure on Mechanical Properties of Bainitic Steels in Railway Applications 13
3.1 Introduction 14
3.2 Material and Experimental Methods 16
3.2.1 Chemical Composition, Sampling and Material Processing 16
3.2.2 Uniaxial Tensile Testing 19
3.2.3 Hardness Measurement 19
3.2.4 Microstructural Characterization 19
3.3 Results and Discussion 20
3.3.1 Tensile Tests 20

3.3.2 Strain Hardening Exponent 21
3.3.3 Fracture Surface Analysis 23
3.3.4 Hardness 26
3.3.5 Influence of Microstructure on Mechanical Properties 26
3.4 Conclusions 36
3.5 References 37
3.A. Supplementary information for chapter 3 42
3.A.1 Effect of Non-Metallic Inclusions on the Mechanical Performance 42
3.A.2 Measurement of Prior Austenite Grain Size (PAGS) 42
4 Strain partitioning and damage initiation in a continuously cooled carbide free bainitic steel 45
4.1 Introduction 46
4.2 Methodology 48
4.2.1 Material 48
4.2.2 Numerical models 49
4.2.3 In-situ tensile experiment 58
4.3 Numerical simulation results 59
4.3.1 von Mises J2 plasticity finite element model (VPFEM) 59
4.3.2 Phenomenological crystal plasticity fast fourier transform model (CPFFT) 61
4.4 The *in-situ* tensile test results 63
4.5 Discussion 67
4.6 Conclusion and future work 70
4.7 References 71
5 Crystal plasticity modelling of strain partitioning in high strength carbide free bainitic steel and validation using *in-situ* tensile experiment 81
5.1 Introduction 82
5.2 Methodology 83
5.2.1 Material and heat treatment 83
5.2.2 Numerical modelling 85
5.2.3 In-situ tensile experiments 89
5.3 Results 90

5.3.1 Crystal plasticity (CP) simulation 90
5.3.2 Validation using in-situ μ-DIC tests 91
5.4 Discussion 93
5.5 Summary and conclusions 95
5.6 References 95
6 Conclusion and recommendation for future work 103
7 Curriculum Vitæ 107
8 Scientific Publications 109

Summary

In this PhD thesis, we investigated possible steel candidates for use in railway crossings in order to reduce the damage in them.

Pearlitic R350HT together with Bainitic grades including CrB, B1400 and carbide free B360 were investigated for their mechanical properties such as ultimate strength, yield strength, ductility and hardness. The influence of their microstructure on these mechanical properties was studied using microscopy techniques such as light optical microscopy (LOM), scanning electron microscopy (SEM) and electron backscatter diffraction (EBSD). The effect of an isothermal heat treatment was also investigated on the bainitic steels which were mostly manufactured using continuous cooling.

Carbide free bainitic steel B360 was found to have the highest strength, ductility and toughness among all the steels. These properties became even better after the isothermal heat treatment.

It was decided to investigate this grade further in detail regarding its damage initiation properties. Micromechanical modelling and *in-situ* experiment with micro Digital Image Correlation (μDIC) was used to measure local strain maps during tensile loading. Microscopic strain partitioning was used to investigate the damage initiation behavior of this steel before and after the isothermal heat treatment.

The deformation localization in the Continuously Cooled Carbide Free Bainitic Steels (CC-CFBS) (B360) was modelled using elastic plastic and crystal plasticity material models. Both models were validated using the *in-situ* tensile experiment.

A 2D real geometry was used as the micromechanical Representative Volume Element. The blocky retained austenite (BRA) was considered as martensite from the beginning of the loading since during the experiments, it was confirmed that large portion of the BRA transform into martensite in a strain-induced transformation mechanism.

The main damage mechanism in this steel was observed to be the strain localization in narrow bainitic channels between martensitic islands and the large BRA (which turn into martensite) and in the interfaces of bainite with martensite. The initiated micro cracks can later fracture the martensitic islands.

Other factors such as the interface of martensite/bainitic ferrite, the orientation of this interface and the phase morphology also influence the damage initiation in the continuously cooled B360 steel.

An isothermal heat treatment was performed on this steel in order to remove/reduce the main damage initiating factors such as martensitic islands and the large BRA which was proved to improve the mechanical properties and damage characteristics .

The deformation localization in isothermally heat treated CFBS (B360-HT) was modelled and the modelling results were validated using the *in-situ* experimental tensile tests.

The effect of the isothermal heat treatment on B360 was to remove martensite, form finer bainitic microstructure and remove the unstable large BRA. As a result, small and homogeneously distributed BRA was observed in the B360-HT. The combination of numerical simulation and *in-situ* test revealed that the new proposed microstructure of carbide free bainitic steel has less strain localization compared to the continuously cooled B360 steel. The maximum local strain was reduced from 35% to 25% using the isothermal heat treatment. In the B360-HT, the strain bands usually form in 45° to the tensile axis.

This new proposed microstructure of carbide free bainitic steel could be a good candidate to be used in the crossing nose.

Samenvatting

In dit PhD onderzoek, hebben we mogelijke staalkandidaten onderzocht voor gebruik in spoorwegovergangen om de schade daarin te verminderen.

Pearlitic R350HT samen met bainitische staalsoorten zoals CrB, B1400 en carbide-vrij B360 werden onderzocht op hun mechanische eigenschappen zoals ultieme sterkte, vloei sterkte, ductiliteit en hardheid. De invloed van hun microstructuur op deze mechanische eigenschappen werd bestudeerd met behulp van microscopietechnieken zoals licht-optische microscopie (LOM), scanning-elektronenmicroscopie (SEM) en elektronen-terugverstrooiingsdiffractie (EBSD). Het effect van een isotherme warmtebehandeling werd ook onderzocht op de bainitische staalsoorten die veelal met continue koeling werden vervaardigd.

Carbide-vrij bainitisch staal B360 bleek de hoogste sterkte, ductiliteit en taaiheid te hebben van alle staalsoorten. Deze eigenschappen werden nog beter na de isotherme warmtebehandeling.

Besloten werd om deze kwaliteit nader te onderzoeken op zijn schade-initiërende eigenschappen. Micromechanische modellering en in-situ experiment met micro Digital Image Correlation (μDIC) werden gebruikt om lokale rekkaarten tijdens trekbelasting te meten. Microscopische spanningsverdeling werd gebruikt om het beschadigingsgedrag van dit staal voor en na de isothermische warmtebehandeling te onderzoeken.

De vervormingslokalisatie in de continu gekoelde carbide-vrij B360 staal (Continuously Cooled Carbide Free Bainitic Steels (CC-CFBS)) werd gemodelleerd met behulp van modellen van elastisch plastic en kristal plasticiteit materiaal modellen. Beide modellen werden gevalideerd met behulp van het in-situ trekexperiment.

Een 2D echte geometrie werd gebruikt als het micromechanische representatieve volume-element. Het blocky retained austeniet (BRA) werd vanaf het begin van de belasting als martensiet beschouwd, aangezien tijdens de experimenten werd bevestigd dat een groot deel van de BRA in martensiet transformeert in een door spanning geïnduceerd transformatie mechanisme.

Het belangrijkste beschadigingsmechanisme in dit staal was de rek lokalisatie in smalle bainitische kanalen tussen martensitische eilanden en de grote BRA (die in martensiet veranderen) en in de grensvlakken van bainiet met martensiet. De geïnitieerde microscheuren kunnen later de martensitische eilanden breken.

Andere factoren zoals het grensvlak van martensiet / bainitisch ferriet, de oriëntatie van dit grensvlak en de fasemorfologie ook beïnvloedt schade in het continu gekoelde B360-staal.

Op dit staal is een isothermische warmtebehandeling uitgevoerd om de belangrijkste factoren die de schade veroorzaken, zoals martensitische eilanden en de grote BRA, te verwijderen / verminderen waarvan is bewezen dat deze de mechanische eigenschappen en schade eigenschappen verbetert.

De vervormings lokalisatie in isotherme warmtebehandelde CFBS (B360-HT) werd gemodelleerd en de modelresultaten werden gevalideerd met behulp van de in-situ experimentele trek tests.

Het effect van de isotherme warmtebehandeling op B360 was om martensiet te verwijderen, een fijnere bainitische microstructuur te vormen en de onstabiele grote BRA te verwijderen. Als resultaat werd een kleine en homogeen verdeelde BRA waargenomen in de B360-HT.

De combinatie van numerieke simulatie en in-situ test onthulde dat de nieuwe voorgestelde microstructuur van carbide-vrij bainitisch staal minder rek lokalisatie heeft in vergelijking met het continu gekoelde B360-staal. De maximale lokale rek werd verminderd van 35% naar 25% met behulp van de isotherme warmtebehandeling. In de B360-HT vormen de spanningsbanden zich meestal in 45 ° ten opzichte van de trekbelasting as.

Deze nieuwe voorgestelde microstructuur van carbide-vrij bainitisch staal zou een goede kandidaat kunnen zijn voor gebruik in de kruising neus.

1 Introduction

1.1 Industrial aim and application of the project

The Dutch rail infrastructure manager, ProRail is responsible for the operation, maintenance and safety of the Dutch railway network, which daily transports of 1,200,000 passengers and 100,000 tonnes of products with 6550 trains on 7000 km of tracks. 6500 witches and crossings (S&Cs) help guide the trains from one track to another in the network.

Rails and especially S&Cs are constantly subjected to complex loading conditions. Typically, crossing noses are subjected to severe impact by passing wheels. These lead to various defects like irregular wear, plastic deformation, squats, head checks and etc. Examples of head checks and squat are shown in Figure 1.1(a) and Figure 1.1(b) respectively.

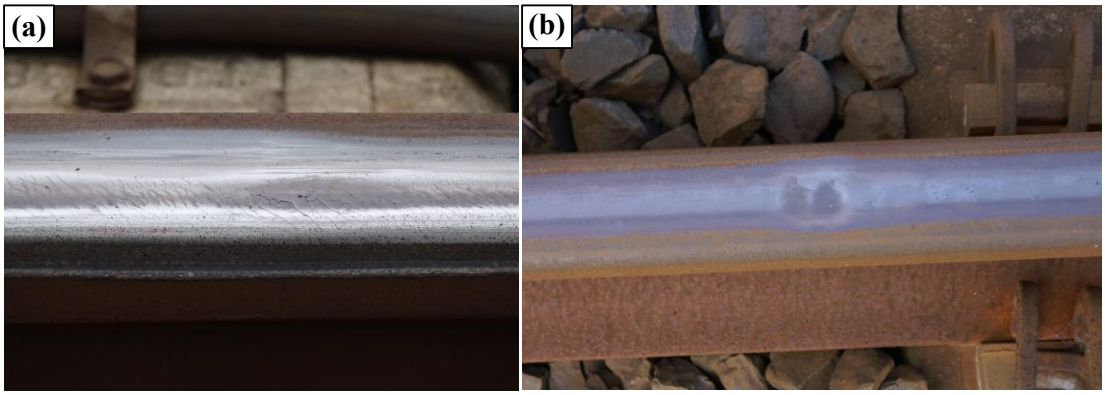

Figure 1.1. RCF in rails such as (a) Head checks, (b) Squat

Finally the defects may lead to failure of the rails and crossings which causes safety concerns and financial issues. Currently, an average of 100 crossings are urgently replaced and 300 crossings are planned for regular replacement yearly.

Hence, ProRail is seeking new materials which are more resistant to damage under such working condition. Most rails are made of steels with pearlitic microstructure, a lamellar structure of ferrite and cementite. Due to increase in vehicle speed and axle load, new steel grades are required. Bainitic steels are a good candidate because of their excellent mechanical properties, such as high strength and toughness. Different microstructural features could influence the damage mechanism in an specific steel. In order to investigate this influence, there is a need for research on these different steel types on microstructural level.

The steels which are candidates to be studied in this research include R350HT pearlitic grade and bainitic grades such as B360, B1400 and Cr-Bainite (CrB).

1.2 Research objective

This research was carried out under project number T91.1.12475a in the framework of the research program of the Materials Innovation Institute (M2i). The results of this research could open the ways for selection of the best steel grades and further improvement of them before implementation in the Dutch rail network.

The severe loading condition causes microstructural alterations, plastic deformation, micro-crack initiation and propagation in the rail steel microstructures. The mechanical behaviour and damage of these steels are directly dependent on their microstructure and the key to design steels with better mechanical properties lies in optimization of the microstructures. The main scientific aim of this project is to investigate the interaction between material microstructure and damage initiation mechanisms in the mentioned railway steels, especially those for S&Cs.

To this end, a detailed comparison of the mechanical properties, in terms of yield and ultimate strength, uniform strain, true and engineering fracture strain, toughness, strain hardening exponent and hardness of these steels in as-received form and after a proposed heat treatment, is performed, their microstructures are analysed using different microscopy techniques and the relation between these mechanical properties and the microstructural features are further investigated. Then the suitable type of steel which is a carbide free bainitic steel is chosen for further detailed microstructural investigation. The damage initiation in this bainitic steel is studied using micromechanical modelling and *in-situ* tensile experiment. Based on this analysis, a heat treatment is proposed in order to remove/reduce the damage initiating factors in this bainitic steel and a modified microstructure of the carbide free bainitic steel is proposed which shows better damage initiation resistance. To confirm this enhanced damage resistance, damage initiation in this steel is also investigated using micromechanical modelling and *in-situ* experiment.

The results of *in-situ* experiments have been used to validate the numerical strain partitioning analysis. These *in-situ* tensile experiments have been performed by A. Kumar et al. which was another researcher in the same project. His doctoral dissertation is referenced below:

Kumar, A. (2019). Multiscale study of microstructural evolution and damage in rail steels. https://doi.org/10.4233/uuid:00f46cda-0b41-48a1-a7c4-f050c13d90fb.

1.3 Outline

The structure of this dissertation is organized as following:

In chapter 2, damage in railway steels will be discussed and our approach towards investigating the damage in crossing nose will be explained.

In chapter 3, the mechanical behavior of three bainitic grades B360, B1400 and CrB (in as-received and heat treated forms) together with already-in-use pearlitic R350HT steel were compared using uniaxial tensile experiments and hardness measurements. The impact of a proposed heat treatment on the mechanical properties of the bainitic grades was studied. The microstructure of the bainitic steels were further analysed using Light Optical Microscopy (LOM), Scanning Electron Microscopy (SEM) and Electron Backscatter Diffraction (EBSD). Finally the influence of the microstructure on the properties such as yield/tensile strength, ductility and hardness were studied. The best steel type, the carbide free bainitic B360 steel, was chosen based on the mechanical properties for further damage initiation studies.

In chapter 4, to investigate the damage initiation in the carbide free bainitic B360 steel, *in-situ* tensile test and numerical modelling using both elastic-plastic and crystal plasticity material models were performed. Strain partitioning in the experiment and the numerical simulations were used to investigate the damage initiating factors in this steel. Results showed the influence of microstructural features on the damage initiation which could be removed or reduced in order to obtain a more damage resistant microstructure.

In chapter 5, using the information gained from the previous study, we designed a new microstructure for carbide free bainitic steel and studied its damage behavior under the *in-situ* tensile tests and micromechanical simulations. The positive effects of removing/reducing the damage initiating factors (that were present in the previous as-received steel) were also discussed. Results confirmed that the new design performs better than the as-received carbide free bainitic steel with regard to strain partitioning and damage initiation.

In chapter 6, the main conclusions and recommendations for future work are presented.

At the last chapter a summary of the dissertation is presented.

2 Damage in railway steels

2.1 Rolling Contact Fatigue

The contact pressure at the wheel-rail interface is high due to high loads and small contact patch size. Steels used in the railway are subjected to Rolling Contact Fatigue (RCF) damage and wear due to wheel rail contact.

The RCF damage could start at the surface or sub-surface of the rails.

The sub-surface damage mainly occurs due to non-metallic inclusions in rail steels. These inclusions could create areas of stress localization around them, which would initiate cracks. Improvement of the steelmaking processes would help reducing such damage.

Modern steelmaking have indeed greatly reduced inclusions that can lead to RCF. RCF is now generally known as the failure of a surface subjected to cyclic contact stress produced under rolling and sliding loading conditions. A fatigue mechanism of crack initiation and propagation caused by near surface alternating stress field involves plastic deformation which is non-uniformly distributed in complicated polycrystalline materials. The fatigue process includes reversible/irreversible dislocation movements, vacancy generation, crystallographic texture development and break down of the hardened microstructure which makes the material brittle. As a result, matrix can no longer bear applied stresses and crack initiates, propagates and eventually leads to failure.

Low coefficient of friction would result in wheel slip on the rail when acceleration or braking while high coefficient of friction, would produce high stresses that could plastically deform the rail steel. Other causes such as dynamic loads would also cause such high stresses. Repetitive high stresses on the rail would result in accumulation of plastic deformation which would initiate fatigue cracks on the surface of the rails.

There are mainly two types of such surface initiated RCF damage, head checks and squats.

Head checks are regularly spaced cracks appearing at the gauge corner of the rail because of the large tangential contact stress due to spin creepage, most often in the outer rails of curves and sometimes in tangent rails. This stress exhausts the ductility of the material at the surface of the rail and initiate cracks [1–4]. At the initiation of these cracks, they grow at a shallow angle with respect to the rail surface. These cracks often grow and form spalling of rail surface material. Later head check cracks could grow with a more steep angle into the rail head [5] which could finally lead to rail break. At initial stages, crack propagation is driven by ratchetting in the plastically deformed layer. These cracks then grow by repeated contact loading and at the final stages they propagate downwards, driven by the bending stresses.

Squats are shallow depression with a dark patch appearance more or less in the centre of the rail head. Squats generally are seen on tangent or slightly curved tracks. Whereas head check cracks initiate at quasi-static wheel-rail contact, squats initiate and grow due to dynamic wheel-rail contact at rail surface irregularities such as indentations [6,7], short pitch corrugations [8], poor welds [9], differential wear and plastic deformation [10], running surface discontinuity at insulation joints [11] and frogs of S&C [12–14]. Cracks initiate in the surface and then propagate to the sub-surface of the rail.

The most successful method so far for preventing these surface initiated cracks is to grind the rail surface and remove the damaged layer [15].

2.2 Switches and crossings

Switches and crossings (S&Cs) are used to guide trains from one track to another. When train passes the crossing, high impact load is created [4,14,16,17]. The impact loading can be the result of developing RCF damage, but first of all the result of the unfavorable geometry discontinuity due to the gap between the crossing nose from the wing rail. This impact loading depends on the vehicle velocity, unsprung mass, track stiffness and the wheel travelling trajectory. In this research we focus mainly on the material damage mechanism and optimization so that the material could resist such loading condition. This severe loading condition increases the chance of damage such as plastic deformation, wear, head checking, squats, spalling, shelling and etc. Figure 2.1 shows an example of squat at crossing nose.

Figure 2.1. RCF damage at railway crossing

The damage has high economic and safety consequences due to the repair and replacement of the damaged rails, as well as the risk of fracture.

2.3 Steel grades used in railway crossings

Crossings are usually made from conventional pearlitic steels or casted Hadfield austenitic Mn-steel. Both grades have their advantages and disadvantages regarding their service life, weldability and maintenance. They become less suitable to meet the demands of high speed and increasing traffic on the Dutch rail network. Bainitic steels have an intermediate microstructure between pearlite and martensite. They can achieve very good mechanical properties and more resistance to damage under wheel-rail contact working conditions. Bainitic microstructures with a proper composition could be a possible candidate for usage in crossings in the Dutch railway network.

2.3.1 Cast Hadfield austenitic Mn-steel

Hadfield high manganese steel (with 13% Mn) has single phase full austenite microstructure at room temperature. High amount of Mn helps to have a stabilized austenite at this temperature. This steel shows excellent work-hardening rate, high toughness and high wear resistance [18,19].

There are many phenomena responsible for the work hardening in the Hadfield steel under impact loads in railway switches such as twin hardening, dislocation hardening, dynamic strain aging hardening [20].

Repeated contact stresses introduce microstructural evolution and internal compressive strain in the surface layer of Hadfield steels [21]. Residual strain can also be created by welding and plastic deformation under the working condition of these

steels. Feng et al. [22] studied the residual strain distribution and its effect on cracks. They confirmed that Hadfield steel used in switches fail mainly due to the formation and propagation of cracks in the subsurface layer where a high strain concentration is produced by the repeatedly transient impact load. Based on the same study, it is shown that the formation and propagation of fatigue cracks in Hadfield railway steels resulting from the growth and coalescence of voids, is not related to the texture of the austenite grains. The deformation twinning and dislocation slipping are the main reasons for work hardening of Hadfield steels and initiation of damage and cracking are mainly because of locally concentrated strain associated with non-uniform work hardening [22].

Casting is used to manufacture the manganese crossings and the cooling process can lead to formation of brittle carbides in this steel microstructure [23]. This would affect the high toughness and could initiate cracks during impact fatigue loading. Welding and the cooling which comes after welding could also form carbides.

After the casting solution-annealing is performed at 1050 °C for few hours with water quenching which comes after that [23]. This leads to surface decarburization and loss of Mn, and hence formation of α-martensite on the surface layer upon quenching [23]. This brittle layer on the surface, could help initiate microcracks during loading. At the beginning of installation of the crossing with the first loading cycles on it, this could initiate damage in the steel. However, performing grinding on the crossing and removing the brittle martensite layer can help solve this issue.

There are several reported damage mechanisms in Hadfield crossings. One study suggests that in the Hadfield steel crossing the RCF cracks initiate in the subsurface parallel to the surface and they propagate to surface to form spalling [18]. The initiation mechanism was explained to be due to formation of high concentration layers of the vacancy clusters parallel to the crossing surface [18]. Another damage mechanism in Hadfield steels could be the strain-induced transformation of austenite to ε or α-martensite [24].

In a recent study which was carried out in collaboration with this PhD research in the framework of project number T91.1.12475a of the research program of the Materials innovation institute M2i, the damage mechanism of a Hadfield steel crossing was investigated [25]. Main deformation mechanism was reported to be deformation twinning which happened mainly near the surface of the crossing. The main damage initiation mechanism was reported to be casting defects such as gas porosities/solidification shrinkages and non-metallic inclusion and other damage mechanism such as strain-induced austenite to martensite transformation was not observed [25]. Regarding crack growth, the influence of grain boundaries and twin boundaries for the deflection of initiated cracks was emphasized [25].

Therefore this steel was not further investigated in this PhD work and the main emphasis was on the pearlitic and specially bainitic grades such as B360, B1400 and CrB.

2.4 Material selection for crossings

Currently, preventing the RCF damage is of crucial importance as the axle load and the speed of both passenger and freight trains are increasing. Higher traction and pressure acting on the rails cause them to damage more frequently. The crossing nose in Dutch S&Cs tend to suffer from high impact loading and RCF damage which cause fracture eventually.

Crossing nose geometry in relation to wheel travelling trajectory together with track stiffness are very important factors which influence the damage process in the crossings.

However from material point of view, there is a need to design materials of higher fatigue strength [26]. The damage development in different types of steels depends on their mechanical properties such as yield strength, hardness and toughness. The mechanical properties and damage characteristics of the steels are mainly influenced by their microstructure. Mechanical properties, damage characteristics and microstructural features of pearlitic and bainitic steels are investigated in this dissertation. Regarding material parameters, RCF development characteristics and plastic deformation are crucial. Material resistance to RCF can improve with increasing the yield limit in pure shear.

Crossings face a complex loading due to mentioned impact fatigue, RCF and wear. In order to avoid plastic deformation, steels with higher yield strength could be designed. Using the von Mises stress theory, the complex loading can be simplified for material design purpose. Based on this theory, a ductile material will yield when the elastic energy of distortion per volume u_d reaches a critical value. This critical value is the distortion energy per unit volume $(u_d)_Y$ of the same material at the yield point in a simple tension test.

$$u_d = \frac{1+\vartheta}{3E}\left[\frac{(\sigma_1-\sigma_2)^2 + (\sigma_2-\sigma_3)^2 + (\sigma_3-\sigma_1)^2}{2}\right] \tag{2.1}$$

where σ_1, σ_2 and σ_3 are the principal stresses, ϑ is the Poisson's ratio and E is the elastic modulus.

$$(u_d)_Y = \frac{1+\vartheta}{3E}(\sigma_y)^2 \tag{2.2}$$

where σ_y is the yield strength of the material.

In order for material not to reach the yielding limit $u_d < (u_d)_Y$. Inputting equations (2.1) and (2.2)(2.2) into this equation would result in:

$$\left[\frac{(\sigma_1 - \sigma_2)^2 + (\sigma_2 - \sigma_3)^2 + (\sigma_3 - \sigma_1)^2}{2}\right]^{1/2} < \sigma_y \quad (2.3)$$

This equation means that if the von Mises stress in the railway steels is less than the yield strength, the steel would not face plastic deformation and hence the type of damage associated with the localized plastic deformation. The von Mises stress in the crossing nose could be from 700 to 1100 MPa [27–30]. Designing a steel with a high yield strength (than the von Mises stress produced in the crossing nose under impact load) could be a possible solution for higher fatigue life of railway crossings.

2.5 References

[1] R. Dollevoet, Z. Li, O. Arias-Cuevas, A Method for the Prediction of Head Checking Initiation Location and Orientation under Operational Loading Conditions, Proc. Inst. Mech. Eng. Part F J. Rail Rapid Transit. 224 (2010) 369–374. doi:10.1243/09544097JRRT368.

[2] A. Zoeteman, R. Dollevoet, Z. Li, Dutch research results on wheel/rail interface management: 2001-2013 and beyond, Proc. Inst. Mech. Eng. Part F J. Rail Rapid Transit. 228 (2014) 642–651. doi:10.1177/0954409714524379.

[3] Y. Zhou, S. Wang, T. Wang, Y. Xu, Z. Li, Field and laboratory investigation of the relationship between rail head check and wear in a heavy-haul railway, Wear. 315 (2014) 68–77. doi:10.1016/j.wear.2014.04.004.

[4] N. Burgelman, Z. Li, R. Dollevoet, A new rolling contact method applied to conformal contact and the train-turnout interaction, Wear. 321 (2014) 94–105. doi:10.1016/j.wear.2014.10.008.

[5] R.P.B.J. Dollevoet, Design of an anti head check profile based on stress relief, University of Twente, 2010. doi:10.3990/1.9789036530736.

[6] Z. Li, X. Zhao, C. Esveld, R. Dollevoet, M. Molodova, An investigation into the causes of squats-Correlation analysis and numerical modeling, Wear. 265 (2008) 1349–1355. doi:10.1016/j.wear.2008.02.037.

[7] Z. Li, R. Dollevoet, M. Molodova, X. Zhao, Squat growth-Some observations and the validation of numerical predictions, Wear. 271 (2011) 148–157. doi:10.1016/j.wear.2010.10.051.

[8] X. Deng, Z. Qian, Z. Li, R. Dollevoet, Investigation of the formation of corrugation-induced rail squats based on extensive field monitoring, Int. J. Fatigue. 112 (2018) 94–105. doi:10.1016/j.ijfatigue.2018.03.002.

[9] X. Deng, Z. Li, Z. Qian, W. Zhai, Q. Xiao, R. Dollevoet, Pre-cracking development of weld-induced squats due to plastic deformation: Five-year field monitoring and numerical analysis, Int. J. Fatigue. 127 (2019) 431–444. doi:10.1016/j.ijfatigue.2019.06.013.

[10] Z. Li, X. Zhao, R. Dollevoet, M. Molodova, Differential wear and plastic deformation as causes of squat at track local stiffness change combined with other track short defects, Veh. Syst. Dyn. 46 (2008) 237–246. doi:10.1080/00423110801935855.

[11] Z. Yang, A. Boogaard, Z. Wei, J. Liu, R. Dollevoet, Z. Li, Numerical study of wheel-rail impact contact solutions at an insulated rail joint, Int. J. Mech. Sci. 138–139 (2018) 310–322. doi:10.1016/j.ijmecsci.2018.02.025.

[12] Z. Wei, A. Núñez, A. Boogaard, R. Dollevoet, Z. Li, Method for evaluating the performance of railway crossing rails after long-term service, Tribol. Int. 123 (2018) 337–348. doi:10.1016/j.triboint.2018.03.016.

[13] Z. Wei, A. Núñez, Z. Li, R. Dollevoet, Evaluating degradation at railway crossings using axle box acceleration measurements, Sensors (Switzerland). 17 (2017). doi:10.3390/s17102236.

[14] Z. Wei, C. Shen, Z. Li, R. Dollevoet, Wheel–Rail Impact at Crossings: Relating Dynamic Frictional Contact to Degradation, J. Comput. Nonlinear Dyn. 12 (2017) 041016. doi:10.1115/1.4035823.

[15] E. Magel, P. Sroba, K. Sawley, J. Kalousek, Control of Rolling Contact Fatigue of Rails, in: AREMA 2004 Annu. Conf., Nashville, Tennessee, USA, 2004.

[16] M.A. Boogaard, Z. Li, R.P.B.J. Dollevoet, In situ measurements of the crossing vibrations of a railway turnout, Meas. J. Int. Meas. Confed. 125 (2018) 313–324. doi:10.1016/j.measurement.2018.04.094.

[17] Z. Wei, A. Boogaard, A. Nunez, Z. Li, R. Dollevoet, An integrated approach for characterizing the dynamic behavior of the wheel-rail interaction at crossings, IEEE Trans. Instrum. Meas. 67 (2018) 2332–2344. doi:10.1109/TIM.2018.2816800.

[18] B. Lv, M. Zhang, F.C. Zhang, C.L. Zheng, X.Y. Feng, L.H. Qian, X.B. Qin, Micro-mechanism of rolling contact fatigue in Hadfield steel crossing, Int. J. Fatigue. 44 (2012) 273–278. doi:10.1016/j.ijfatigue.2012.04.010.

[19] P.H. Adler, G.B. Olson, W.S. Owen, Strain Hardening of Hadfield Manganese Steel, Metall. Trans. A. 17A (1986) 1725–1737.

[20] Y.N. DASTUR, W. C. LESLIE, Mechanism of Work Hardening in Hadfield Manganese Steel, Metall. Trans. A. 12A (1981) 749–759.

[21] W. Jing, Focuses of material science development in recent years, Sci China Tech Sci. 54 (2011) 1645–1648. doi:10.1007/s11431-011-4383-3.

[22] X.Y. FENG, F.C. ZHANG, C.L. ZHENG, B. LÜ, Micromechanics behavior of fatigue cracks in Hadfield steel railway crossing, Sci China Tech Sci. 56 (2013) 1151–1154. doi:10.1007/s11431-013-5181-x.

[23] A.K. Srivastava, D. Karabi, Microstructural characterization of Hadfield austenitic manganese steel, J Mater Sci. 43 (2008) 5654–5658. doi:10.1007/s10853-008-2759-y.

[24] T.S. Wang, B. Lu, M. Zhang, R.J. Hou, F.C. Zhang, Damage and microstructure evolution in cast Hadfield steels used in railway crossings, Mater. Sci. Eng. A 458. 458 (2007) 249–252. doi:10.1016/j.msea.2006.12.066.

[25] A. Kumar, R. Petrov, J. Sietsma, Damage and microstructure evolution in cast Hadfield steels used in railway crossings, 2019.

[26] Z. Wei, A. Núñez, X. Liu, R. Dollevoet, Z. Li, Multi-criteria evaluation of wheel/rail degradation at railway crossings, Tribol. Int. 144 (2020). doi:10.1016/j.triboint.2019.106107.

[27] L. Xin, V.L. Markine, I.Y. Shevtsov, Numerical analysis of the dynamic interaction between wheel set and turnout crossing using the explicit finite element method, 3114 (2016). doi:10.1080/00423114.2015.1136424.

[28] L. Xin, V.L. Markine, I.Y. Shevtsov, Numerical procedure for fatigue life prediction for railway turnout crossings using explicit fi nite element approach, Wear. 366–367 (2016) 167–179. doi:10.1016/j.wear.2016.04.016.

[29] J.H. Xiao, F.C. Zhang, L.H. Qian, Contact stress and residual stress in the nose rail of a high manganese steel crossing due to wheel contact loading, (2014) 219–226. doi:10.1111/ffe.12108.

[30] J. Xiao, F. Zhang, L. Qian, Numerical simulation of stress and deformation in a railway crossing, Eng. Fail. Anal. 18 (2011) 2296–2304. doi:10.1016/j.engfailanal.2011.08.006.

3 Influence of Microstructure on Mechanical Properties of Bainitic Steels in Railway Applications*

Wheel–rail contact creates high stresses in both rails and wheels, which can lead to different damage, such as plastic deformation, wear and rolling contact fatigue (RCF). It is important to use high-quality steels that are resistant to these damages. Mechanical properties and failure of steels are determined by various microstructural features, such as grain size, phase fraction, as well as spatial distribution and morphology of these phases in the microstructure. To quantify the mechanical behavior of bainitic rail steels, uniaxial tensile experiments and hardness measurements were performed. In order to characterize the influence of microstructure on the mechanical behavior, various microscopy techniques, such as light optical microscopy (LOM), scanning electron microscopy (SEM) and electron backscatter diffraction (EBSD), were used. Three bainitic grades industrially known as B360, B1400 plus and Cr-Bainitic together with commonly used R350HT pearlitic grade were studied. Influence of isothermal bainitic heat treatment on the microstructure and mechanical properties of the bainitic grades was investigated and compared with B360, B1400 plus, Cr-Bainitic and R350HT in as-received (AR) condition from the industry. The results show that the carbide-free bainitic steel (B360) after an isothermal heat treatment offers the best mechanical performance among these steels due to a very fine, carbide-free bainitic microstructure consisting of bainitic ferrite and retained austenite laths.

* This chapter is based on a published article:

Hajizad, O.; Kumar, A.; Li, Z.; Petrov, R.H.; Sietsma, J.; Dollevoet, R. Influence of Microstructure on Mechanical Properties of Bainitic Steels in Railway Applications. *Metals* **2019**, *9*, 778.

3.1 Introduction

Energy and material conservation have stimulated research to produce high performance steels for structural applications. These steels should combine high strength with good ductility and toughness. Steels are widely used in railway infrastructure, and their good performance is crucial to enhance the safety of the system and to reduce the cost of repairs or replacements. There are multiple track components, such as straight tracks, curved tracks, switches and crossings (S&Cs), that are manufactured from different steels and are subjected to various loading conditions. For example, rails suffer from high contact loads of frictional rolling, which create a complex multiaxial shear and compressive stress state. These high contact stresses eventually lead to rolling contact fatigue (RCF). The two major types of RCF defects are head checks (HC) and squats [1–6]. On the other hand, S&Cs that help guide the trains from one track to another are subjected to rather complex loading conditions in comparison with the rails. At crossing, the wheel rolls from the wing rail to the crossing nose or in the opposite direction, generating heavy impact loads in addition to RCF and wear. These loading conditions deteriorate the crossing nose over time by local plastic deformation, irregular wear and various RCF defects. These defects can finally lead to failure if they are not repaired in time and would cause safety issues and financial costs due to replacement. Therefore, the steel used to manufacture S&Cs must have good impact fracture toughness.

The response of the material to the forces acting in the contact zone between rail and wheel is of crucial importance. Due to these forces, rails (and wheels) will be deformed, and their properties will change over time. Mechanical properties such as yield and ultimate strength, uniform elongation, fracture toughness, hardness, impact strength and crack growth parameters provide valuable information about the way materials interact and fail under these external loadings. Some of these properties, such as yield and ultimate strength, uniform strain, true and engineering fracture strain, toughness, strain hardening exponent and hardness, are evaluated in this paper.

The mechanical behavior and damage in steels are directly dependent on their microstructure, and the key to producing steels with better mechanical properties lies in optimization of their microstructure. Most rails are made of steels with pearlitic microstructure, which is an alternating lamellar structure of ferrite and cementite. The mechanical behavior of different pearlitic rail steels in relation with their microstructure has been widely investigated in the literature [7–20]. The pearlitic rail steel grades offer appreciable wear resistance due to their hardness values ranging from 260 to 400 HB [21]. The hardness values can be further increased by increasing the carbon content in pearlitic grades, which results in higher wear resistance in the steel microstructure [7], but this comes with the cost of reducing fracture toughness

and producing poor weldability. The wear resistance of the pearlite steels can be further improved by refining the microstructure [13,14] using accelerated cooling or by using high concentrations of Mn, Cr, V, Si and Mo in the alloy composition [15–17,19]. Increased concentrations of these alloying elements shift the continuous cooling transformation curve towards longer times (decrease the critical quench rate), and fine pearlitic microstructure can be achieved with low cooling rates [20]. Some pearlitic steels, such as R350HT, which have good impact properties, are used to manufacture S&Cs.

Cast manganese austenitic Hadfield steels are also used for this purpose due to their good work-hardening rate, high toughness and excellent wear resistance properties under compressive loading [22,23]. These steels have low yield strength, which can cause excessive deformation and consequently work hardening, which leads to change in the geometry of the crossing. In this case, welding is used to restore the original dimensions of the crossing. However, Hadfield steels have poor weldability, which is usually due to high carbon content and formation of carbides during the cooling process after welding, which can decrease the material toughness [24]. Furthermore, higher thermal expansion coefficient of Hadfield steel compared to pearlitic grades can cause problems during welding [25,26].

Due to high speed and high axle load requirements of future railways, new steel grades are required. Bainitic steels are a good candidate because of their excellent mechanical properties, such as high strength and toughness. This microstructure was discovered by Bain and Davenport [27] and generally forms by phase transformation in the temperature range between pearlite finish and martensite start temperatures. Depending on the bainite transformation temperature, there exist two distinct forms of bainite, i.e., upper bainite and lower bainite. The upper bainite, which is obtained in the high temperature range (~400–500 °C for the rail steels), consists of coarser laths of bainitic ferrite and carbides than lower bainite formed in the lower temperature range (300–400 °C) [26–31]. This results in poorer mechanical properties in the upper bainite [32,33] than in the lower bainite, which offers better mechanical properties, namely strength, hardness and toughness [33–35]. The bainitic steels primarily contain lamellar structures of bainitic ferrite and cementite. The brittle cementite phase is considered to be detrimental for the fatigue properties of the bainitic steels [35]. The precipitation of cementite can be suppressed by using high concentration of Si and Al, which leads to the formation of carbide-free bainitic microstructures. This microstructure consists of bainitic ferrite and retained austenite lamellae, and due to high strength, ductility and toughness, it is being used extensively in industry [36–39]. Bainitic rails can be produced with conventional methods by natural air cooling after rolling. They have hardness above 400 HB and fracture toughness much better than the conventional head-hardened (HH) pearlitic rail steels. This results in much better RCF resistance together with a wear resistance at least as good as in HH pearlitic rail

steels [40]. It was also reported that for most laboratory rolling/sliding tests, with the same hardness, bainitic microstructures are more wear resistant than pearlitic ones [41].

The microstructure of the steels is dependent on their chemical composition and the heat treatment performed on them during production process. The variations in the bainitic-type microstructures can be very large and depend significantly on the chemical compositions and the thermal treatment parameters, such as austenitization temperature/time, bainitic isothermal temperature/time and cooling rates. These variations in microstructures during bainitic transformation are also sensitive and dependent on the dimensions of the rails. That is why the bainitic microstructures in rails can often contain lower, upper bainite, martensite and retained austenite. Having in mind the growing interest of the rail industry for the bainitic steels, this work aims to compare the influence of bainitic microstructures formed in different bainitic rail steels on their mechanical properties. The intention of the work is to focus on the mechanical properties in relation to the microstructure but not on the specific details of the formation of the microstructures. Including also these aspects would make the study too extensive. That is why the microstructures of the rail steels are described qualitatively and quantitatively, but the specific physical metallurgy aspects of bainite formation are not discussed.

These bainitic grades in as-received (AR) condition and after the heat treatment (HT) were compared using uniaxial tensile tests and hardness measurements. In this way, we can understand the influence of the specific microstructures on the mechanical performance of these bainitic steels. The performance of these bainitic steels is also compared with commonly used R350HT pearlitic grade. The mechanical properties, such as maximum tensile strength, yield strength, uniform elongation, engineering and true fracture strains, toughness and strain hardening exponent (SHE) were obtained from tensile testing. Hardness of the steels was also compared using micro-hardness measurements. In order to investigate the influence of microstructure on these properties, imaging techniques such as light optical microscopy (LOM), scanning electron microscopy (SEM) and electron backscatter diffraction (EBSD) were used. At the end, as conclusion, the most suitable combination of steel grade and heat treatment is proposed for a more sustainable railway network.

3.2 Material and Experimental Methods

3.2.1 Chemical Composition, Sampling and Material Processing

The chemical composition of the steels studied in this paper is shown in Table 3.1. The bainitic steels have less carbon compared to the pearlitic grade. B360 has the lowest carbon content (≈0.27 wt %) and a high concentration of Si. Both bainite 1400 (B1400)

and chrome bainitic (CrB) steels grades have equal carbon content (≈0.36 wt %) with different concentrations of other alloying elements.

Table 3.1. Chemical composition of steels in (wt %).

Steel Grade	C	Cr	Mn	Si	V	Mo	S	Cu	Al	P	Ni	N
B360	0.269	0.51	1.547	1.36	0.033	0.148	-	-	-	-	-	0.006
B1400	0.363	1.146	0.934	0.694	0.095	0.713	0.0009	0.242	-	-	0.223	0.008
CrB	0.367	2.722	0.726	0.595	0.109	0.3	0.0008	0.05	0.0069	0.0059	0.059	0.009
R350HT	0.72	0.11	1.1	0.5	-	-	-	-	0.004	0.02	-	-

The different bainitic steel grades, including B360, B1400, chrome bainitic (CrB) in as-received (AR) and heat-treated (HT) conditions and pearlitic R350HT steel, were compared for their mechanical performance under uniaxial tensile experiments. The samples were cut and prepared using electron discharge machining (Makino, Tokyo, Japan) in combination with turning and polishing on lathe machine from the real rail specimens (as shown in Figure 3.1).

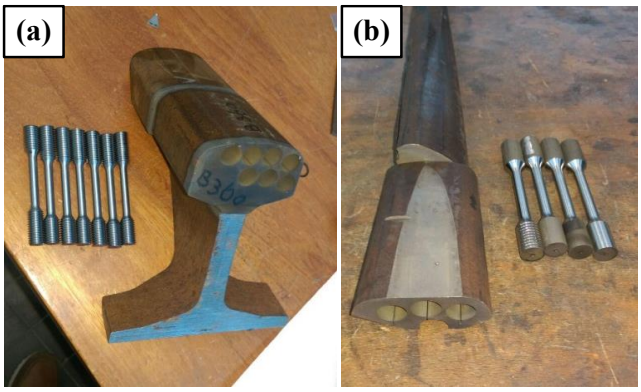

Figure 3.1. Sample preparation for uniaxial tensile test machine; (a,b) Images of specimens cut from real used rails.

For each grade, samples with the geometry shown in Figure 3.2 and with dimensions presented in Table 3.2 were cut and prepared. Heat treatment was performed on these samples. The uniaxial tensile test in each condition was performed on at least three samples to make sure that the results were reliable and representative.

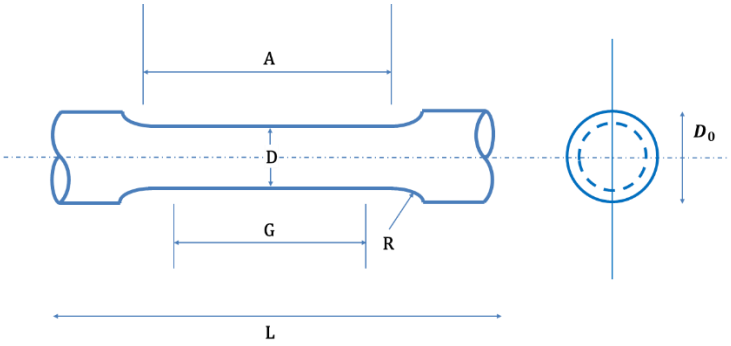

Figure 3.2. Tensile sample dimensions.

Table 3.2. Tensile sample dimension.

G (Gauge length)	30.0 ± 0.1 mm
D (Diameter)	6.0 ± 0.1 mm
R (Minimum radius of fillet)	6 mm
A (Minimum length of reduced section)	36 mm
L (Full specimen length)	85 ± 5 mm
D_o (Diameter of the gripping section)	≥12 mm

In as-received condition, B360-AR and CrB-AR steel grades were produced by austenitization followed by continuous cooling to room temperature, while B1400-AR grade is isothermally heat treated with a hold at 400 °C for 30 min. To optimize both strength and toughness of the steels, the isothermal heat treatment shown in Figure 3.3 was used for the bainitic grades. The heat-treatment process involves first heating the samples up to 900 °C and keeping them there for 10 min (600 s). Afterwards, specimens were brought to 330 °C to be austempered for 60 min (3600 s) and subsequently oil quenched to room temperature.

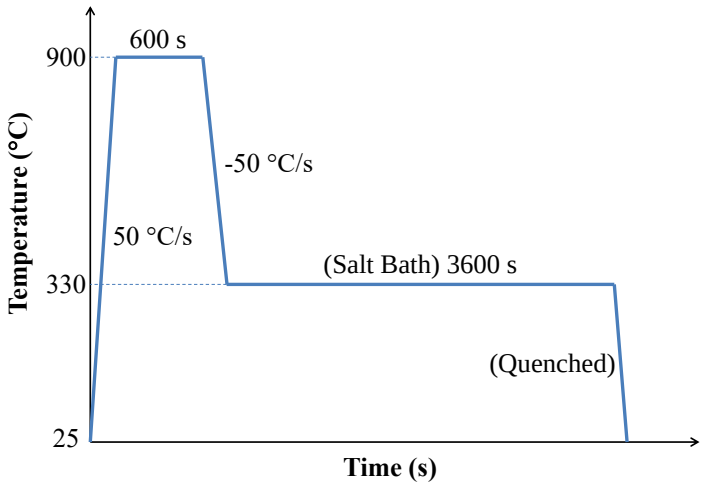

Figure 3.3. Scheme of the planned heat-treatment process.

3.2.2 Uniaxial Tensile Testing

Uniaxial tensile tests were performed at the room temperature on an INSTRON 2200 machine with a constant cross head speed of 1 mm/min. The strain values were measured using a knife edge extensometer (INSTRON, Boechout, Belgium) with a gauge dimension of 12.5 mm. The stress-strain diagrams for each steel were plotted. The mechanical properties such as yield strength, ultimate tensile strength, uniform elongation, engineering fracture strain, toughness and strain hardening exponent (SHE) were calculated from the resulting stress-strain diagram. The value of yield strength was taken at 0.2% engineering strain. The broken samples were further investigated for the fracture surface analysis on a Keyence VHX-5000 optical microscope (Keyence, Mechelen, Belgium). Reduction of area and true fracture strain, which are good measures for ductility, were measured using the fracture surface analysis.

3.2.3 Hardness Measurement

Hardness measurements were performed on a DuraScan 70 Vickers micro hardness tester (EMCO-TEST, Kuchl, Austria) under a load of 0.1 kgf on different steel grades. The measurement results are shown in Section 3.3.4.

3.2.4 Microstructural Characterization

The specimens from the bainitic steels were prepared for metallographic observation using conventional grinding followed by polishing using the diamond paste, having particle size of 3 and 1 μm, respectively. Afterwards, the specimens were etched using 2 vol % solution of nitric acid in ethanol (2% Nital) to reveal the microstructure under the light optical microscopy (LOM) and scanning electron microscopy (SEM). For

LOM, a Keyence VHX-5000 (Keyence, Mechelen, Belgium) was used. The SEM imaging was conducted on a JEOL JSM-IT100 microscope (JEOL Ltd., Tokyo, Japan) with a tungsten filament. The imaging was conducted with an accelerating voltage of 30 kV and working distance of 10 mm. The EBSD characterization was performed using a FEI Quanta-450 SEM (FEI Company, Hillsboro, OR, USA) equipped with a field emission gun (FEG). A Hikari-Pro EBSD detector in combination with EDAX-TSL OIM Data Collection v.6.2 software (AMETEK BV, Tilburg, the Netherlands) was used for EBSD data collection. The EBSD measurements were performed with an accelerating voltage of 15 kV with a step size of 50 nm. The hexagonal scan grid mode was used for EBSD data collection. The EBSD data were further analyzed using a TSL OIM v. 7.0 software (AMETEK BV, Tilburg, the Netherlands) and phase fractions and grain sizes were determined. All points having a confidence index less than 0.1 were excluded from quantification during this analysis.

3.3 Results and Discussion

3.3.1 Tensile Tests

The results of the tensile tests are presented in Figure 3.4 and Table 3.3. All the stress-strain curves are illustrated in Figure 3.4(a). Figure 3.4(b) shows the comparison of the engineering uniform and fracture strain of these steels. Among the bainitic steels in as-received condition, B360-AR has the highest engineering fracture strain (19.9 ± 0.9%). The uniform strain is the strain up to maximum load and it is usually used to describe the formability of metals. B360-AR has also the highest uniform strain (16.6 ± 0.8%).

During necking, the cross section of the samples changes, so true fracture strain is used to accurately define the straining of ductile materials by considering the actual cross-section area after fracture. The true fracture strain is calculated using the reduction of area in the tensile specimens. Reduction of area is an important material characteristic that indicates the ductility of the material. Reduction of area (ΔA) and true fracture strain (ε_f) are calculated by:

$$\Delta A = \frac{A_0 - A_{min}}{A_0} \tag{3.1}$$

$$\varepsilon_f = ln\frac{A_0}{A_{min}} = ln\frac{1}{1 - \Delta A} \tag{3.2}$$

where A_0 is the area of original cross section and A_{min} is the minimum final cross section after fracture.

It is observed in Figure 3.4(c) that all bainitic steels also show a higher true fracture strain than the R350HT pearlitic grade. Comparing bainitic grades in as-received

condition, B1400-AR had the highest true fracture strain (99.4 ± 3.1%). The reason for the large difference in ductility (for as-received samples) is due to the isothermal heat treatment done on this rail steel (in industry) in contrast to the continuous cooling heat treatment that was performed on B360-AR and CrB-AR, which is explained more in Section 3.3.5 The isothermal heat treatment on bainitic steels increases the true fracture strain and hence increases the ductility. We observed that the true fracture strains of all bainitic steels are improved by the isothermal bainitic heat treatment. The true fracture strain of B1400-HT reaches to a value of around 167.1 ± 2.2%. However, the B360-HT steels show a true fracture strain of 171.4 ± 2.7% which is the highest among all steels.

Figure 3.4(d) shows the comparison of yield and ultimate tensile strength of all rail steels. All bainitic steels have higher yield and ultimate strength than the pearlitic R350HT steel. It is also observed that the yield and ultimate strength of all bainitic steels increase after the isothermal bainitic heat treatment. B360 has the highest increase compared to other steels, which results in B360-HT having the highest yield and ultimate strength of 1324 ± 17 and 1879 ± 19 MPa, respectively. This is due to its fine carbide-free bainitic structure, which is explained in Section 3.3.5. Among all as-received bainitic grades, B1400-AR shows the highest yield strength. This can be due to the isothermal bainitic heat treatment of B1400-AR at 400 °C (in industry) in contrast to other as-received bainitic grades, which were produced by continuous cooling of samples to the room temperature. CrB-AR has the highest ultimate strength compared to other two as-received bainitic steels.

Figure 3.4(e) shows the comparison of toughness of all steel grades. Toughness is the capacity of the material to absorb energy by elastic and plastic deformation. Toughness is measured as the area under the stress-strain curve. B360-AR shows the highest toughness among all steels. Heat treatment does not seem to increase the toughness of steels, and just CrB-HT has higher toughness than its as-received form. The reason is that heat treatment increases the strength of these steels, and this causes them to fracture in a lower engineering strain value compared to as-received situation.

3.3.2 Strain Hardening Exponent

The strain hardening exponent measures the ability of a material to strain harden. Larger magnitudes indicate higher rate of strain hardening. This exponent was measured for all steels using Hollomon's model [42]. The true stress-strain curve of the steels during the uniform plastic deformation can be approximated as a simple power curve relation:

$$\sigma_t = K\,\varepsilon_t^n \tag{3.3}$$

where σ_t is the true stress, ε_t is the true strain, n is the SHE and K is the strength coefficient. A log-log plot of this curve would result in a straight line. The slope of this line is calculated as strain hardening exponent (SHE).

Figure 3.4(f) shows the comparison of the measured SHEs for all steels. Pearlitic R350HT grade has the highest SHE (0.24 ± 0.005), while B1400-AR shows the lowest value for SHE. The exact values can be seen in Table 3.3.

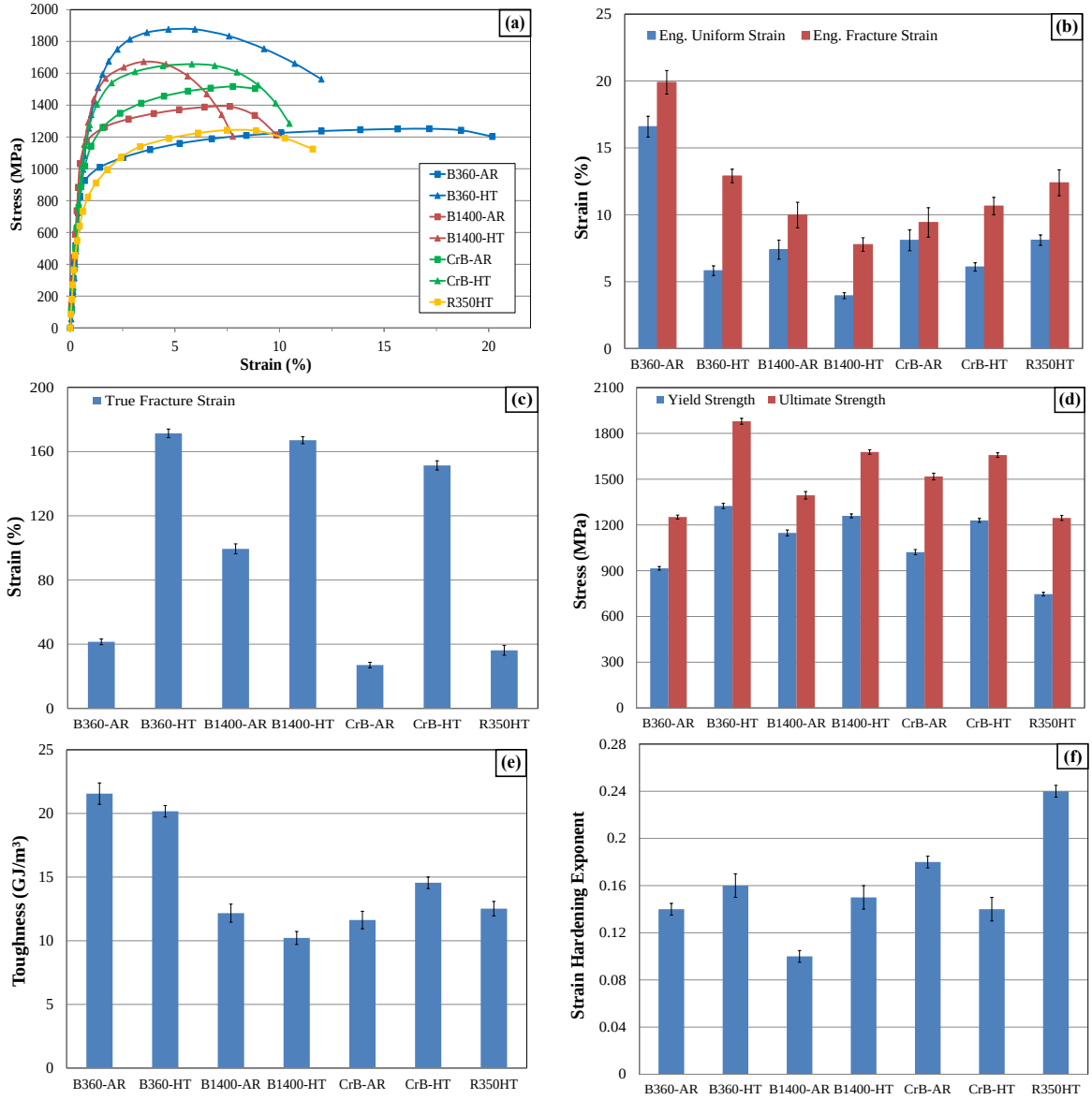

Figure 3.4. Comparison of mechanical properties of steels using results of the uniaxial tensile tests; (a) engineering stress-strain curves, (b) engineering uniform strain, engineering fracture strain, (c) true fracture strain, (d) yield and ultimate strength, (e) toughness and (f) strain hardening exponent (SHE).

Table 3.3. The values of mechanical (tensile) properties for each steel.

Steels	Eng. Fracture Strain (%)	Eng. Uniform Strain (%)	True Fracture Strain (%)	Yield Strength (MPa)	Ultimate Strength (MPa)	Toughness (GJ/m^3)	SHE (-)	Hardness (HV0.1)
B360-AR	19.9 ± 0.9	16.6 ± 0.8	41.5 ± 1.8	915 ± 12	1251 ± 13	21.5 ± 0.8	0.14±0.005	380 ± 8
B360-HT	12.9 ± 0.5	5.8 ± 0.4	171.4 ± 2.7	1324 ± 17	1879 ± 19	20.2 ± 0.4	0.16 ± 0.01	545 ± 9
B1400-AR	9.98 ± 0.9	7.4 ± 0.7	99.4 ± 3.1	1147 ± 19	1394 ± 25	12.2 ± 0.7	0.10±0.005	510 ± 15
B1400-HT	7.77 ± 0.5	3.9 ± 0.2	167.1 ± 2.2	1260 ± 13	1678 ± 14	10.2 ± 0.5	0.15 ± 0.01	533 ± 7
CrB-AR	9.4 ± 1.1	8.1 ± 0.8	27.0 ± 1.7	1021 ± 17	1517 ± 22	11.6 ± 0.7	0.18±0.005	460 ± 13
CrB-HT	10.6 ± 0.6	6.1 ± 0.3	151.4 ± 2.9	1229 ± 13	1657 ± 15	14.5 ± 0.4	0.14 ± 0.01	537 ± 7
R350HT	12.4 ± 0.9	8.1 ± 0.4	36.2 ± 3.1	746 ± 11	1245 ± 16	12.5 ± 0.6	0.24±0.005	350 ± 10

3.3.3 Fracture Surface Analysis

Figure 3.5 shows the fracture surface analysis of the broken tensile samples, which were characterized using LOM. During ductile fracture, extensive plastic deformation occurs, which leads to necking. The necking is followed by the void formation and coalescence of these voids to form cracks. These cracks propagate in the material, and the failure leads to a cup-and-cone-type fracture surface. In contrast to ductile fracture, brittle fracture happens with limited plastic deformation. Cracks propagate rapidly, and their direction is perpendicular to the applied load, leaving a fracture surface equal to the cross section of the sample. In Figure 3.5(a),(b) the fracture surface of the as-received and heat-treated B360 steel in 2D and 3D is shown. It can be observed that after the heat treatment, this steel becomes more ductile, and the fracture area changes from brittle like to a cup-and-cone form. Using Equation (3.1), the B360-AR and B360-HT show the ΔA value of 34.3 ± 1.5% and 82.1 ± 1.4%, respectively. Figure 3.5(c),(d) illustrates the fracture surface of B1400-AR and B1400-HT, respectively. It can be observed that B1400-AR is not fracturing in a complete brittle way as in the case of other as-received bainitic steels and pearlitic R350HT. Isothermal bainitic heat treatment at 330 °C for 1 h makes this steel even more ductile than compared to in as-received condition with an increase in ΔA from 63.4 ± 2.1% to 81.1 ± 1.2%.

Figure 3.5(e),(f) shows the fracture surface of CrB steels before and after isothermal heat treatment. CrB-AR fractures in a brittle like manner while after the heat treatment, this steel shows much more ductile fracture behavior with a cup-and-cone fracture surface. The value ΔA in CrB steels increases from 23.9 ± 1.7% to 78.2 ± 2.1% after the isothermal heat treatment. R350HT pearlitic steel shows the least ductile fracture behavior with an ΔA of 30.5 ± 2.6% and shows a brittle like fracture surface (Figure 3.5(g)). To conclude the fracture surface analysis, we observe that the microstructure after heat treatment causes a much more ductile behavior (as was also observed from

tensile tests data) with a higher ΔA percentage (and hence higher true fracture strain) compared to as-received cases. Except for B1400-AR which showed a cup-and-cone fracture surface (for the reason which is explained in Section 3.3.5), all the other as-received samples show a brittle type fracture surface.

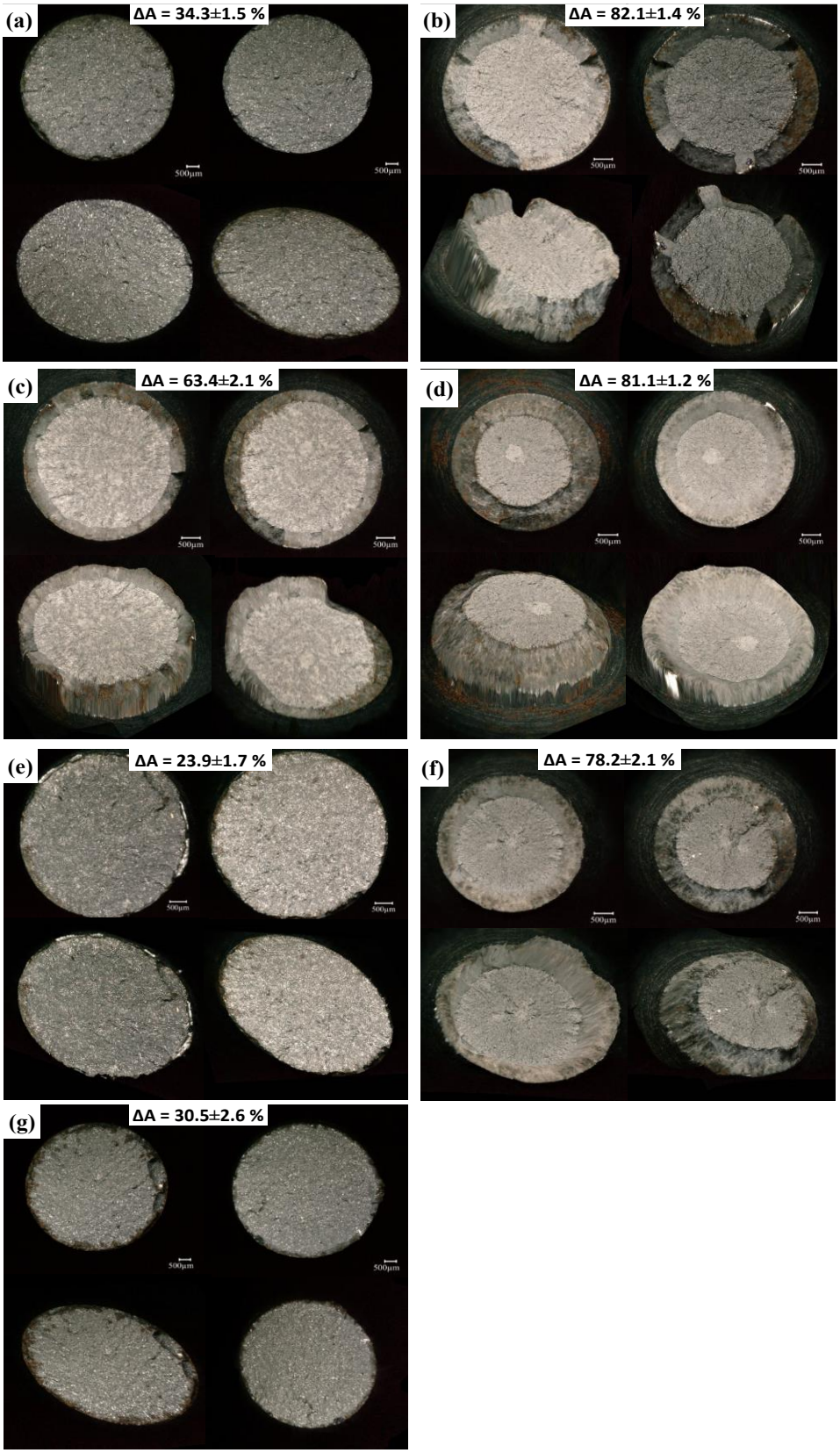

Figure 3.5. The fracture surfaces and reduction of area (ΔA) of all tensile samples, up (2D image) and down (3D image); (a) B360-AR, (b) B360-HT, (c) B1400-AR, (d) B1400-HT, (e) CrB-AR, (f) CrB-HT and (g) R350HT.

It is reported that high tensile strength rail steels are less susceptible to RCF damage [43]. Therefore, the preferred situation would be the design of high-strength steels, one variant of which is achieved via the isothermal bainitic transformation. Considering the comparison of the mechanical properties and RCF damage resistance among all steels, B360-HT would be the best choice due to its very high strength, good ductility and toughness.

3.3.4 Hardness

The hardness of the steel grades was measured and compared, as shown in Figure 3.6. It is observed that hardness increases after the heat treatment for all steel grades. In general, all heat-treated steels and B1400-AR show hardness value above 500 HV. R350HT has the lowest hardness among all steels. Grain size and the phase fraction of harder phases (such as martensite) have large influence on the hardness values, which is further explained in Section 3.3.5.

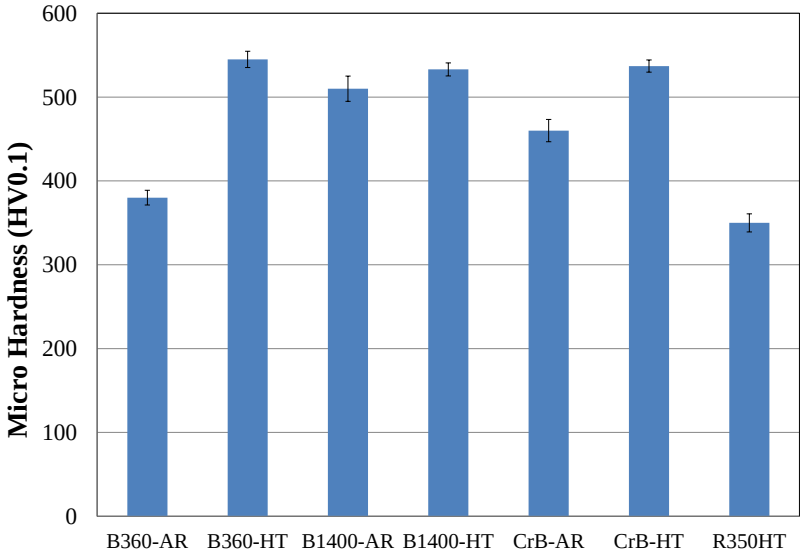

Figure 3.6. Hardness of all steels (HV0.1).

3.3.5 Influence of Microstructure on Mechanical Properties

There have been several studies on the relationship between the mechanical properties and damage development in rail steels [43–45]. One of these studies showed that using steels with higher hardness and tensile strength reduces the wear and RCF damage in rails [43]. Although it is believed that using softer rails helps removing the RCF cracks due to wear, the RCF damage development is also influenced by the wear rate of the steels. Due to faster wear, the rail profile changes, and the contact patch becomes larger, which eventually leads to lower contact stresses in the wheel–rail interface [43]. A study on the German railways showed that not only the wear but also the RCF (head

checks) crack growth was reduced significantly by using head-hardened 350HT rails compared to the pearlitic 220, 260 rail grades [44]. The 220 grade had the highest crack depth and 350HT the lowest [44]. In another study, it was shown that, with an increase in the rail hardness, the wear in rail will decrease but, depending on the wheel hardness, wheel wear can increase or remain constant. In this case, if the wheel is harder than the rail, wheel wear increases, and if the wheel is softer than the rail, wheel wear remains constant. However, in both cases, increasing rail hardness reduces overall system wear [45].

As was mentioned, mechanical properties and failure in steels are strongly governed by their microstructures. The bainitic steels in as-received condition are complex mixtures of upper and lower bainite in combination with martensite and carbides. The lower the bainitic transformation temperature, the finer the bainitic structure is, and it results in higher hardness, toughness and wear resistance [46]. Furthermore, minimizing the martensite and cementite fractions in the microstructure contributes to improved damage resistance [46]. In another study, the comparison between bainitic structures isothermally transformed at 330 °C (lower bainite) and 425 °C (upper bainite) showed that steels with lower bainite structure have finer and more uniform distribution of carbides and lower bainitic ferrite plates. Together with the higher dislocation density in lower bainite, this results in higher tensile strength, elongation and impact energy properties than for the upper bainite [47]. In the next sections, the difference in the microstructure of the bainitic steels, the effect of isothermal heat treatment on their microstructure and the influence of microstructure on the measured mechanical properties are discussed based on the results obtained via LOM, SEM and EBSD.

We did investigation on the samples using LOM on polished and non-etched samples at magnification up to 250×, and we did not find any visible non-metallic inclusions (MnS or oxides) at this magnification (see supplementary information).

3.3.5.1 B360 Grade

Figure 3.7(a) shows the LOM of the carbide-free bainitic B360-AR. The continuous cooling causes the bainitic transformation in different temperature ranges to form two morphologies of bainite, i.e., upper bainite (UB) and lower bainite (LB). The UB is formed at relatively high temperature just below bainitic start temperature, while LB, which has a lamellar structure of lath bainitic ferrite (BF) and thin film retained austenite (TFRA), forms at rather low temperature just above martensitic start temperature [27–30]. Simultaneously, the formation of bainite during the continuous cooling is not complete due to limited transformation time. This leads to large areas of untransformed retained austenite (RA), which later remains as blocky retained austenite (BRA) or transforms into martensite (M). In Figure 3.7(a), locations of LB, which is a lamellar structure consisting of BF (dark) and TFRA (bright) lamellae, and

also locations of bright patches of M/BRA can be observed. Figure 3.8(a) shows the SEM image of B360-AR microstructure, indicating the presence of fine bainite (LB), coarse bainite (UB) and islands of blocky retained austenite (BRA) and martensite (M).

It is common design strategy in bainitic steels to avoid incomplete bainitic transformation, since the remaining austenite (which does not transform into bainite) could later transform into martensite during further cooling or under mechanical load. This brittle M phase reduces the toughness of the steel [48]. For this purpose, low transformation temperature at 330 °C was selected for isothermal heat treatment and enough time was given to maximize the bainitic fraction (Figure 3.3). This also leads to formation of a fine bainitic microstructure with good mechanical properties, as shown above. The resulting carbide-free low bainitic microstructure in B360-HT (Figure 3.7(b) and Figure 3.8(b)) contains mainly fine lath bainitic ferrite and thin film retained austenite with small-sized homogeneously distributed blocky retained austenite, whereas B360-AR has a microstructure of low bainite and large zones (islands) of blocky retained austenite and martensite (Figure 3.7(a) and Figure 3.8(a)).

The small-size BRA islands observed in B360-HT usually contain higher carbon concentration due to carbon partitioning during the bainite formation and are mechanically and thermally more stable [48–52]. The carbide-free fine bainitic microstructure of B360-HT consists of approximately 2.2 ± 1.0% of blocky retained austenite (BRA) having an average size of 463 ± 61 nm, as shown in Table 3.4. Another research, which was performed on the carbide-free bainitic steel with the same composition and isothermal bainitic treatment, shows that the BRA islands less than 250 nm in size in carbide-free bainitic steels are mechanically stable and do not transform into martensite during the tensile fracture [53]. Thus, the BRA islands in B360-HT will partially transform into martensite during the tensile fracture and small BRA islands (<250 nm), and TFRA would be stable during the tensile fracture. The mechanical stability of the small BRA islands is governed by the C enrichment in these islands due to high bainitic ferrite fraction [54,55]. Furthermore, thin film retained austenite (TFRA) in this steel is even more mechanically stable than BRA due to constraints from bainitic ferrite, high defect density in the TFRA due to displacive bainitic transformation and high C enrichment (up to 8 at. %) [53]. As mentioned above, the BRA fraction in B360HT is small (2.2 ± 1%), and the partial transformation to martensite will not affect the local strain partitioning and damage significantly [53]. In the same study, it is shown that the strain partitioning in this steel was homogenous due to its uniform microstructure, which leads its good mechanical performance and high damage resistance [53].

Large BRA present in B360-AR is less stable to transformation due to the lower carbon content in large blocks, which contributes to an increase in the martensitic fraction upon mechanical loading via strain induced transformation of austenite into martensite [54]. This transformation increases the overall fraction of brittle martensite

phase in the microstructure, which leads to brittle-like fracture response (Figure 3.5) and lower toughness [48]. It was shown that in B360-AR bainitic steel, micro-cracks initiate primarily at the weak interfaces between martensite and bainitic ferrite. [55–57].

Figure 3.9(a) shows superimposed Image Quality (IQ) and phase maps of the B360-HT steel. The maps illustrate that there is mainly bainite (LB) and BRA with area fraction of 97.8 ± 1.0% and 2.2 ± 1.0%, respectively (Table 3.4). The average calculated bainitic lath diameter is 2391 ± 348 nm, and average grain diameter for blocky retained austenite is 463 ± 61 nm (Table 3.4). We do not observe areas with low IQ in Figure 3.9(a). This indicates that there is no M present in the B360-HT microstructure. This explanation is based on the fact that the martensite phase contains a high dislocation density, which deteriorates the IQ in the EBSD measurements [49–51]. The ductile fracture of the B360-HT steel is due to its carbide/martensite free fine bainitic microstructure. The brittle microstructural constituents, such as cementite and martensite, are not present in the microstructure due to high Si content and isothermal bainitic transformation, respectively.

In conclusion, the isothermal bainitic heat treatment leads to the avoidance of martensite and large blocky retained austenite and also produces much finer bainitic structure as LB, which primarily contains more stable TFRA laths sandwiched between lath BF.

3.3.5.2 B1400 Grade

The B1400 steels contain lower concentration of Si than the carbide-free B360 grade (Table 3.1). Si suppresses the precipitation of carbide (cementite) from retained austenite [36,37]. This is why B1400 steels are prone to having bainitic ferrite together with carbides in the microstructure during bainitic transformation. The microstructures of B1400-AR and B1400-HT are presented in Figure 3.7(c),(d), respectively.

As can be observed in Figure 3.7(c), B1400-AR contains finer bainitic microstructure compared to the other two as-received steels. The reason, as mentioned before, is that the as-received steel was treated in an isothermal bainitic transformation at 400 °C for 30 min (in industry). The higher bainitic transformation temperature leads to a coarser bainitic microstructure [46]. The holding time for bainitic transformation for the rails was not sufficiently long so that it led to the presence of some BRA/M islands in the microstructure. Figure 3.7(c) shows the presence of lower bainite together with M/BRA islands. Looking at higher magnification in Figure 3.8(c) indicates the presence of carbide (cementite) precipitates. These carbides exist in two different morphologies, i.e., spherical and lath-shaped. The geometrical measurements of these carbides were done using image processing tools in the ImageJ software in different locations on the

SEM image (Figure 3.8(c)). Based on these measurements, the average diameter of the spherical carbides is 144 ± 28 nm, and the average thickness of lath-shaped carbides is 128 ± 15 nm (Table 3.5). The average distance between the carbides in B1400-AR is also obtained using combination of ImageJ software and MATLAB. This distance was measured to be 1225 ± 89 nm (Table 3.5).

We performed isothermal heat treatment on B1400-AR steels at 330 °C for 1 h, and relatively fine bainitic microstructure is obtained after this heat treatment, as shown in Figure 3.7(d) and Figure 3.8(d). The resulting microstructure contains nano-sized carbides (NSC) with average diameter of 106 ± 21 nm, which is smaller than the measured diameter for B1400-AR (144 ± 28 nm), as can be seen in Table 3.5. The average distance between these NSCs was measured to be 620 ± 89 nm (compared to 1225 ± 89 nm for B1400-AR), as can also be seen in Table 3.5. This shows that NSCs, which precipitate within the lower BF laths, are smaller and more closely spaced inside B1400-HT compared to B1400-AR. These NSCs are expected to act as obstacles to the dislocation motion and will improve the yield strength of the B1400-HT steel [58]. Figure 3.8(d) also shows the presence of inter-lath thin film retained austenite (TFRA) in between the BF laths. On the other hand, the relatively longer holding period maximizes the bainitic fraction (with LB morphology) and suppresses the martensitic transformation. No M is present in B1400-HT, as indicated by IQ data shown in Figure 3.9(b). This enhances the ductility of the heat-treated steel and leads to more ductile fracture response compared to as-received condition (Figure 3.5). There are still islands of BRA, as shown in Figure 3.8(d). The green color in Figure 3.9(b) shows the BRA inside the B1400-HT microstructure with fraction of 2.8 ± 0.7%, as given in Table 3.4. The average lath diameters of bainite and BRA grain diameter inside B1400-HT are 2641 ± 478 nm and 530 ± 71 nm respectively (Table 3.4).

To summarize, the finer bainitic microstructure of B1400-HT than B1400-AR and avoidance of M phase in B1400-HT, containing closely spaced nano-sized carbides (NSCs) inside the bainitic laths and also presence of small BRA, which is more stable than bigger islands of BRA, produce a microstructure with better strength and ductility compared to as-received steel.

3.3.5.3 CrB Grade

The LOM and SEM images of CrB-AR microstructure are shown in Figure 3.7(e) and Figure 3.8(e). This steel contains brittle phases like martensite and carbides due to incomplete bainitic transformation. Presence of these phases leads to poor mechanical properties and more brittle fracture response (Figure 3.5). Carbides are considered to be bad for fatigue life as well [48]. The geometrical properties of the carbides were also measured using the same method as used for B1400. The average diameter of the carbides is 127 ± 24 nm, and the average distance between these carbides is 1069 ± 55 nm (Table 3.5). Isothermal heat treatment is performed on this steel to suppress the

untransformed regions of austenite by maximizing bainitic transformation. This suppresses the formation of brittle martensite in the microstructure. A much finer microstructure compared to CrB-AR results (comparing Figure 3.7(e),(f)). Looking at higher magnification in Figure 3.8(f) shows that the microstructure after the heat treatment primarily contains LB (combination of BF, TFRA and NSC) with smaller size BRA islands (compared to as-received microstructure). Comparing Figure 3.8(e),(f) shows that there is a change in shape and size of carbides. The average diameter of these carbides was measured to be 79 ± 13 nm, and the average distance between them was 550 ± 21 nm (Table 3.5). This means CrB-HT has smaller carbides (mostly as NSC), which are closely spaced with respect to each other and this increases the yield strength of CrB-HT compared to the as-received condition [58].

According to EBSD maps of CrB-HT presented in Figure 3.9(c)–(e), there is still 3.8% M (as darker areas) present in the microstructure (in contrast to no M in other two heat-treated steels). Figure 3.9(d) illustrates the M islands distribution in CrB-HT, while Figure 3.9(e) shows the distribution of BRA phase in addition to M. The main difference of CrB-HT compared to other two heat-treated steels is the presence of M. This can be due to the fact that the CrB grade contains high concentration of Cr (3 wt %). High content of Cr slows down the bainitic transformation kinetics [59–61]. This is why the CrB-HT contains a lower bainitic fraction than B360-HT or B1400-HT for a given isothermal holding time, which naturally means that there is higher fraction of untransformed regions in the microstructure in the same heat-treatment condition. From EBSD phase map for CrB-HT, there is 3.3 ± 0.8% BRA with average grain diameter of 327 ± 55 nm and bainite with average lath diameter of 2100 ± 358 nm, as shown in Table 3.4.

Comparing CrB-AR and CrB-HT, it appears that the isothermal heat treatment creates finer microstructure with smaller BRA islands and more uniform distribution of closely spaced nano-sized carbides inside the bainitic laths in these steel grades that reflects the better mechanical properties in the heat-treated steel compared to as-received one.

For all the heat-treated samples, we did the reconstruction of the prior austenite grains (PAGs) to see if there were any significant differences in the prior austenite grain size (PAGS) of different steels. However, the observed difference in PAGS is not significant and does not exceed 8% (see supplementary information). It should be noted that the difference in bainitic lath sizes in the heat-treated steels would not be significantly affected by such small difference in PAGS. This difference in bainitic lath sizes (Table 3.4) would primarily be due to the difference in chemical composition of different steels than their PAGS. For more information about PAGS calculations, the reader is referred to the supplementary information of the article.

Table 3.4. The comparison of microstructural constituents in heat-treated samples.

Steel	Bainite Average Lath Diameter (nm)	BRA Area Fraction (%)	BRA Average Grain Diameter (nm)	Martensite Area Fraction (%)
B360-HT	2391 ± 348	2.2 ± 1.0	463 ± 61	~0
B1400-HT	2641 ± 478	2.8 ± 0.7	530 ± 71	~0
CrB-HT	2100 ± 358	3.3 ± 0.8	327 ± 55	3.8 ± 0.9

Table 3.5. The morphological characteristics of carbides in B1400 and CrB steels.

Steel	Average Carbide Size (diameter) (nm)	Average Distance between Carbides (nm)	Average Width of Lath-Shaped Carbides (nm)
B1400-AR	144 ± 28	1225 ± 89	128 ± 15
B1400-HT	106 ± 21	620 ± 89	-
CrB-AR	127 ± 24	1069 ± 55	-
CrB-HT	79 ± 13	550 ± 21	-

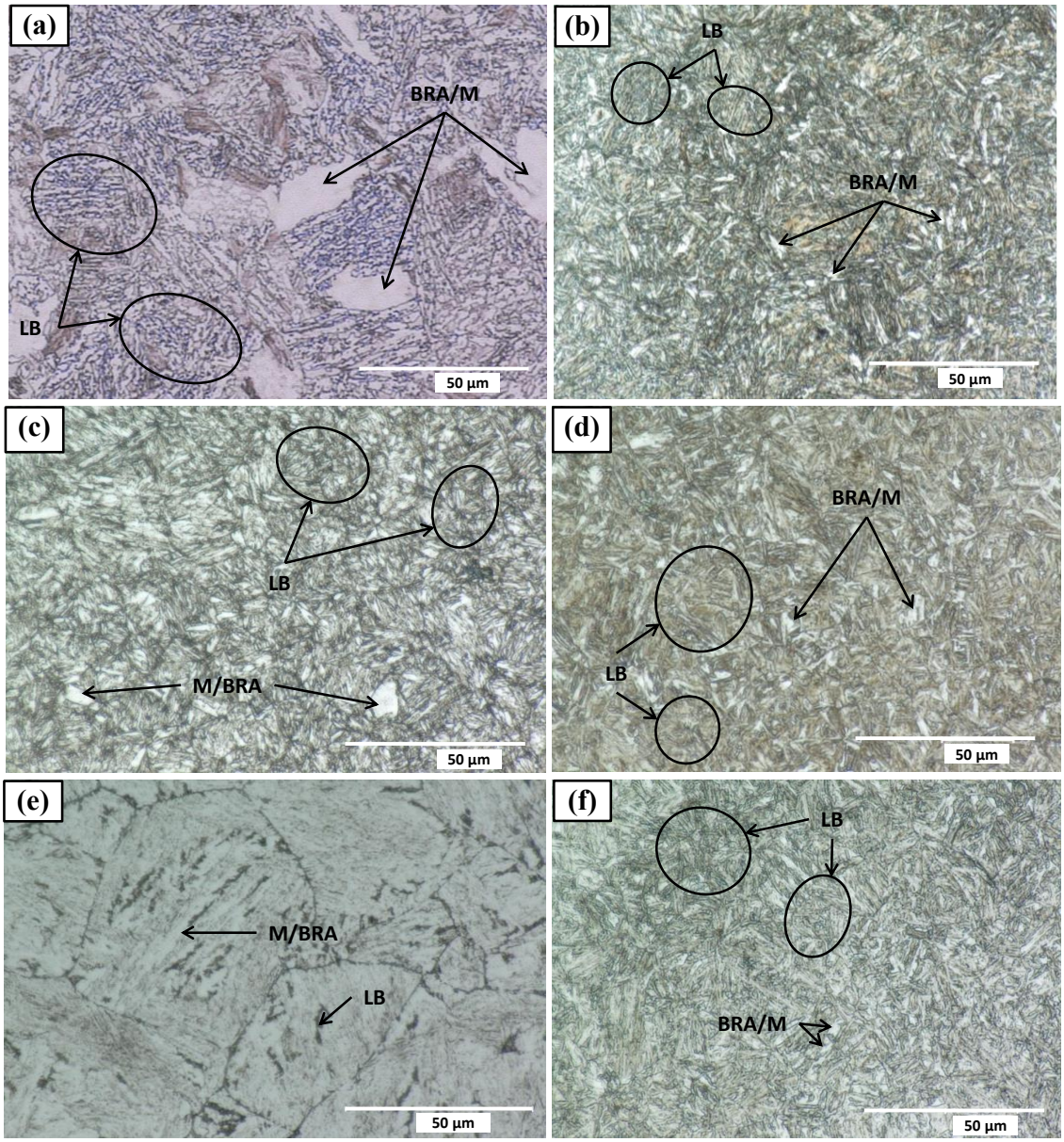

Figure 3.7. Light optical microscopy LOM images of all bainitic steels; (a) B360-AR, (b) B360-HT, (c) B1400-AR and (d) B1400-HT, (e) CrB-AR, (f) CrB-HT.

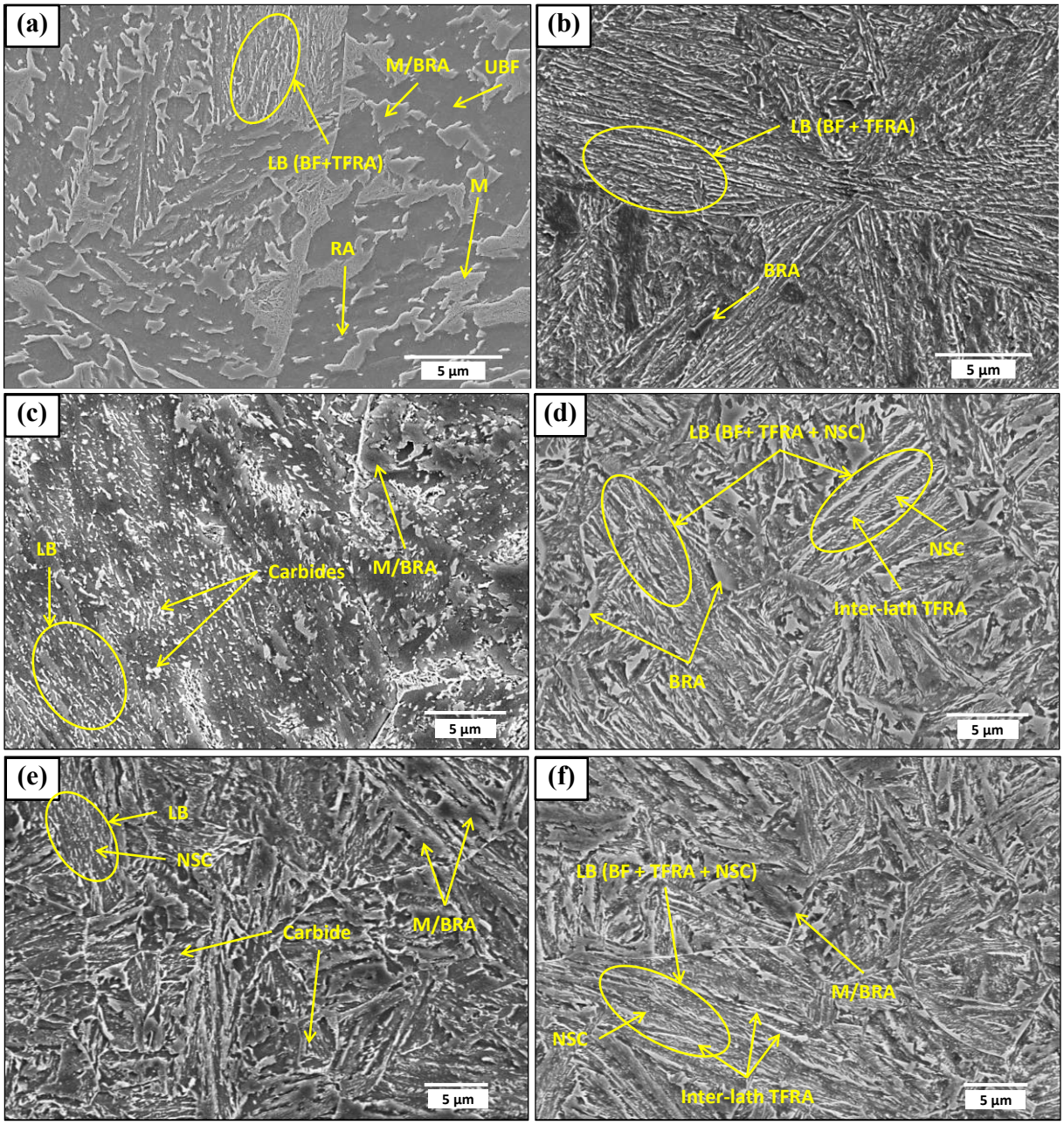

Figure 3.8. SEM images of all bainitic steels; (a) B360-AR, (b) B360-HT, (c) B1400-AR, (d) B1400-HT, (e) CrB-AR, (f) CrB-HT.

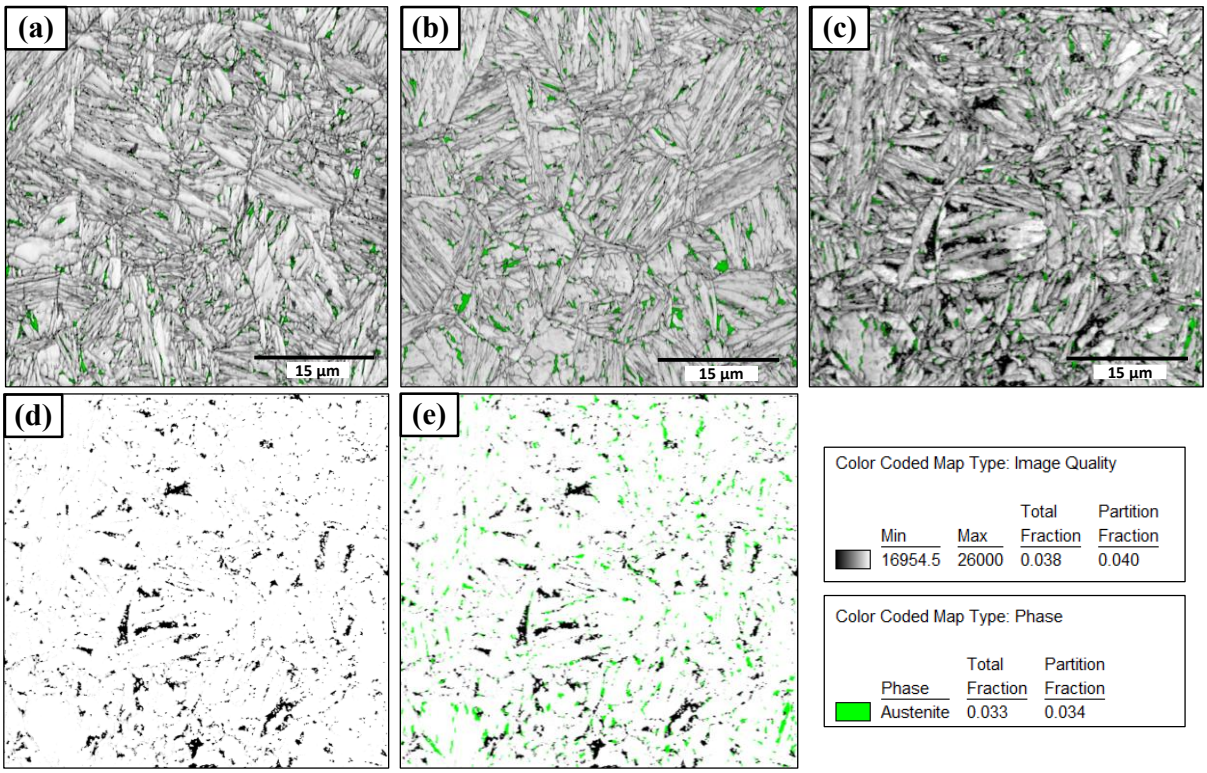

Figure 3.9. Electron backscatter diffraction (EBSD) maps of heat-treated grades; (a) image quality (IQ) and phase map of B360-HT, green color representing austenite phase, (b) IQ and phase map of B1400-HT, (c) IQ and phase map of CrB-HT, (d) IQ map of CrB-HT showing the M phase distribution (black), (e) IQ map and phase map of CrB-HT showing the M and austenite phase distribution.

In conclusion, investigating the microstructure of the bainitic steels reveals valuable information about the root causes of the measured mechanical properties. This investigation would give us good insight to choose the suitable material for our purpose. Since carbides have a bad effect on the fatigue properties of steels, B360-HT can be a good candidate in the case of fatigue loading. This steel also has high hardness (533 HV0.1) with a finer bainitic microstructure without any martensite or carbide. This would result in good resistance to wear and RCF damage development [46]. Thus, B360 carbide-free bainitic steel after an isothermal heat treatment is a good candidate to manufacture rails and S&Cs.

The loading in rails and switches and crossings (S&Cs) is different from and more complex than tensile load. Rails face the combination of compression and shear. However, the S&Cs are subjected to heavy dynamic impact loads. In future, a fatigue load combining shear and compression tests can be carried out to acquire more information regarding the material reaction to this kind of loading. Impact resistance of the material should also be investigated. Another important material property is the fracture toughness. Usually, rolling contact fatigue crack grows slowly and steadily up to a certain length but after this critical crack length, propagation rate increases

rapidly. Fracture toughness gives good insight regarding the crack growth rate and the critical crack length for RCF damage development in steels. The results of these tests combined and their interaction with the material microstructure could help to make an optimal design. These optimal designs can be used in different parts of railway infrastructure and ultimately lead to more sustainable railway networks.

It should be taken into consideration that, in order to reduce the damage in rails and S&Cs, not only must the right material for each section of a railway track be chosen but there should also be a good control of the loads on the rail during wheel–rail contact. These loads are dependent on factors such as track geometrical characteristics, train suspension system, track stiffness and damping characteristics, tribological properties and lubrication condition of wheel–rail interface.

3.4 Conclusions

The mechanical properties of three bainitic grades B360, B1400 and CrB in as-received and heat-treated conditions together with R350HT pearlitic steel were compared. For this purpose, uniaxial tensile tests and hardness measurements were performed on all steels. To study the influence of the microstructure on mechanical properties of bainitic steels, imaging techniques such as LOM, SEM and EBSD were used. The main conclusions of this study are as follows:

All three bainitic steels (irrespective of the heat treatment) perform better than the pearlitic R350HT steel regarding tensile strength, ductility and hardness.

By using low bainitic transformation temperature and providing enough time for it, nearly complete bainitic transformation is achieved. As a result, a finer bainitic microstructure with smaller-size blocky retained austenite (BRA) results (in comparison to the as-received steel), with almost no martensite (M). This change in the microstructure results in better mechanical properties.

For B1400-HT and CrB-HT grades, isothermal heat treatment results in smaller size of carbides (in comparison to the as-received steel), which are closely spaced to each other (mostly inside the bainite laths). This results in higher yield strength in heat-treated grades compared to as-received conditions.

The hardness of bainitic steels increases with heat treatment due to production of large fraction of lower bainite (LB), which is finer, stronger and harder than upper bainite (UB).

The highest strength, ductility and toughness among all steels investigated here were obtained in B360-HT. These improved properties are associated with the absence of carbides and martensite and formation of fine bainitic microstructure, which consists

of bainitic ferrite (BF) laths, thin film retained austenite (TFRA) and small and homogeneously distributed BRA.

3.5 References

[1] Clayton, P.; Allery, M.B.P. Metallurgical Aspects of Surface Damage Problems in Rails. Can. Met. Q. 1982, 21, 31–46.

[2] Dollevoet, R. Design of an Anti Head Check profile based on stress relief. PhD Thesis, University Library/University of Twente, Enschede, the Netherlands, 2010.

[3] Dollevoet, R.; Li, Z.; Arias-Cuevas, O. A Method for the Prediction of Head Checking Initiation Location and Orientation under Operational Loading Conditions. Proc. Inst. Mech. Eng. Part F: J. Rail Rapid Transit 2010, 224, 369–374.

[4] Li, Z.; Zhao, X.; Esveld, C.; Dollevoet, R.; Molodova, M. An investigation into the causes of squats—Correlation analysis and numerical modeling. Wear 2008, 265, 1349–1355.

[5] Deng, X.; Qian, Z.; Li, Z.; Dollevoet, R. Investigation of the formation of corrugation-induced rail squats based on extensive field monitoring. Int. J. Fatigue 2018, 112, 94–105.

[6] Wei, Z.; Núñez, A.; Boogaard, A.; Dollevoet, R.; Li, Z. Method for evaluating the performance of railway crossing rails after long-term service. Tribol. Int. 2018, 123, 337–348.

[7] Ueda, M.; Uchino, K.; Kobayashi, A. Effects of carbon content on wear property in pearlitic steels. Wear 2002, 253, 107–113.

[8] Hyzak, J.M.; Bernstein, I.M. The role of microstructure on the strength and toughness of fully pearlitic steels. Met. Mater. Trans. A 1976, 7, 1217–1224.

[9] Krauss, G.; Grossmann, M.A. Principles of heat treatment of steel; American Society for Metals: Metals Park, OH, USA, 1980; pp. 1890–1952.

[10] Kavishe, F.P.L.; Baker, T.J. Effect of prior austenite grain size and pearlite interlamellar spacing on strength and fracture toughness of a eutectoid rail steel. Mater. Sci. Technol. 1986, 2, 816–822.

[11] Gladman, T. Material Science and Technology; Wiley-VCH Verlag GmbH & Co. KGaA: Weinheim, Germany, 2006; pp. 402–432

[12] Pickering, F.B. Structure-Property Relationships in Steels. In Material Science and Technology; Wiley-VCH Verlag GmbH & Co. KGaA: Weinheim, Germany, 2006; pp. 43–81.

[13] Pérez-Unzueta, A.J.; Beynon, J.H. Microstructure and wear resistance of pearlitic rail steels. Wear 1993, 162, 173–182.

[14] Clayton, P.; Danks, D. Effect of interlamellar spacing on the wear resistance of eutectoid steels under rolling-sliding conditions. Wear 1990, 135, 369–389.

[15] Bouse, G.; Bernstein, I.; Stone, D. Role of Alloying and Microstructure on the Strength and Toughness of Experimental Rail Steels. In Rail Steels—Developments, Processing, and Use; ASTM International: West Conshohocken, PA, USA, 1978.

[16] Marich, S.; Curcio, P. Development of High-Strength Alloyed Rail Steels Suitable for Heavy Duty Applications. In Rail Steels—Developments, Processing, and Use; ASTM International: West Conshohocken, PA, USA, 1978.

[17] Smith, Y.E.; Fletcher, F.B. Alloy steels for high-strength, as-rolled rails. Am. Soc. Test. Mater. Spec. Tech. Publ. 1978, 11, 212–232. Available online: http://inis.iaea.org/search/search.aspx?orig_q=RN:10454787 (accessed on: 13 September 2018)

[18] Han, K.; Mottishaw, T.; Smith, G.; Edmonds, D.; Stacey, A. Effects of vanadium additions on microstructure and hardness of hypereutectoid pearlitic steels. Mater. Sci. Eng. A 1995, 190, 207–214.

[19] Han, K.; Smith, G.D.W.; Edmonds, D.V. Pearlite phase transformation in Si and V steel. Met. Mater. Trans. A 1995, 26, 1617–1631.

[20] Honeycombe, R.W.K.; Bhadeshia, H.K.D.H. Steels : Microstructure and Properties, 2nd ed.; Edward Arnold: New York, NY, USA, 1995.

[21] Kumar, A.; Agarwal, G; Petrov, R.; Goto, S.; Sietsma, J.; Herbig, M. Microstructural evolution of white and brown etching layers in pearlitic rail steels. Acta Materialia 2019, 171, 48-64

[22] Zuidema, B.K.; Subramanyam, D.K.; Leslie, W.C. The effect of aluminum on the work hardening and wear resistance of hadfield manganese steel. Met. Mater. Trans. A 1987, 18, 1629–1639.

[23] Peters, N.W. The Performance of Hadfield's Manganese Steel as It Relates to Manufacture. Available online: https://www.arema.org/files/library/2005_Conference_Proceedings/00040.pdf (accessed on 12 September 2018).

[24] Schmidova, E.; Hlavaty, I.; Hanus, P. The weldability of the steel with high manganese. Teh. Vjesn. - Tech. Gaz. 2016, 23, 749–752.

[25] Havel, D. Austenitic Manganese Steel: A Complete Overview. Available online: https://www.sfsa.org/doc/2017-4.1%20Columbia%20-%20Havel.pdf (accessed on 14 September 2018).

[26] Lewis, R.; Olofsson, U. Copyright. In Wheel–Rail Interface Handbook; Woodhead Publishing: Sawston, UK, 2009. doi:https://doi.org/10.1016/B978-1-84569-412-8.50029-X.

[27] Bain, E.C. Factors affecting the inherent hardenability of steel. J. Heat Treat. 1979, 1, 57–100.

[28] Ohtani, H.; Okaguchi, S.; Fujishiro, Y.; Ohmori, Y. Morphology and properties of low-carbon bainite. Met. Mater. Trans. A 1990, 21, 877–888.

[29] Ohmori, Y. Microstructural Evolutions with Precipitation of Carbides. ISIJ Int. 2001, 41, 554–565.

[30] Azuma, M.; Fujita, N.; Takahashi, M.; Senuma, T.; Quidort, D.; Lung, T. Modelling Upper and Lower Bainite Trasformation in Steels. ISIJ Int. 2005, 45, 221–228.

[31] Krauss, G.; Thompson, S.W. Ferritic Microstructures in Continuously Cooled Low- and Ultralow-carbon Steels. ISIJ Int. 1995, 35, 937–945.

[32] Bakhtiari, R.; Ekrami, A. The effect of bainite morphology on the mechanical properties of a high bainite dual phase (HBDP) steel. Mater. Sci. Eng. A 2009, 525, 159–165.

[33] Tomita, Y.; Okabayashi, K. Mechanical properties of 0.40 pct C-Ni-Cr-Mo high strength steel having a mixed structure of martensite and bainite. Met. Mater. Trans. A 1985, 16, 73–82.

[34] Pickering, F.B. Physical Metallurgy and the Design of Steels; Applied Science Publishers: London, UK, 1978. Available online: http://books.google.com/books?id=k5NTAAAAMAAJ (accessed on 5 August 2018).

[35] Bhadeshia, H.K. High Performance Bainitic Steels. Mater. Sci. Forum 2005, 500, 63–74.

[36] Sandvik, B.P.J.; Nevalainen, H.P. Structu re-property relationships in commercial low-alloy bainitic-austenitic steel with high strength, ductility, and toughness. Met. Technol. 1981, 8, 213–220.

[37] Bhadeshia, H.K.D.H; Edmonds, D.V. Bainite in Silicon Steels New Composition - Property Approach Part 1. Met. Sci. 1983, 17, 411–419.

[38] Long, X.; Kang, J.; Lv, B.; Zhang, F. Carbide-free bainite in medium carbon steel. Mater. Des. 2014, 64, 237–245.

[39] Wang, Y.; Zhang, F.; Wang, T. A novel bainitic steel comparable to maraging steel in mechanical properties. Scr. Mater. 2013, 68, 763–766.

[40] Sawley, K.; Kristan, J. Development of bainitic rail steels with potential resistance to rolling contact fatigue. Fatigue Fract. Eng. Mater. Struct. 2003, 26, 1019–1029.

[41] Clayton, P.; Devanathan, R.; Jin, N.; Steele, R.K. A Review of Bainitic Steels for Wheel/Rail Contact. In Rail Quality and Maintenance for Modern Railway Operation; Kalker, J.J., Cannon, D.F., Orringer, O., Eds.; Springer: Dordrecht, the Netherlands, 1993; pp. 41–51. doi:10.1007/978-94-015-8151-6_4.

[42] Hollomon, J.H. Tensile deformation. Trans. AIME 1945, 162, 268–290.

[43] Pointner, P. High strength rail steels—The importance of material properties in contact mechanics problems. Wear 2008, 265, 1373–1379.

[44] Heyder, R.; Girsch, G. Testing of HSH® rails in high-speed tracks to minimise rail damage. Wear 2005, 258, 1014–1021.

[45] Lewis, R.; Wang, W.J.; Burstow, M.; Lewis, S.R. Investigation of the Influence of Rail Hardness on the Wear of Rail and Wheel Materials under Dry Conditions Wear and RCF Mechanisms. Proc. Third Int. Conf. Railway Technol.: Res. Dev. Maintenance 2016, 5, 1–17. doi:10.4203/ccp.110.151.

[46] Shipway, P.; Wood, S.; Dent, A. The hardness and sliding wear behaviour of a bainitic steel. Wear 1997, 203, 196–205.

[47] Abbaszadeh, K.; Saghafian, H.; Kheirandish, S. Effect of Bainite Morphology on Mechanical Properties of the Mixed Bainite-martensite Microstructure in D6AC Steel. J. Mater. Sci. Technol. 2012, 28, 336–342.

[48] Bhadeshia, H.K.D.H. Bainite in Steels: Transformations, Microstructure and Properties; IOM Communications Ltd.: London, UK, 2001. Available online: https://books.google.co.id/books?id=sF5RAAAAMAAJ (accessed on 1 August 2018)

[49] Kunze, K.; Wright, S.I.; Adams, B.L.; Dingley, D.J. Advances in Automatic EBSP Single Orientation Measurements. Textures Microstruct. 1993, 20, 41–54.

[50] Wilson, A.; Madison, J.; Spanos, G. Determining phase volume fraction in steels by electron backscattered diffraction. Scr. Mater. 2001, 45, 1335–1340.

[51] Wu, J.; Wray, P.J.; Garcia, C.I.; Hua, M.; DeArdo, A.J. Image Quality Analysis: A New Method of Characterizing Microstructures. ISIJ Int. 2005, 45, 254–262.

[52] García-Mateo, C.; Caballero, F.G. The Role of Retained Austenite on Tensile Properties of Steels with Bainitic Microstructures. Mater. Trans. 2005, 46, 1839–1846.

[53] Kumar, A.; Makineni, S.; Dutta, A.; Goulas, C.; Steenbergen, M.; Petrov, R.; Sietsma, J. Design of high-strength and damage-resistant carbide-free fine bainitic steels for railway crossing applications. Mater. Sci. Eng. A 2019, 759, 210–223.

[54] Podder, A.S.; Lonardelli, I.; Molinari, A.; Bhadeshia, H.K.D.H. Thermal stability of retained austenite in bainitic steel: an in situ study. Proc. R. Soc. A: Math. Phys. Eng. Sci. 2011, 467, 3141–3156.

[55] Kumar, A.; Dutta, A.; Makineni, S.; Herbig, M.; Petrov, R.; Sietsma, J.; Makeneni, S. In-situ observation of strain partitioning and damage development in continuously cooled carbide-free bainitic steels using micro digital image correlation. Mater. Sci. Eng. A 2019, 757, 107–116.

[56] Hajizad, O.; Kumar, A.; Li, Z.; Petrov, R.H.; Sietsma, J.; Dollevoet, R. Micromechanical modelling of strain partitioning and damage initiation in a continuously cooled carbide free bainitic steel and validation using in-situ tensile experiment. Unpublished work, 2019.

[57] Hajizad, O.; Kumar, A.; Li, Z.; Petrov, R.H.; Sietsma, J.; Dollevoet, R. Crystal plasticity modelling of strain partitioning in high strength carbide free bainitic steel and validation using in-situ tensile experiments. Unpublished work, 2019.

[58] Skobir, D.A.; Vodopivec, F.; Kosec, L.; Jenko, M.; Vojvodič-Tuma, J.; Vojvodič-Tuma, J. Influence of Precipitates Size and Distribution on Room Temperature Mechanical Properties and Accelerated Creep of X20CrMoV121. Steel Res. Int. 2004, 75, 196–203.

[59] Bracke, L.; Xu, W. Effect of the Cr Content and Coiling Temperature on the Properties of Hot Rolled High Strength Lower Bainitic Steel. ISIJ Int. 2015, 55, 2206–2211.

[60] Tian, J.; Xu, G.; Zhou, M.; Hu, H.; Wan, X. The Effects of Cr and Al Addition on Transformation and Properties in Low-Carbon Bainitic Steels. Met. 2017, 7, 40.

[61] Zhou, M.; Xu, G.; Tian, J.; Hu, H.; Yuan, Q. Bainitic Transformation and Properties of Low Carbon Carbide-Free Bainitic Steels with Cr Addition. Met. 2017, 7, 263.

3.A. *Supplementary information for chapter 3*

3.A.1 *Effect of Non-Metallic Inclusions on the Mechanical Performance*

Figure 3.10 shows the optical micrographs of the B360, B1400 and CrB steels in non-etched condition. It was observed that all the steels do not have any visible inclusions at a magnification of 250x in the optical microscope. Thus, it can be concluded that the effect of non-metallic inclusions on the mechanical performance of different bainitic steels would either be similar or would not be affected significantly.

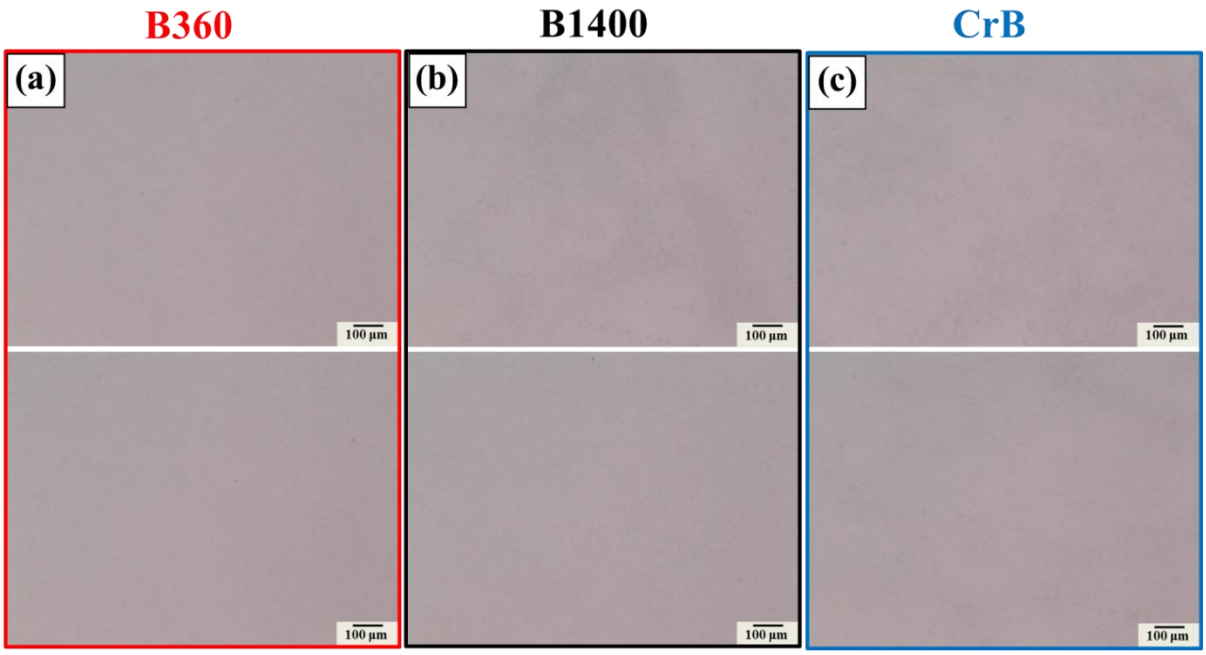

Figure 3.10. Optical Micrographs of different steels in non-etched condition (a) B360, (b) B1400, (c) CrB.

3.A.2 *Measurement of Prior Austenite Grain Size (PAGS)*

The bainitic transformation in different steels is affected by the PAGS and the chemical composition of the steels. Thus it is essential to reconstruct the prior austenite grains (PAGs) to see if there were any significant differences in the PAGS. Figure 3.11 shows the PAGs of the heat-treated microstructures which were reconstructed using ARPGE 2.4 software from the EBSD maps which were presented in Figure 3.9 (in the original manuscript). We considered N-W orientation relationships for the reconstruction. Then the PAGS was calculated using TSL OIM Analysis 7 ×64 software (AMETEK BV, Tilburg, the Netherlands) and shown in Table 3.6. The PAGS is the largest for B360-HT and the smallest for CrB-HT (Table 3.6). However, this difference in PAGS is not significant and does not exceed 8%. We believe that the difference in bainitic lath sizes

in the heat-treated steels would not be affected by such small difference in PAGS. But, this difference in packet size in Table 3.4 and Table 3.5 (in the manuscript), is primarily due to the difference in the chemical composition of the steels.

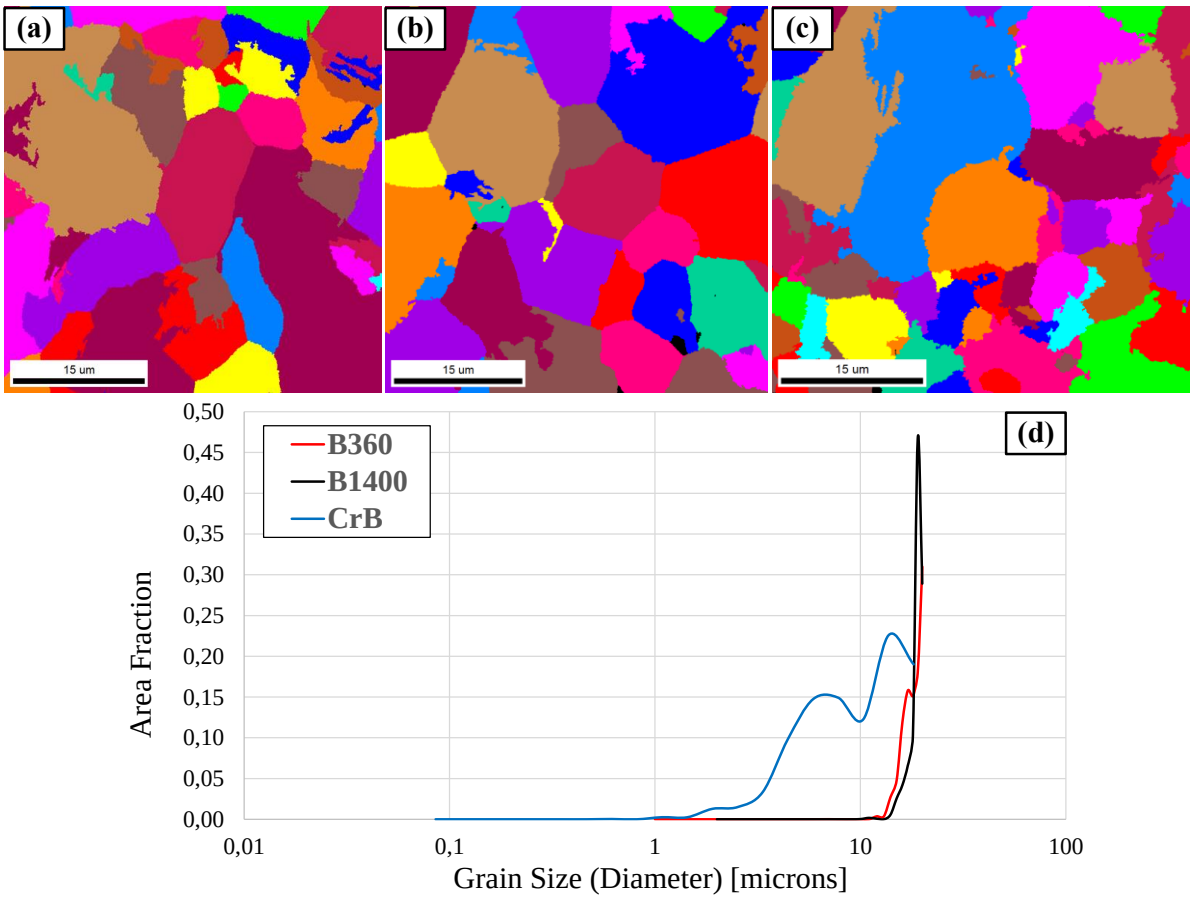

Figure 3.11. (a) Grain map showing the PAGs for B360-HT, (b) PAGs for B1400-HT, (c) PAGs for CrB-HT, (d) the grain size distribution for all steels.

Table 3.6. PAGS for heat treated steels.

Steels	PAGS (Average diameter)
B360-HT	12.1 ± 6.0
B1400-HT	11.6 ± 3.8
CrB-HT	10.8 ± 6.1

4 Strain partitioning and damage initiation in a continuously cooled carbide free bainitic steel †

Microscopic stress and strain partitioning control the mechanical and damage behavior of multiphase steels. Using a combined numerical and experimental approach, local strain distributions and deformation localization are characterized in a carbide free bainitic steel produced by continuous cooling. The microstructure of the steel consists of bainite (aggregate of bainitic ferrite and thin film retained austenite), martensite and blocky retained austenite.

Numerical simulations were done using a von Mises J2 plasticity flow rule and also a phenomenological crystal plasticity material model. The representative volume element (RVE) was created using a realistic 2D geometry captured through Electron Backscatter Diffraction (EBSD). These simulations describe the strain distribution and deformation localization in this steel. To validate the simulation results, local strain maps were obtained experimentally via *in-situ* tensile testing using micro digital image correlation (μDIC) in scanning electron microscopy (SEM). The information gained from numerical and experimental data gave valuable insight regarding the microstructural features responsible for strain partitioning and damage initiation in this carbide free bainitic steel. The results of the modelling show that martensite, martensite/bainitic ferrite interfaces, interface orientation with respect to tensile direction, bainitic ferrite size and phase composition influence the strain partitioning in this carbide free bainitic steel.

† This chapter is based on an article submitted to a journal for publication.

4.1 Introduction

Pearlitic steels are commonly used in railway applications. Due to demands of future railway transport, there is a need for better materials that can endure the high contact stresses which over time lead to rolling contact fatigue [1–3] and wear [4,5] in rails. Bainitic steels have gained a lot of attention in rail industries due to their higher strength and toughness than the pearlitic counterparts [6,7]. The conventional bainitic microstructure contains a mixture of bainitic ferrite with fine cementite (carbide) laths (or particles) in between them. The presence of cementite laths can lead to void initiation or cleavage in the bainitic microstructure and is detrimental for the fatigue life of the steel [8]. The cementite precipitation in bainitic steels can be suppressed by the addition of Si during the alloy design [9,10]. The bainitic transformation in the presence of high Si (1.3-2.0 wt.%) results in a carbide free bainitic microstructure which contains bainitic ferrite, retained austenite and martensite. The retained austenite usually exists in two morphologies: *(i)* thin film retained austenite (TFRA) between bainitic ferrite *(ii)* blocky retained austenite (BRA), which is distributed between bainitic regions [8]. The TFRA acts against crack propagation [8] and the aggregate it produces together with fine bainitic ferrite results in high strength, toughness and hardness [11–13]. These steels also offer better rolling contact fatigue (RCF) characteristics compared to conventional pearlitic steels [14,15]. Therefore, carbide free bainitic steels could be a good candidate for railway applications.

Heterogeneous deformation in metals can initiate damage. Proper modelling of this heterogeneous deformation would result in prediction of locations where cracks form. The knowledge about these damage initiation sites would help to design stronger and more damage resistant metals. Many researchers have studied such heterogeneous deformation and damage in metals [16–26].

The crystal plasticity (CP) has been successfully used to describe the anisotropic deformation modes of metallic materials (such as dislocation slip and deformation twining). This methods can effectively describe the micromechanical behavior of polycrystalline materials and has been used by many researchers to simulate the damage accumulation and fracture [27–35].

The mechanical response and damage behavior in multi-phase complex steels are governed by microscopic strain and stress partitioning among the microstructural constituents. Such complex microstruture with different phases would produce highly non-uniform partitioning of stresses and strains in the microstructure. The stress/strain partitioning can lead to severe deformation localization and eventually can initiate damage during the application of mechanical loading [36,37]. However, the complexity of the microstructure makes it difficult to capture such strain partitioning and damage response. Many numerical and experimental studies have been performed on dual phase steels and some of these studies have combined both

numerical and experimental methods in order to study the damage mechanism [37–50]. But there exist only few studies on the damage and strain partitioning phenomena in the complex bainitic microstructures [35,51] such as Continuously Cooled Carbide Free Bainitic Steels (CC-CFBS) (industrially known as B360). Therefore, a detailed investigation is needed to study the local deformation and microscopic damage mechanisms in these steels, in relation to their microstructural constituents.

Numerical models have been established to study the material micromechanical behavior using a simplified geometry based on the Voronoi algorithm [43,52]. Recently, development of computational tools has enabled to investigate the material response by considering its realistic microstructure [33,35,40,41,44,51,53–56]. Many researchers [36,57–61] have performed *in-situ* experiments with micro Digital Image Correlation (μDIC) to measure local strain maps in steels. Such experiments are useful for the validation of numerical models. However, few studies have been performed using a combined numerical and experimental approach on the same geometry so that the local strain maps obtained from simulations could be validated using *in-situ* experiment [62–64].

In this research, we use this combined approach where numerical simulations are validated using the *in-situ* experimental results, on the microstructure of a CC-CFBS. Both the simulations and the experiment were performed on the same microstructure. Using this approach, the strain partitioning and damage initiation behavior of this CC-CFBS has been investigated. Numerical simulations using two different methods including: *(i)* a von Mises J2 plasticity model within the framework of continuum mechanics (via Abaqus) and *(ii)* a phenomenological crystal plasticity finite element approach (via DAMASK, the Düsseldorf Advanced Material Simulation Kit, [65]) using a fast Fourier solver [66], have been performed. The representative volume element (RVE) for the numerical models has been created using 2-dimensional microstructure of CC-CFBS, obtained through Electron Backscatter Diffraction (EBSD). The validation was done via *in-situ* tensile experiment with μDIC in Scanning Electron Microscope (SEM) in combination with EBSD.

The combined numerical and experimental investigation on the damage mechanisms in CC-CFBS provides valuable insight into damage initiating microstructural factors. This would help to optimize the microstructure by removing/reducing these factors, which would result in steels with better mechanical performance such as high strength and toughness.

4.2 Methodology

4.2.1 Material

The chemical composition of continuously cooled carbide free bainitic steel (B360) is verified by a combined use of Optical Emission Spectrometry (OES) and X-ray Fluorescence Spectrometry (XRF) techniques and is presented in Table 4.1. The final microstructure is produced by continuous cooling in the air from fully austenitic temperature range. Low carbon content is selected in the current alloy in order to have good weldability and fast bainitic transformation kinetics [67]. By using silicon, carbide formation is suppressed and carbide-free bainitic microstructure is obtained [9,10].

Table 4.1. Chemical composition of B360 (in wt.%).

Steel Grade	C	Cr	Mn	Si	V	Mo
B360	0.27	0.51	1.55	1.36	0.03	0.15

4.2.1.1 EBSD analysis

The EBSD characterization was performed by an FEI Quanta-450 SEM with a field emission gun (FEG). To collect EBSD data, a Hikari-Pro EBSD detector together with an EDAX-TSL OIM Data Collection software was utilized. Accelerating voltage was 15 kV and a step size of 50 nm was employed in a hexagonal scan grid mode for all scans. To analyze the EBSD data a TSL OIM data analysis v. 7.0 software was used. The points with a confidence index less than 0.1 were excluded from quantification.

The EBSD analysis of this steel is presented in Figure 4.1. Figure 4.1(a) shows the phase map of B360. Bainite, which is a lamellar structure of bainitic ferrite [68], is shown in red and (blocky) retained austenite in green. However, the EBSD phase map cannot distinguish between bainite and martensite and they are both represented in red. It is possible to separate martensite from bainite using image quality (IQ) maps. Martensitic islands have lower IQ than the bainitic ferrite, which is due to high dislocation density that reduces the quality of the diffraction pattern [69,70]. The lower IQ values mean that martensite in the microstructure would appear darker in IQ maps. Figure 4.1(b) shows the phase map together with the IQ map while Figure 4.1(c) shows the martensite distribution, represented in black. The EBSD analysis shows that B360 steel consists of about 64% bainite, about 22% M, and around 14% retained austenite.

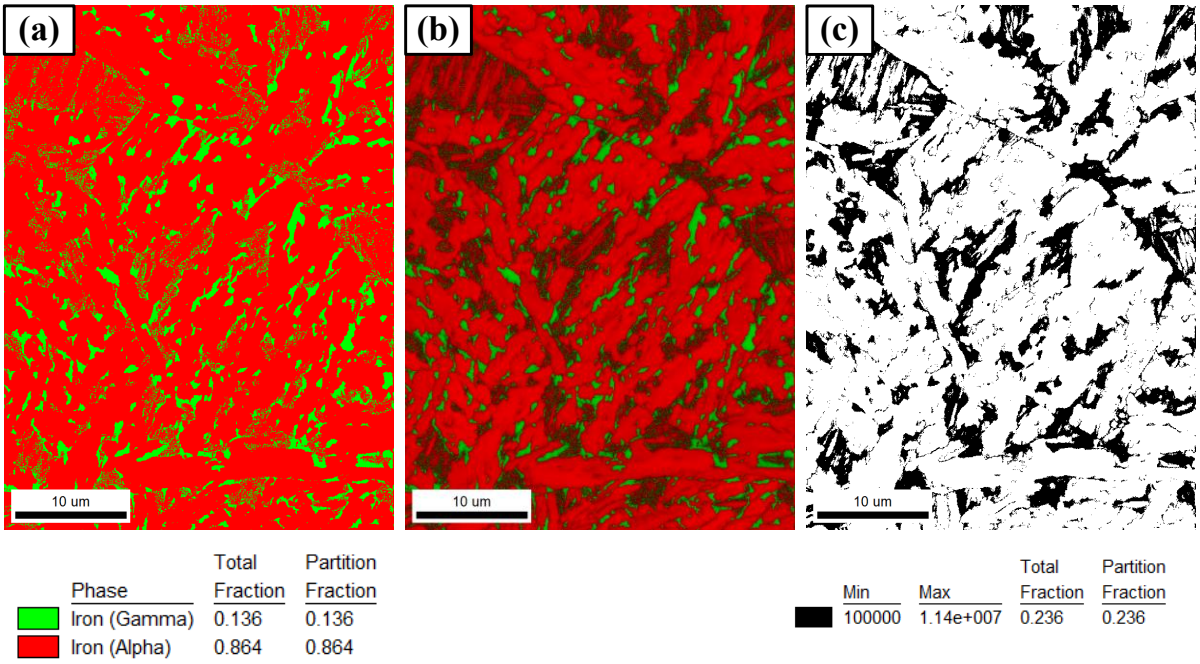

Figure 4.1. EBSD map of B360, (a) phase distribution map, (b) IQ and phase fraction map, (c) the IQ map, showing martensite distribution (as dark areas).

4.2.1.2 SEM analysis

Analyses of the SEM images were conducted in order to measure some microstructural characteristics that will be discussed at section 0. The SEM was performed on a JEOL JSM-IT100 microscope with a tungsten filament. The accelerating voltage was 10 kV and working distance was 6.6 mm.

4.2.2 Numerical models

In order to simulate the strain partitioning and damage behavior of the B360 under tensile loading, a von Mises J2 plasticity finite element model (VPFEM) and a phenomenological crystal plasticity model using a fast Fourier transform solver (CPFFT) [65,66] were applied. For the former, Abaqus software and for the latter the framework of DAMASK are used. DAMASK provides various constitutive models, of which phenomenological power law (a dislocation based model) [65] is applied in this research. The flow curves of individual phases are calculated by using a dislocation-density-based strain hardening model (section 0) and later used to calibrate these material models.

4.2.2.1 Representative volume element

Representative volume element (RVE) approach [71] was employed to create a representative geometry from the actual microstructure of the B360 steel. The RVE

model represents phase distribution and morphology, shape, size and spatial distribution of the different phases. Using the EBSD data a 2D RVE was built from the actual microstructure of B360 (Figure 4.1).

Based on another study on the exact same grade, we know that most of retained austenite transforms into martensite during *in-situ* tensile testing in a deformation induced martensitic transformation mechanism [72]. This study shows that large BRA islands (with grain size > 0.25 μm) are less stable compared to finer or nano-crystalline retained austenite islands during mechanical deformation. Based on this information and for simplicity, it is assumed that all of BRA tranforms into martensite at the beginning of straining. So, the microstructure will be consisting of a bainite costituent and a martensite phase. In the bainite, which is an aggregate of TFRA and bainitic ferrite, the TFRA cannot be indexed in the EBSD due to the limit of spatial resolution and hence the aggregate of bainitic ferrite and TFRA is considered as one homogeneous microstructural constituent in the numerical model, named as bainite. The resulting RVE is shown in Figure 4.2(a). The EBSD data is then edited using MATLAB based codes [73] and cleaned from the pixels which are non-indexed, have low confidence index (CI) and belong to unreasonably small grains. These pixels are filled with phase ID, grain ID and orientations equal to those of the grain that surrounds these removed pixels. In order to prepare the input for the VPFEM, this edited EBSD data set is meshed and prepared for Abaqus as shown in Figure 4.2(b).

However for DAMASK there is no need of meshing and the input data (geometry, material texture and phase distribution) can be extracted from the same edited EBSD data set, using the tools already implemented in DAMASK.

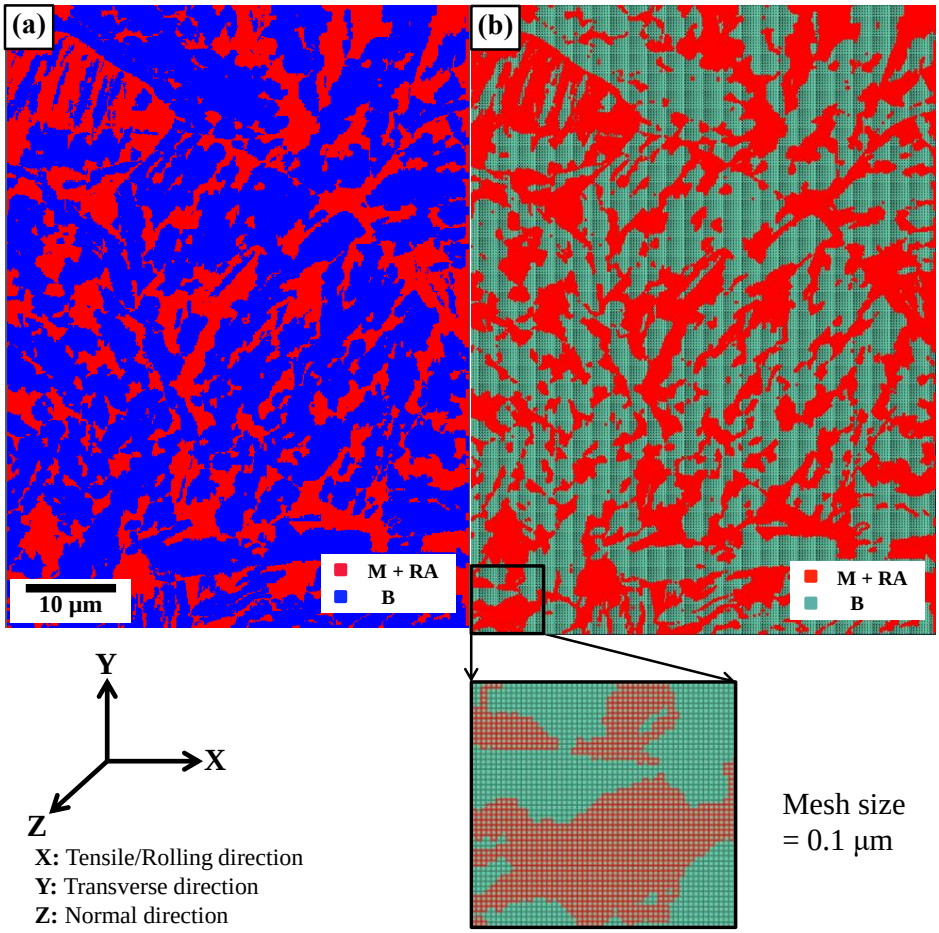

Figure 4.2. Selection of the RVE from the EBSD and creating the geometry input for models, (a) The RVE input into spectral solver of DAMASK, (b) The RVE input into Abaqus after meshing.

4.2.2.2 Mechanical properties of each phase

There have been several studies to measure the mechanical properties of each phase in steels [40,41,74]. In this work, all phases were assumed to be homogeneous. The flow curve of the individual constituents of martensite and bainite is estimated using a dislocation-based strain hardening model [74] which originates from classical dislocation theory [75–77]. The nano-hardness test has shown that this model has a good estimation of the stress-strain relation of the single phases [74]. The elastic properties of each phase are assumed to be the same as B360 steel which was calculated in [68] as E=202.6 MPa and υ=0.3, with E the Young's modulus and υ the poisson ratio.

The stress-strain relation is presented as follows [74]:

$$\sigma = \sigma_0 + \Delta\sigma + \alpha\, M\, \mu \sqrt{b} \sqrt{\frac{1-\exp(-M\, k\, \varepsilon)}{k\, L}} \tag{4.1}$$

where σ is flow stress (von Mises). The first term (σ_0) takes care of the dislocation strengthening effect as well as work softening due to recovery. Second term ($\Delta\sigma$) is the

additional strengthening due to the precipitation or the carbon in solution and the last term is the strain-dependent part where ε is the true plastic strain (equivalent plastic strain).

The value of σ_0 which is called the Peierls stress is calculated using the effects of alloying elements in the solid solution.

$$\sigma_0 = 77 + 80 \times (\%\mathrm{Mn}) + 750 \times (\%\mathrm{P}) + 60 \times (\%\mathrm{Si}) + 80 \times (\%\mathrm{Cu}) + 45 \times (\%\ \mathrm{Ni}) + 60 \times (\%\mathrm{Cr}) + 11 \times (\%\mathrm{Mo}) + 5000 \times (\%N_{ss}) \quad (4.2)$$

The fraction of alloying elements in bainite and martensite is taken the same as the bainitic B360 steel which is presented in Table 4.1.

However, the carbon content is different in the two constituents. The carbon content of bainitic ferrite is taken to be 0.1% [78,79] and in martensite 0.58%. For martensite and ferrite Δσ is calculated as follows [80]:

$$\Delta\sigma_m = 3065\ (\%C_{ss}^m) - 161 \quad (4.3)$$

$$\Delta\sigma_f = 5000\ (\%C_{ss}^f) \quad (4.4)$$

where C_{ss}^m is carbon content (wt%) in martensite and C_{ss}^f is carbon content (wt%) in ferrite.

For bainite, the effect of dislocation strengthening is strong and more influential than the solid solution carbon strengthening effect [81]. Δσ for bainite is dependent on prior austenite grain size (PAGS) and transformation temperature [80,82]. Low bainitic transformation temperature would result in high density of transformation dislocations and also higher Δσ value. PAGS indirectly influences the Δσ value since it can influence bainitic transformation temperature and kinetics [80–82]. In this work, the same approach as in [83] and the same rule of mixtures are used to calculate the value of $\Delta\sigma_b$ for bainite. The hardness of B360 steel, which was measured as 344 HV0.1 is equal to the hardness of DP1000 dual phase steel, which contains 0.15% carbon [84] with 48% ferrite and 52% martensite volume fraction. So $\Delta\sigma_b$ can be measured as follows:

$$\Delta\sigma_\mathrm{b} = \Delta\sigma_\mathrm{f} \times \mathrm{V_f} + \Delta\sigma_\mathrm{m} \times \mathrm{V_m} \quad (4.5)$$

where $\mathrm{V_f}$ and $\mathrm{V_m}$ are the volume fraction of ferrite and martensite (in DP1000 steel), respectively. Using this approach the value of $\Delta\sigma_b$ was calculated to be 365 MPa.

The last term in eq. (4.1) considers the strain dependency. The constant α is equal to 0.33, M is Taylor factor (M = 2.75) [51], μ is the value of shear modulus (μ = 77.9 GPa) and b is the length of Burger vector ($b = 2.5\times10^{-10}$ m). The dislocation mean free path L for ferrite, is considered equal to the average grain diameter (d_α), for martensite, it is 3.8×10^{-8} m [74,85] and for bainite is assumed to be the average distance between low

angle grain boundaries [83]. The average bainitic lath width was calculated as 0.55±0.09 μm by using the SEM images captured from various bainitic laths, for which two of these cases are shown in Figure 4.3. So the *L* for bainitic ferrite is measured to be 0.55 μm.

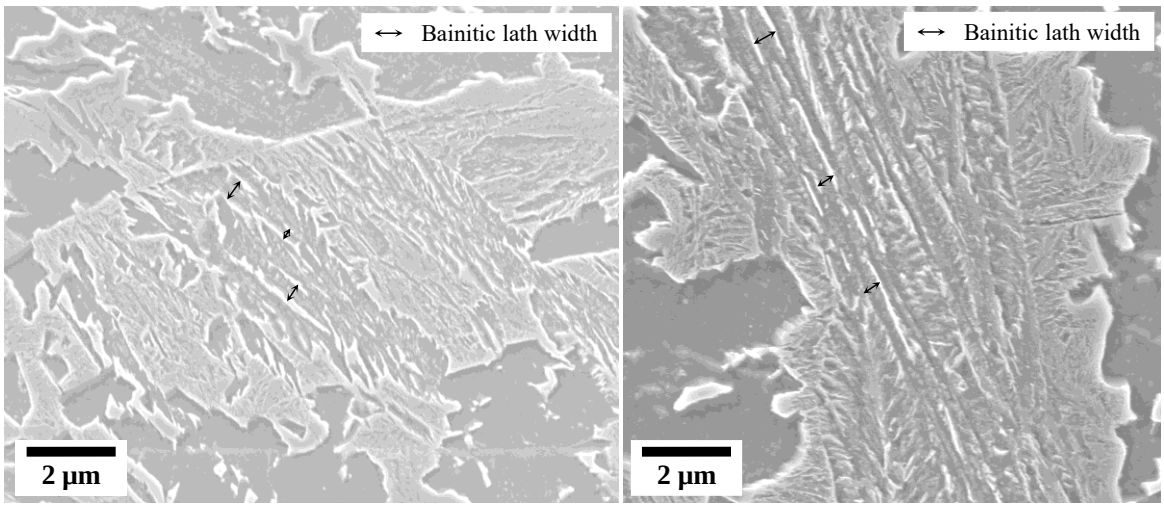

Figure 4.3. SEM images from different bainitic laths.

The recovery rate k is $10^{-5}/d_{\alpha}$ for ferrite, and 41 for martensite [82,83,86]. For bainite, k is considered to be $10^{-5}/d_{\gamma}$, where d_{γ} is the PAGS [83,87].

Figure 4.4(a) represents the EBSD phase map (red color showing Iron-Alpha and green color showing Iron-Gamma phase) overlapped with IQ for the original RVE. Figure 4.4(b) shows the inverse pole figure (IPF) map overlapped with IQ map of the considered RVE. Since the size of this RVE was small compared to the prior austenite grains (PAGs) (as shown in Figure 4.4(b)) and not statistically suitable to measure the PAGS, another larger region of B360 was examined. The phase map overlapped with IQ map of this second region is shown in Figure 4.4(c) and its IPF map is shown in Figure 4.4(d). All IPF maps are plotted in the normal direction. In order to calculate the PAGS of the second region of B360, the PAGs were reconstructed from the EBSD maps, using ARPGE 2.4 software [88]. We considered Nishiyama-Wassermann (N-W) orientation relationships for this reconstruction. The PAGs were further plotted using TSL OIM Analysis v. 7.0 software and shown in Figure 4.4(e). The average PAGS was calculated (using the second region data) as 26±9 μm. From this measurement the k was calculated for bainite.

Based on these measurements and calculations, the stress-strain curves for bainite and martensite are plotted in Figure 4.5.

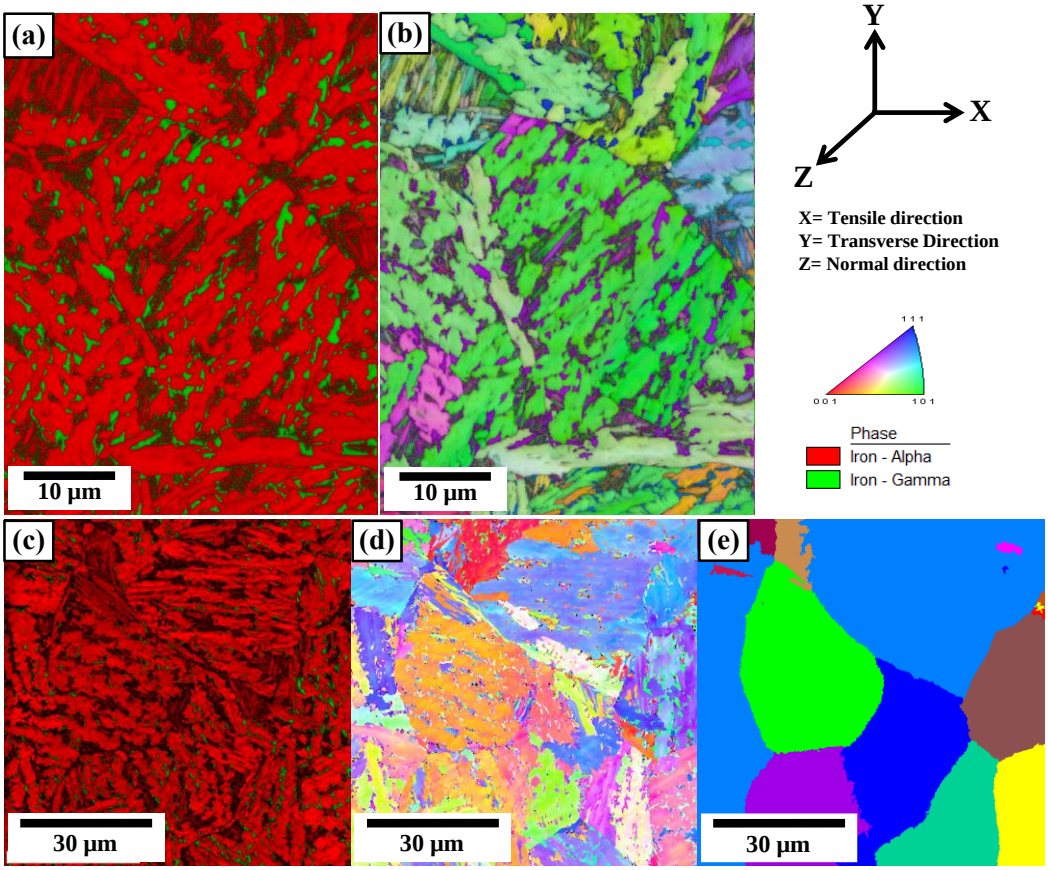

Figure 4.4. EBSD maps of two different regions of B360, (a) The phase map overlapped with IQ map of the considered RVE created from first region, (b) IPF map overlapped with IQ map of the considered RVE, (c) The phase map overlapped with IQ map of second region of B360, (d) IPF map of second region of B360 (IPFs are plotted in the normal direction), (e) Grain map of the reconstructed PAGs.

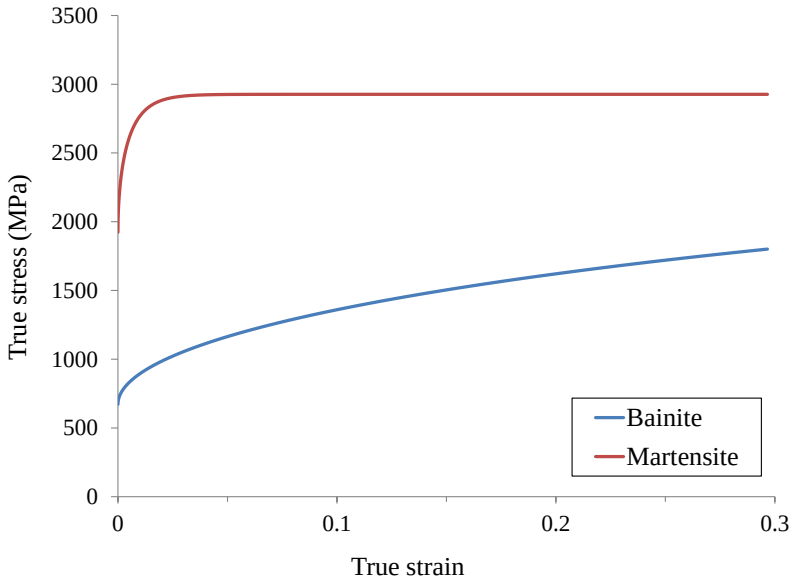

Figure 4.5. Stress strain curves for bainite and martensite in B360.

4.2.2.3 von Mises J2 plasticity material model

In this model, for both phases von Mises J2 plasticity material model with an isotropic hardening law is used. The flow behavior shown in Figure 4.5 is used and yield stress is given as a function of plastic strain. The RVE mentioned in section 4.2.2.1 is used with a mesh size of 0.1 μm. Periodic boundary conditions (PBC) are applied using a python based code to impose the repetitive deformation on this RVE. In order to do so the meshing should be in a way that nodes on opposite sides of the RVE are equal in number and space.

PBCs [89] imply that the macroscopic geometry of the bigger model can be constructed by spatially repeating the RVE. Using such boundary conditions also results in periodic deformation of the micromechanical model. These boundary conditions are defined as follows [90]:

$$\vec{x}_R = \vec{x}_L + \vec{x}_2 - \vec{x}_1, \tag{4.6}$$

$$\vec{x}_T = \vec{x}_B + \vec{x}_4 - \vec{x}_1, \tag{4.7}$$

where $\vec{x}_R, \vec{x}_L, \vec{x}_B$ and $\vec{x}_T$ are a position vector on the right, left, bottom and top of the boundary of RVE. And $\vec{x}_i, i = 1, 2, 4$, are the position vectors of the corner points 1, 2 and 4 (in deformed state).

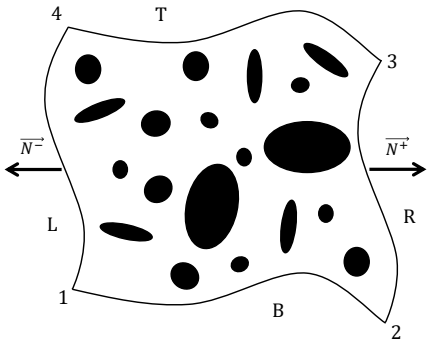

Figure 4.6. The representation of PBCs.

Other proper boundary conditions were also imposed to remove rigid body motion and apply uniaxial tensile displacement. Then simulation was performed and the strain localization results were postprocessed which will be discussed in section 4.3.

4.2.2.4 Phenomenological crystal plasticity material model

The geometry definition for the CPFFT model is done using the EBSD data of the microstructure. This geometry as a periodic volume element is defined by the size and the grid in each direction. The size is chosen as 35×47.3×0.1 μms with 350×473×1 grid points to solve the equations. The information regarding grains belonging to different

constituents which have different constitutive behaviors and also exist in various crystallographic orientations was also obtained from EBSD map in order to create the material model input. This geometry and material model information were then introduced to DAMASK. The tensile deformation was applied in x-direction (Figure 4.2) with the strain rate of 6×10^{-4} s^{-1} up to total strain of 0.09. The constitutive behavior of material is discussed in more detail in the following.

A phonemenological crystal plasticity material model together with a spectral solver has been used to model the tensile deformation behavior and strain partitioning in the carbide free bainitic B360 steel. Crystal plasticity was implemented within DAMASK [65]. Among the material models [91–94] a viscoplastic phenomenological model [94] was chosen. The most important relations of this constitutive model are presented.

The deformation gradient $\boldsymbol{F}$ is decomposed multiplicatively to elastic and plastic parts:

$$\boldsymbol{F} = \boldsymbol{F}_e\boldsymbol{F}_p \tag{4.8}$$

where $\boldsymbol{F}_e$ describes the elastic deformation gradient which considers the elastic distortion of the lattice and $\boldsymbol{F}_p$ represents plastic deformation gradient which considers the cumulative effect of dislocation motion on the active slip systems in the crystal.

The plastic deformation evolves as:

$$\dot{\boldsymbol{F}}_p = \boldsymbol{L}_p\boldsymbol{F}_p \tag{4.9}$$

The plastic velocity gradient $\boldsymbol{L}_p$ is presented as a sum of all shear slips on slip systems:

$$\boldsymbol{L}_p = \sum_{\alpha=1}^{n}\dot{\gamma}^{\alpha}(\boldsymbol{m}^{\alpha} \otimes \boldsymbol{n}^{\alpha}) \tag{4.10}$$

where $\dot{\gamma}$ is the reference shear strain rate and α is the slip system index, vectors $\boldsymbol{m}^{\alpha}$ and $\boldsymbol{n}^{\alpha}$ are unit vectors which represent slip direction and normal to the slip plane respectively.

Phenomenological power law uses the critical shear stress S^{α} of the slip systems as state variable for each slip system α. The evolution of material state on slip system α is formulated as a function of total shear γ and shear rate $\dot{\gamma}^{\alpha}$. Given a set of current slip resistances, shear on each system evolves at a rate:

$$\dot{\gamma}^{\alpha} = \dot{\gamma}_0 \mathrm{sgn}\,(\tau^{\alpha})\left(\frac{|\tau^{\alpha}|}{R^{\alpha}}\right)^{m} \tag{4.11}$$

where $\dot{\gamma}_0$ is reference shear rate, m is the strain rate exponent value, τ^{α} is resolved shear stress and R^{α} is current slip resistance of slip system α.

The resolved shear stress on slip system α is defined by:

$$\tau^{\alpha} = \boldsymbol{F}_e^{T}\boldsymbol{F}_e\boldsymbol{S}.(\boldsymbol{m}^{\alpha} \otimes \boldsymbol{n}^{\alpha}) \tag{4.12}$$

where $\boldsymbol{S}$ is considered as second Piola-Kirchhoff stress. As for metallic materials the elastic deformation is small, above equation is usually approximated as:

$$\tau^{\alpha} = \boldsymbol{S}.(\boldsymbol{m}^{\alpha} \otimes \boldsymbol{n}^{\alpha}) \tag{4.13}$$

In crystal plasticity theories, the slip system resistance parameter R^{α} is given by:

$$\dot{R}^{\alpha} = \sum_{\alpha=1}^{n} \dot{\gamma}^{\alpha} h_0 \left|1 - \frac{R^{\alpha}}{R_S^{\alpha}}\right|^{a} \operatorname{sgn}\left(1 - \frac{R^{\alpha}}{R_S^{\alpha}}\right) h_{\alpha\beta} \tag{4.14}$$

where R_S^{α} is the saturation slip resistance, h_0 is the initial hardening rate, $h_{\alpha\beta}$ is the interaction parameter which describes the rate of increase of deformation resistance on slip system α due to shearing on slip system β and a is a fitting parameter. In this formula h_0, a, R_S^{α} are slip hardening parameters and are assumed to be identical for all slip systems.

To calibrate the material model parameters, the stress-strain curves for bainite and martensite were used (Figure 4.5). Initial and saturation flow stress and parameters controlling the hardening behavior were estimated using reverse engineering, i.e. the effect of each single model parameter was studied in the simulation results to see which set of parameters results in the best fit with the calculated stress-strain response.

Using Voronoi tessellation algorithm [95] a randomized three dimensional microstructure was generated in order to approximate the distribution of grain size and shape. Periodic boundary conditions were imposed on this RVE. In order to find the suitable number of grains for this RVE, the stress-strain response of the simulations with different number of grains, were compared. Before any plastic strain develops, all the different analyses have the same response because of the elastic behavior of the grains and therefore there is no influence of the crystal orientations i.e. the model can be considered homogeneous. It was noted that the difference between the plastic responses is decreased when the number of grains is increased. In a model with more grains, the heterogeneity in the model tends to become less pronounced, which results in a more representative model for the macroscopic material. After the number of grains reaches a certain level differences in texture do not cause much difference in the stress-strain response. The same load was applied on the RVE as in the macroscopic uniaxial tensile tests. Resolution was chosen to be 32×32×32 since the obtained results had no significant difference with the results from using an RVE with 64×64×64 resolution. For solving the equations an FFT solver was used [66].

The elastic properties for martensite are considered the same as in [36] and for bainite these were considered the same as for the B360 steel during the macroscopic tensile testing [68]. The calibrated material parameters are presented in Table 4.2.

Table 4.2. The material parameters in phenomenological power law model for bainite and martensite.

Material parameters	Description	Bainite	Martensite	
C_{11}	Elastic constant	282×10^3	417.4×10^3	MPa
C_{12}	Elastic constant	121×10^3	242.4×10^3	MPa
C_{44}	Elastic constant	80×10^3	211.1×10^3	MPa
$\dot{\gamma}_0$	Reference shear strain rate	0.001	0.001	ms^{-1}
R_0^α	Initial slip resistance	260	710	MPa
R_s^α	Saturation slip resistance	840	1140	MPa
h_0	Initial hardening rate	9×10^3	230×10^3	MPa
$h_{\alpha\beta}$	Interaction parameter	1	1	
m	Strain rate exponent	20	20	
a	Hardening exponent	3.2	2.05	

4.2.3 In-situ tensile experiment

To analyze the strain partitioning and damage initiation in low carbon carbide free bainitic B360 steel, *in-situ* μDIC tensile experiment was performed in SEM. This experiment was combined with EBSD measurements prior to the *in-situ* testing [72]. Specimens with dimensions of 1 mm × 0.5 mm × 0.5 mm were deformed with a strain rate of 6×10^{-4} s^{-1} up to 9% global strain [72]. Electrical Discharge Machining (EDM) was used for sample preparation. Surfaces of the specimens were polished using colloidal silica (with 50-100 nm particle size).

In order to find the regions of interest (ROI) on the specimen surfaces a JEOL JSM 6500F scanning electron microscope was used. For the EBSD, accelerating voltage of 15 kV with a working distance of 18 mm and step size of 40 nm in a hexagonal scan grid were used. To locate the ROI during the *in-situ* testing, it was marked using Focused Ion Beam (FIB) milling in a Helios NanoLab 600i microscope. In order to perform local strain measurements during the tensile straining a monolayer of SiO2 particles (50-100 nm) was dispersed on the sample surface [72]. A Kammrath & Weiss stage inside the Zeiss Crossbeam XB 1540 microscope was used for *in-situ* tensile experiment. The deformation was applied on the specimens at a cross head speed of 3 μm/sec. After every deformation step of 1 μm, high resolution images of the ROI were taken using in-lens secondary electron (SE) detector. These images were then used for measurement of the von Mises equivalent micro-strain, using the Aramis software.

4.3 Numerical simulation results

4.3.1 von Mises J2 plasticity finite element model (VPFEM)

The RVE as discussed in section 4.2.2.1 and the material properties which were calculated in section 4.2.2.2 were used together with a von Mises J2 plastic material model from Abaqus. The periodic boundary conditions (as discussed in section 4.2.2.3) were assigned to the RVE together with a tensile deformation applied in x-direction (Table 4.2) with strain rate of 6×10^{-4} s^{-1} up to total strain of 0.09. Figure 4.7 shows the numerical simulation results of VPFEM performed in Abaqus. Figure 4.7(a) illustrates the RVE used for this model. The regions which include bainite (B), martensite (M) and an island which contains a mixture of lath bainitic ferrite (LBF) and martensite (M) which is located in the upper left corner of this image, are shown.

The von Mises strain distributions at different levels of global strain at 2.7%, 4.7% and 9% are shown at Figure 4.7(b)- Figure 4.7(d). As can be observed, the von Mises strain is partitioned between different constituents and as a result, areas of strain concentration are created in the microstructure during tensile deformation. The analysis of the data shown in Figure 4.7(d) while considering the RVE at Figure 4.7(a), shows that these strain concentrations mostly occur in channels of bainite between martensitic islands. The high strain in the bainitic areas locally deforms the bainite while martensite does not accumulate much strain and local deformation.

Strain partitioning in these different regions vs the global strain is shown in Figure 4.7(e). The von Mises local strain build up and partitioning in different constituents occurs while increasing the global strain. In order to measure these local strains, the average von Mises strain was measured in ten different elements from each constituent. The bainite (or bainitic ferrite) takes higher strain than the martensite. The bainite which is located in narrow channels between martensitic islands, takes much larger strains than bainite which is away from these channels and martensite islands. Therefore, the bainitic channels which are close to the martensitic regions face high strain localization. The narrower these channels are, the higher the strain localization will be. In Figure 4.7(e), narrow bainite channels were considered to be the ones narrower than 5 μm while bainite distant from martensite, refers to channels wider than 5 μm. Using VPFEM, the average von Mises local strain was calculated to be 32.9 ± 1.1% in narrow channels (at 9.0% global strain) and 17.2 ± 0.8% in bainite channels wider than 5 μm (also shown in Table 4.3).

From the simulation, it can be seen that the local strains are concentrated along 45° angle to the tensile axis, which is aligned with the maximum resolved shear stress direction. Experimentally, we observed that the interfaces (of two adjacent bainitic ferrite grains) which are aligned in the direction of maximum resolved shear stress, show high strain accumulation compared to interfaces aligned in other directions. Therefore, these interfaces can be potential sites for damage initiation [72].

The average strain accumulation in the islands with mixture of marteniste and LBF is lower than the average strain in the bainite regions while it is higher than the average strain accumulated in martensite. This is due to higher dislocation density and carbon concentration in LBF compared to coarse bainitic ferrite (in the bainite) [81]. In addition, this LBF is adjacent to martensite which gives this mixture more strength against straining.

The complex morphology of the carbide free bainitic steel makes it difficult to anticipate these strain concentration areas before loading. VPFEM gives an estimate of the strain concentration in the B360 microstructure. The maximum von Mises strain was measured to be 45% at 9.0% global strain (which happened in the upper right corner area in Figure 4.7(d)). As a conclusion, the main reason for high strain localization in the microstructure of this carbide free bainitic steel is that martensite accommodate lower von Mises local strain compared to bainite. This causes high strain accumulation in narrow channels of bainite in between these marteniste islands. In Figure 4.7(d), the red arrows indicate the high strain localization areas while the dark arrows represent the low strain areas occuring at martensitic islands. The areas indicated with red arrows could be candidates for nucleation of microcracks. As another damage initiating factor, martensite could also fracture in lower strains (compared to bainite), however as it was observed from numerical simulation, the critical value of fracture strain for martensite is not simply reached and the local strain rather partitions mostly into bainite.

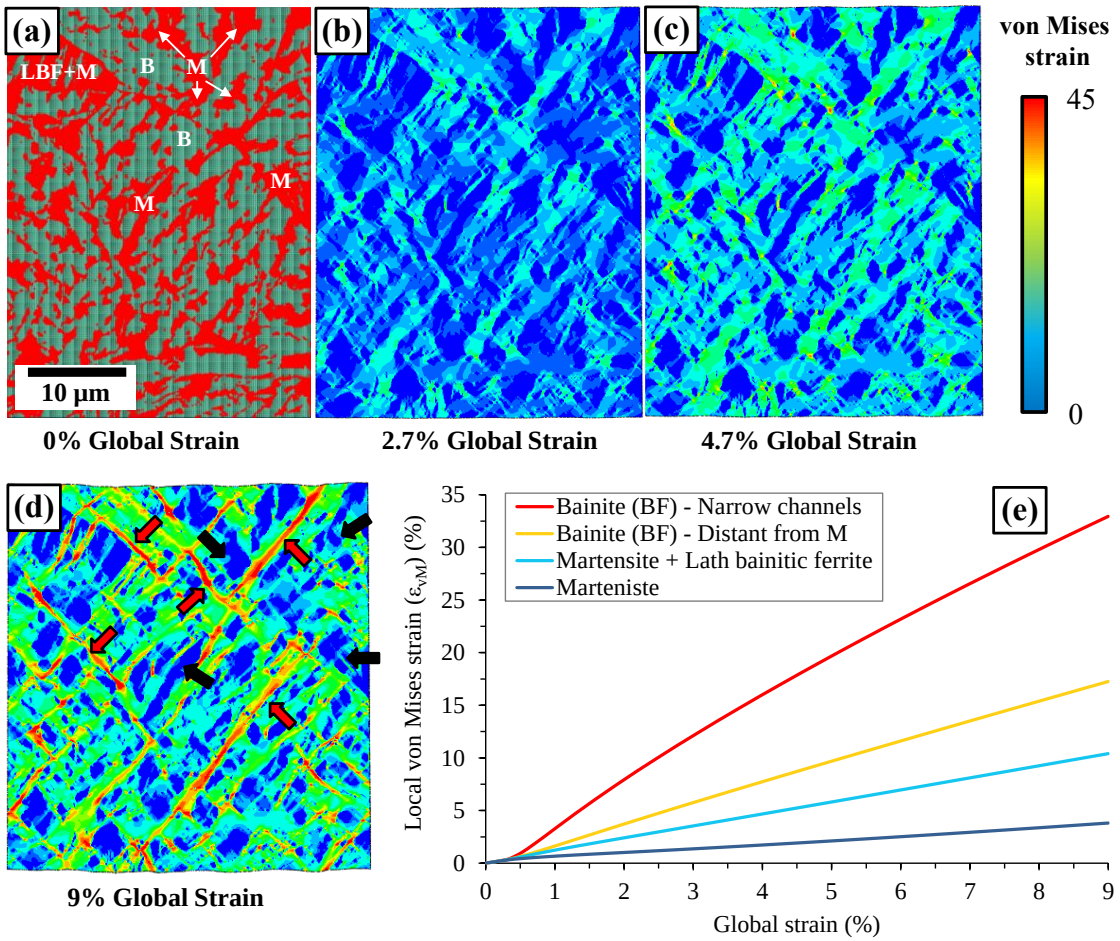

Figure 4.7. VPFEM numerical simulation results, (a) The RVE used for this model, (b) Local strain map at 2.7% global strain, (c) Local strain map at 4.7% global strain, (d) Local strain map at 9% global strain, (e) Strain partitioning among different constituents (and regions).

4.3.2 Phenomenological crystal plasticity fast fourier transform model (CPFFT)

DAMASK modeling platform was also used to analyse the strain partitioning in the same sample. The calibrated material model parameters were assigned to the phenomenological model (as discussed in section 4.2.2.4) and the same tensile deformation was applied.

Figure 4.8 shows the CPFFT simulation results. In Figure 4.8(a), the used RVE and the regions with different constituents are illustrated. Figure 4.8(b)- Figure 4.8(d) show the von Mises local strain build up during different stages of global strain at 2.7%, 4.7% and 9%. An observation similar to the one for VPFEM is also noted for CPFFT model i.e. the bainite endures much higher strain compared to martensite. This strain partitioning between different phases causes deformation localization in bainitic phase in between martensitic islands. In Figure 4.8(d), the high strain concentration areas (in bainitic phase) are illustrated with red arrows and low strain areas in martensitic phase are shown with black arrows. As shown in this figure the strain is mostly localized in

the bainite phase in between martensitic islands. These narrow bainitic channels in between martensite islands take more strain than the bainite in wider channels as shown in Figure 4.8(e). At 9% global strain, the channels narrower than 5 μm take 30.7 ± 0.9% average local von Mises strain while bainitic channels wider than 5 μm take 18.1 ± 0.6% local strain (as shown also in Table 4.3). Hence, these narrow regions of bainite situated between the martensitic islands face the highest strain localization and can be considered as potential microcracks nucleation sites. The same as for VPFEM, the strains are localized in direction of 45° to the tensile direction, which is the same direction for maximum resolved shear stress.

Another influential parameter for strain localization is the inclination of the interfaces of two adjacent bainitic ferrite (in the bainite). In-line with the experimental observation [72], the interfaces aligned in the direction of maximum resolved shear stresses (i.e. 45° to the tensile direction) show high strain localization and can be potential sites for damage initiation.

There is a good agreement between CPFFT simulation results with the ones from VPFEM although some deviations can be observed. Both simulation results indicate that the main reason for the start of strain localization in the carbide free bainitic B360 steel is the much lower local von Mises strain built up in martensite compared to bainite. The areas with high possibility of microcrack initiation are mostly the same in both simulations (comparing Figure 4.7(d) and Figure 4.8(d)) although some deviation are also observed. For the CPFFT, the maximum von Mises at 9% global strain was estimated to be 38% in comparison to the 45% resulted from VPFEM simulation results. The maximum von Mises strain estimated by CPFFT is closer to the value captured from in-situ tensile experiment (which will be discussed in the following section). The more accurate strain localization from the CPFFT can be due to the more accurate material model and also consideration of the texture as a material input in this model.

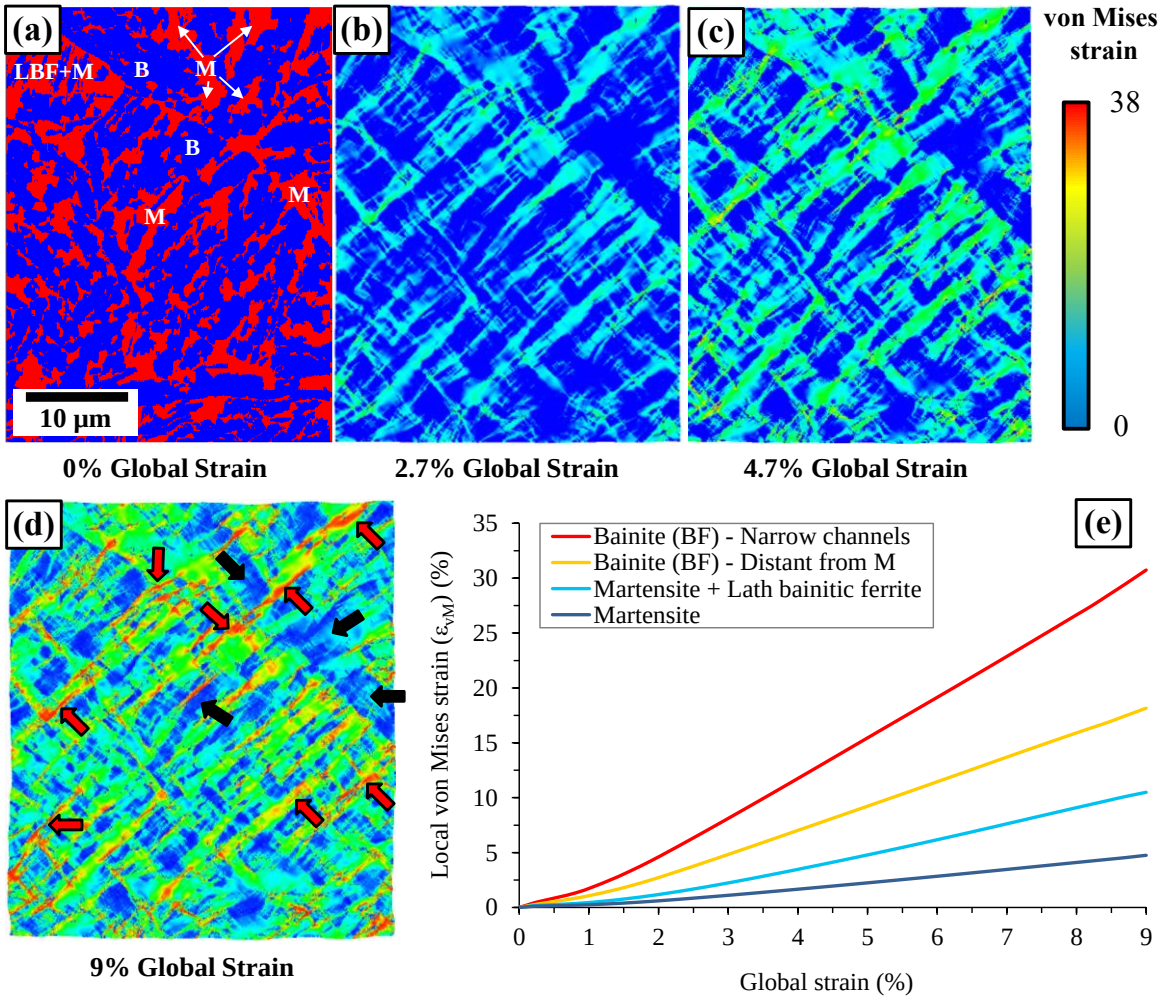

Figure 4.8. CPFFT numerical simulation results, (a) The used RVE for this model, (b) Local strain map at 2.7% global strain, (c) Local strain map at 4.7% global strain, (d) Local strain map at 9% global strain, (e) Strain partitioning among different constituents (and regions).

4.4 The *in-situ* tensile test results

Figure 4.9 shows the *in-situ* tensile test results performed on the B360 steel as described at section 4.2.3. Figure 4.9(a) shows the overlapped EBSD phase map and IQ map of B360 steel with red color assigned to bainitic phase (B), green color assigned to BRA and black representing the low IQ areas indicating the martensitic islands (M).

Figure 4.9(b)- Figure 4.9(d) show the von Mises strain maps during different steps of global strains at 2.7%, 4.7% and 9%. In order to understand the strain partitioning behavior, the average local von Mises strain vs global strain for different constituents, are presented in Figure 4.9(e). Martensite takes the lowest average von Mises strain. The local von Mises strain build up in the island with mixture of LBF and marteniste is larger than strains in the martensite due to presence of bainitic ferrtite laths but lower strain than BRA (as observed in Figure 4.9(e)). Much less strain is accumulated

in this island than the bainite. The higher dislocation density and carbon concentration in LBF compared to coarse bainitic ferrite (in the bainite) [81] together with the fact that this bainitic ferrite is mixed with stronger martensite result in lower strain build up in this constituent compared to bainite.

BRA also tends to take more strain than martensite but less strain than the LBF and martensite mixture (at upper left corner in Figure 4.9) and also the bainite. In the initial stages of global strain up to 2.3%, retained austenite takes the highest local strain among all other constituents. This can be due to the easy slip tendency in the face centered cubic crystal structure of retained austenite, which is followed by strain-induced transformation of austenite into martensite. As mentioned earlier in section 4.2.2.1 another study on the same steel grade shows that the austenite fraction suddenly decreases during the global strain of 0 to 3% and the large BRA islands (grain size > 0.25 μm) which are less stable, turn into martensite [72]. After 2.3% of global strain, bainite takes the highest local von Mises strain among all the constituents. The maximum strain accumulation in BRA at 9% global strain is approximately 11%, which is still much lower than the 29% of average von Mises strain accumulated in bainite. This can be due to the fact that after 2.3% of global strain, BRA gradually further transforms into martensite by a strain-induced phase transformation which causes this locations to take less strain compared to untransformed retained austenite.

The strain partitioning causes strain localization mainly between martensitic islands in the bainite channels as it is depicted in Figure 4.9(d). In this figure, the black arrows show the martensite islands (which take low strains) and the red arrows show the high strain concentration areas which are located in narrow bainite channels surrounded by martensitic areas. The orange arrows show the location of the crack in these channels which resulted from this excessive strain localization. This crack further continues and fractures the martensitic island in the middle of the microstructure. The test results show that the strains are higher when the bainitic ferrite channel is narrower. The average local strain was measured to be 30.4 ± 1.6% in bainitic ferrite channels narrower than 5 μm while this value was 20.5 ± 1.0% for channels which are wider than 5 μm. This confirms the good estimation from both simulations (as shown in Table 4.3).

As also observed for both simulations, the strain localization is maximum in the 45° angle to the tensile direction, which is aligned with the maximum resolved shear stress direction. The bainite-bainite interfaces which are oriented in the same direction (45° angle to the tensile direction) face the highest average von Mises strain and was measure to be 35% [72] in comparison to 45% using VPFEM and 38% using CPFFT.

There is general agreement between the simulation and experimental results. The microcrack observed at the *in-situ* tensile tests was among the possible crack locations predicted by both simulations. However, there are some deviations in the results which will be explained in more detail in the section 4.5.

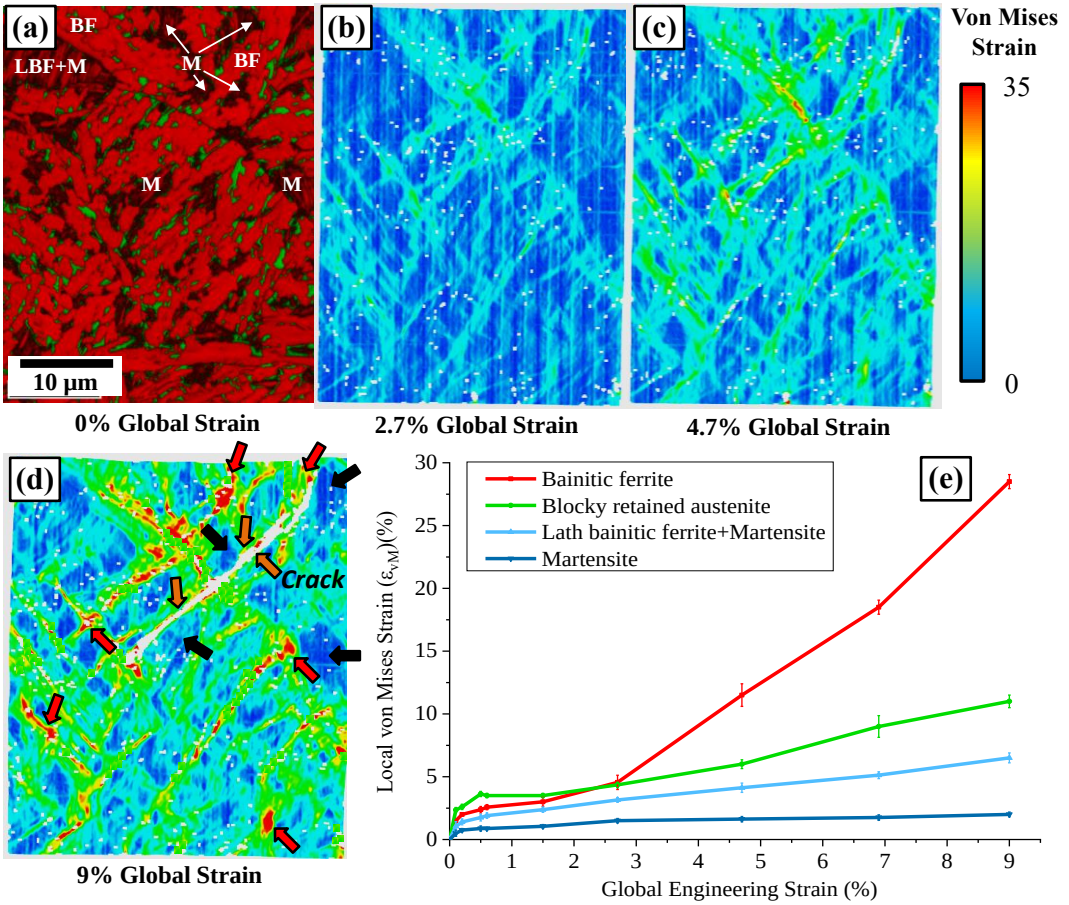

Figure 4.9. In-situ tensile test results of B360 [72], (a) The EBSD map of the used microstructure, (b) Local strain map at 2.7% global strain, (c) Local strain map at 4.7% global strain, (d) Local strain map at 9% global strain, (e) Strain partitioning among different constituents.

Table 4.3. The average local strain (%) built up at 9% global strain, in bainitic ferrite channels narrower or wider than 5 µm from simulations results and in-situ experiment results.

	Average local strain at bainitic channels < 5 µm	Average local strain at bainitic channels > 5 µm
VPFEM	32.9 ± 1.1%	17.2 ± 0.8%
CPFFT	30.7 ± 0.9%	18.1 ± 0.6%
In-situ experiment	30.4 ± 1.6%	20.5 ± 1.0%

The distribution of local von Mises strain obtained from both simulations and *in-situ* experiment at 9% global strain, are shown in Figure 4.10. This figure shows the fraction of counts (or area fraction) for certain von Mises strain. These ditributions follow near-logarithmic shapes. At Figure 4.10(a), the histogram resulted from Abaqus simulation

shows that the highest area fraction occurs at strains of 2-6%. After these strains, the value of area fraction reduces fast until strains around 12% where the rate of this reduction decreases. This is due to the fact that a large fraction of bainite which are away from martensitic islands endure strains in the range of 13-20% (Figure 4.7(e)). After local von Mises strains around 20% the area fraction value reduces rapidly in a logarithmic shape. According to DAMASK simulation results shown at Figure 4.10(b), the area fraction reaches its peak at strains in the range of 4-8% and then this area fraction reduces rapidly until local strains in the range of 12-17% which are the strains accumulated at bainitic area which are located away from martensitic islands (Figure 4.8(e)). In this strain range, the area fraction reduction rate decreases and after strains around 19% the area fraction value again reduces following a logarithmic pattern. Almost the same strain distribution is observed for *in-situ* simulation results as shown in Figure 4.10(c), however after the peak of area fraction is reached, the it reduces in a more constant logarithmic rate compared to the simulation results. The maximum area fraction occurs at strains in the range of 2-7%. The main difference in local strain distribution results between simulation results and *in-situ* experiment is how the area fraction reduces fast after the peak is reached and then slows down for the strain ranges of 12-17% in numerical simulation results while for experiment results this distribution is more smooth. This could come from the fact that the BRA (which endure average local strain of around 11% in global strain of 9%) are not considered in the microstructure models (for the reasons explained in section 4.2.2.1). Comparing the two modelling methods, it is observed that DAMASK simulation gives a better approximation of the local strain distribution from the experiments.

The mean and standard deviation (SD) of these distributions are calculated using a normal distribution (shown at Table 4.4 and Figure 4.10(d)). The DAMASK simulation results show estimation of the local von Mises strain distribution closer to the experiment results (in comparison to the Abaqus simulation results).

Table 4.4. The mean and standard deviation (SD) of these distributions.

	Mean (%)	SD (%)
ABAQUS (a)	10.32	7.2
DAMASK (b)	9.37	6.1
Experiment (c)	9.17	6.8

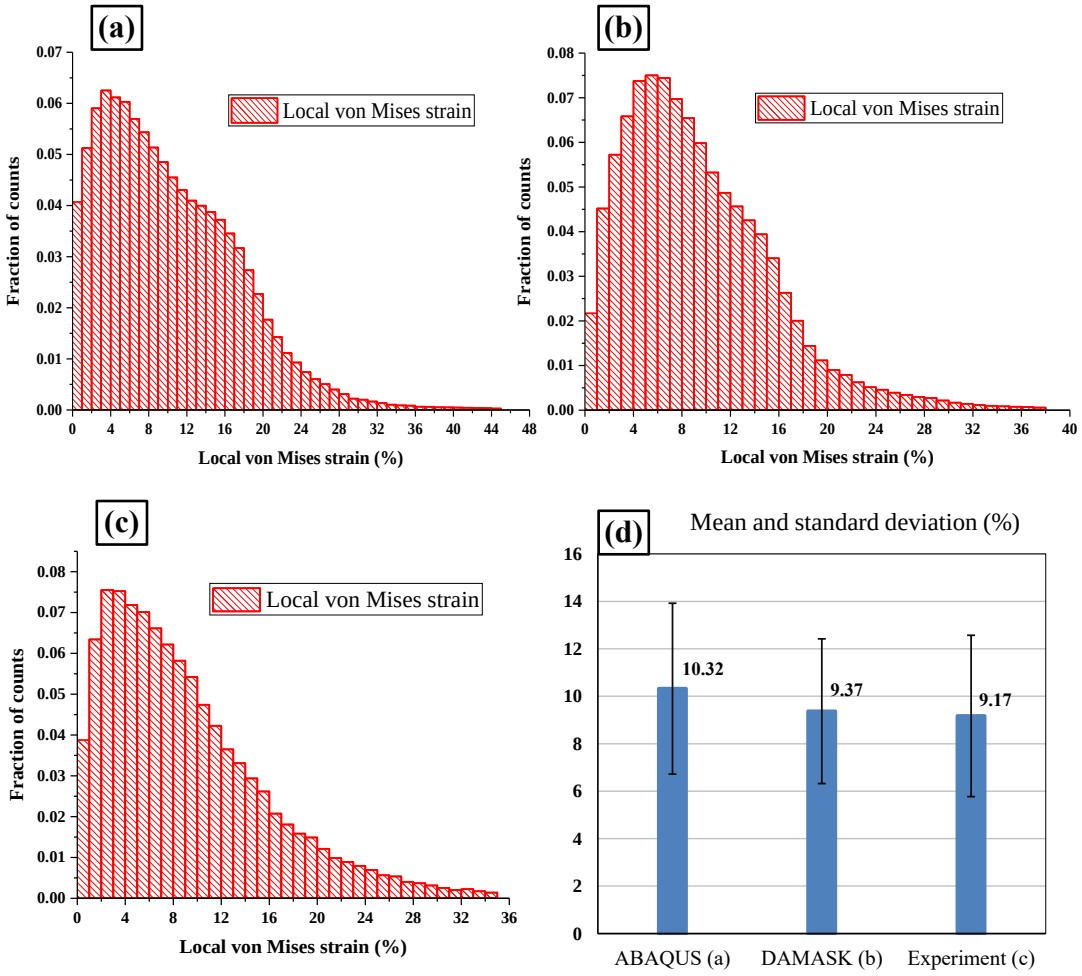

Figure 4.10. Strain distribution at 9% global strain from experiment and numerical simulations; (a) ABAQUS simulation (VPFEM), (b) DAMASK simulation (CPFFT), (c) *in-situ* tensile test [72], (d) The mean and standard deviation (SD) of these distributions.

4.5 Discussion

The observed localization patterns and strain concentration are indicators of damage initiation in the Continuously Cooled Carbide Free Bainitic Steels (CC-CFBS) or B360. The numerical simulations were performed in order to investigate the strain partitioning in B360, using a von Mises plastic finite element model (VPFEM) by Abaqus and also a phonemenological crystal plasticity with a fast Fourier transform solver (CPFFT) utilizing DAMASK. *In-situ* tensile experiment was performed in order to validate the numerical simulation results and to observe damage initiating factors in B360. Both simulations and the experiment were performed on the same geometry. In the numerical simulations, the RVE was constructed based on the assumption that all the blocky retained austenite turns into martensite from the beginning of the straining. This is a simplification based on the fact a that large part of the large islands of BRA (grain size > 0.25 μm) which are unstable, transform into martensite in a

deformation induced martensitic transformation mechanism which results in reduction in the fraction of retained austenite fraction in the microstructure [72]. TFRA (inside the bainitic lath) and also the ultrafine islands of BRA (grain size < 0.25 μm) are more stable [72,81,96–99] and do not transform into marteniste.

Simulated von Mises strain maps (Figure 4.7 and Figure 4.8) during different stages of tensile straining show a reasonable correlation with the *in-situ* experiment (Figure 4.9). Based on both simulations, von Mises strain localization is mostly due to presence of large martensitic islands and large BRA (grain size > 0.25 μm) which later transform into martenite in the microstructure. Very low degree of strain is endured by these martensitic islands and strain is localized in the narrow channels of bainite in the interfaces of martensite and bainitic ferrite. This is confirmed by *in-situ* tensile tests showing that there is strong strain concentration in bainite between martensitic islands and crack initiates from these interfaces of martensite and bainite and grows along the interfaces by fracturing of martensitic islands (Figure 4.9(d)) [72]. The narrower these channels are the higher the strain accumulation is. Channels which are narrower than the threshold value of 5 μm, accumulate much higher local strains than the wider channels.

Both numerical simulations give an acceptable estimate of the damage initiation sites in the microstructure of B360. While VPFEM uses a simpler material model and does not take into account the texture of the steel microstructure, it gives a good estimate of the strain localization areas. However, there is difference in the maximum local von Mises strain estimated by the VPFEM and CPFFT simulation results compared to *in-situ* experiment. At 9% of global strain VPFEM and CPFFT simulations show 28.5% and 8.5% error in estimating maximum local von Mises strain, respectively. The geometry and texture information for the phenomenological crystal plasticity model are easy to obtain directly using the EBSD data, however the phenomenological material model parameters for each phase must be calibrated using macroscopic flow curves for each phase. The CPFFT model takes into account texture information of each grain and with a more complex and accurate material model so that it gives better approximation of the maximum von Mises local strain together with the locations of these strain localizations.

The histograms of the von Mises strain distribution in the microstructure were also calculated and compared. The histograms resulted from the simulations differ slightly from the histogram of the *in-situ* test, especially the one from VPFEM by Abaqus. Considering the histogram from *in-situ* test, after reaching the peak area fraction (strains of 2-4%), it reduces in a logarithmic pattern while for the simulation results the rate of reduction is low in the strain ranges 12-17% and then increases. In other words, the area fraction for strain of 7-13% are higher for the *in-situ* experiment results compared to the simulation results while the area fraction of strains in the range of 12-17% are higher for simulation results. This is because of several reasons, one of them

being the simplification (in the numerical simulations) that all BRA transforms into martensite from the beginning of the straining. This simplification not only changes the area fraction of the local strains around 11% (average local strain ensured by BRA) and shift it towards much lower strains (because we consider they turn into martensite), but also changes the phase morphology and creates more area fraction of strains in the range of 12-17%.

The deviations (of strain localization maps) observed among the numerical simulations results (Figure 4.7(d), Figure 4.8(d)) and the *in-situ* experiment (Figure 4.9(d)) can also be the result of considering a two dimensional (2D) geometry instead of a three dimensional (3D) one. As an example, the left top corner of the specimen, with the LBF aggregated with martensite (shown by LBF+M in Figure 4.7(a)- Figure 4.9(a)), shows that in both numerical simulations, there is strain localization in the bainitic ferrite in the middle of this region. However, such strain localization was not observed in the *in-situ* experiment. This could be because that other martensitic layers under or above this LBF do not allow this softer constituent to strain as much as we observe in the 2D numerical models. Accuracy in geometry and RVE creation would help to include more microstrutural details such as lamellar structure of bainite (bainitic ferrite and retained austenite). Higher resolution imaging can also help to capture more details of the microstructure.

Choosing suitable material model and measuring accurately the mechanical behavior and (also possibly) damage characteristics for each phase would result in more accurate numerical models. Using nano-indentation technique in order to characterize the mechanical properties of each phase would help to obtain a more accurate estimation of the strain partitioning and damage initiation in steels [36]. The martensitic phase transformation and the stability of the retained austenite during deformation have significant influence on the mechanical behavior and ductility of steels which experience this phenomenon [35]. Therefore, considering deformation-induced martensitic phase transformation in the numerical material models is another very important step in simulating the strain partitioning behavior of these steels.

In summary, in order to increase the accuracy of the numerical models, there is a need for accurate geometry and precise material behavior modelling, i.e. we should try to represent the actual behavior of each phase/constituent with a suitable material model which also includes precise model parameters.

The carbide free bainitic steels do not contain cementite laths like pearlitic steels. These cementite laths in pearlitic steels can lead to the formation of brittle white etching layer (WEL) due to cementite dissolution under plastic deformation [100,101]. This WEL could be related to rolling contact fatigue in the rails [102]. However the void formation by strain incompatibility between hard martensite and bainite, makes this steel vulnerable to damage under rolling contact loading conditions as well [103].

4.6 Conclusion and future work

Strain partitioning in Continuously Cooled Carbide Free Bainitic Steels (CC-CFBS) (B360) was simulated using von Mises J2 plasticity and also phenomenological crystal plasticity material models. Both of these models give reasonable estimation of the strain localization pheonomena compared to *in-situ* tensile experiment which was used to validate these numerical simulations. However the phenomenological crystal plasticity model gives results closer to the *in-situ* tensile experiment than the von Mises plasticity model.

There were some deviations between the simulation results and the experiment, regarding the strain localization maps and also the maximum von Mises local strain estimation. These deviations could be due to simpler geometrical and material models considered in the model. For the geometry in the numerical models, a 2D RVE was used instead of a 3D microstructure. The retained austenite transfomation into martensite was neglected and the blocky retained austenite (BRA) was considered to transform into martensite at the beginning of the straining. This simplification was done since large BRA transform into martensite during loading in a strain-induced transformation mechanism. More accurate mechanical behavior modelling of each phase can be developed using more advanced methods such as nano-indentation. Considering damage characteristics of each phase can help to obtain a more realistic material model.

Factors such as martensite/bainitic ferrite interfaces, interface orientation with respect to tensile direction, spatial distribution of phases, phase fraction and phase morphology influence the strain partitioning and damage initiation in this carbide free bainitic steel. The martensitic islands and the large BRA (which transform into martensite under strain) present in B360 steel, could initiate damage which in general reduces the mechanical performance. The main damage mechanism in this steel is strain localization in the narrow channels of bainite and in the interfaces of bainite with martensite which later develops voids and eventually cracks which also leads to fracture of martensitic islands.

In order to design a better microstructure while benefitting from the absence of carbides, there is a need to improve this microstructure using the lessons learned from this research. To do so, elimination of large BRA and martensitic islands might help this steel to achieve better mechanical and damage characteristics.

4.7 References

[1] R. Dollevoet, Design of an anti-head check profile based on stress relief, 2016. https://doi.org/10.3990/1.9789036530736.

[2] R. Dollevoet, Z. Li, O. Arias-Cuevas, A Method for the Prediction of Head Checking Initiation Location and Orientation under Operational Loading Conditions, Proc. Inst. Mech. Eng. Part F J. Rail Rapid Transit. 224 (2010) 369–374. https://doi.org/10.1243/09544097JRRT368.

[3] Z. Li, X. Zhao, C. Esveld, R. Dollevoet, M. Molodova, An investigation into the causes of squats-Correlation analysis and numerical modeling, Wear. 265 (2008) 1349–1355. https://doi.org/10.1016/j.wear.2008.02.037.

[4] W.J. Jiang, C. Liu, C.G. He, J. Guo, W.J. Wang, Q.Y. Liu, Investigation on impact wear and damage mechanism of railway rail weld joint and rail materials, Wear. 376–377 (2017) 1938–1946. https://doi.org/10.1016/j.wear.2017.02.035.

[5] R. Lewis, R.S. Dwyer-Joyce, Wear mechanisms and transitions in railway wheel steels, Proc. Inst. Mech. Eng. Part J J. Eng. Tribol. 218 (2004) 467–478. https://doi.org/10.1243/1350650042794815.

[6] K.M. Lee, A.A. Polycarpou, Wear of conventional pearlitic and improved bainitic rail steels, Wear. 259 (2005) 391–399. https://doi.org/10.1016/j.wear.2005.02.058.

[7] H.A. Aglan, Z.Y. Liu, M.F. Hassan, M. Fateh, Mechanical and fracture behavior of bainitic rail steel, J. Mater. Process. Technol. 151 (2004) 268–274. https://doi.org/10.1016/j.jmatprotec.2004.04.073.

[8] H.K.D.H. Bhadeshia, High Performance Bainitic Steels, Mater. Sci. Forum. 500–501 (2005) 63–74. https://doi.org/10.4028/www.scientific.net/MSF.500-501.63.

[9] T. Suzuki, Y. Ono, G. Miyamoto, T. Furuhara, Effects of Si and Cr on Bainite Microstructure of Medium Carbon Steels, ISIJ Int. 50 (2010) 1476–1482. https://doi.org/10.2355/isijinternational.50.1476.

[10] X.Y. Long, J. Kang, B. Lv, F.C. Zhang, Carbide-free bainite in medium carbon steel, Mater. Des. 64 (2014) 237–245. https://doi.org/10.1016/j.matdes.2014.07.055.

[11] H.K.D.H. Bhadeshia, Nanostructured bainite, Proc. R. Soc. A Math. Phys. Eng. Sci. 466 (2010) 3–18. https://doi.org/10.1098/rspa.2009.0407.

[12] H.K.D.H. Bhadeshia, The first bulk nanostructured metal, Sci. Technol. Adv. Mater. 14 (2013). https://doi.org/10.1088/1468-6996/14/1/014202.

[13] F.G. Caballero, C. Garcia-Mateo, M.K. Miller, Design of novel bainitic steels: Moving from ultrafine to nanoscale structures, Jom. 66 (2014) 747–755. https://doi.org/10.1007/s11837-014-0908-0.

[14] K.-H. Kim, J.-S. Lee, On microstructure and properties of Si modified 100Cr6 bearing steels, Mater. Sci. Technol. 28 (2012) 50–54. https://doi.org/10.1179/1743284711Y.0000000053.

[15] X. Gui, K. Wang, G. Gao, R.D.K. Misra, Z. Tan, B. Bai, Rolling contact fatigue of bainitic rail steels: The significance of microstructure, Mater. Sci. Eng. A. 657 (2016) 82–85. https://doi.org/10.1016/j.msea.2016.01.052.

[16] K. Chung, N. Ma, T. Park, D. Kim, D. Yoo, C. Kim, A modified damage model for advanced high strength steel sheets, Int. J. Plast. 27 (2011) 1485–1511. https://doi.org/10.1016/j.ijplas.2011.01.007.

[17] M. Brünig, S. Gerke, V. Hagenbrock, Stress-state-dependence of damage strain rate tensors caused by growth and coalescence of micro-defects, 63 (2014) 49–63. https://doi.org/10.1016/j.ijplas.2014.04.007.

[18] L. Malcher, E.N. Mamiya, An improved damage evolution law based on continuum damage mechanics and its dependence on both stress triaxiality and the third invariant, Int. J. Plast. 56 (2014) 232–261. https://doi.org/10.1016/j.ijplas.2014.01.002.

[19] M. Brünig, S. Gerke, Simulation of damage evolution in ductile metals undergoing dynamic loading conditions, 27 (2011) 1598–1617. https://doi.org/10.1016/j.ijplas.2011.02.003.

[20] M. Brünig, S. Gerke, V. Hagenbrock, Micro-mechanical studies on the effect of the stress triaxiality and the Lode parameter on ductile damage, Int. J. Plast. 50 (2013) 49–65. https://doi.org/10.1016/j.ijplas.2013.03.012.

[21] M. Brünig, O. Chyra, D. Albrecht, L. Driemeier, M. Alves, A ductile damage criterion at various stress triaxialities, 24 (2008) 1731–1755. https://doi.org/10.1016/j.ijplas.2007.12.001.

[22] J.V.S. Cavalheiro, L. Malcher, Assessment of third invariant elasto-plastic models_ Mathematical aspects, numerical strategies and comparative results, Finite Elem. Anal. Des. 123 (2017) 51–69. https://doi.org/10.1016/j.finel.2016.09.001.

[23] L. Malcher, F.M.A. Pires, J.M.A.C. De Sá, An extended GTN model for ductile fracture under high and low stress triaxiality, Int. J. Plast. 54 (2014) 193–228. https://doi.org/10.1016/j.ijplas.2013.08.015.

[24] J.Q. Ran, M.W. Fu, A hybrid model for analysis of ductile fracture in micro-scaled plastic deformation of multiphase alloys, 61 (2014) 1–16. https://doi.org/10.1016/j.ijplas.2013.11.006.

[25] M. Basirat, T. Shrestha, G.P. Potirniche, I. Charit, K. Rink, A study of the creep behavior of modified 9Cr – 1Mo steel using continuum-damage modeling, Int. J. Plast. 37 (2012) 95–107. https://doi.org/10.1016/j.ijplas.2012.04.004.

[26] C.F.B. Sandoval, L. Malcher, F.A. Canut, L.M. Araújo, T.C.R. Doca, J.A. Araújo, Micromechanical Gurson-based continuum damage under the context of fretting fatigue: influence of the plastic strain field., Int. J. Plast. (2019). https://doi.org/10.1016/j.ijplas.2019.09.012.

[27] J. Kim, J. Whan, Necking behavior of AA 6022-T4 based on the crystal plasticity and damage models, Int. J. Plast. 73 (2015) 3–23. https://doi.org/10.1016/j.ijplas.2015.06.013.

[28] M. Knezevic, I.J. Beyerlein, D.W. Brown, T.A. Sisneros, C.N. Tomé, A polycrystal plasticity model for predicting mechanical response and texture evolution during strain-path changes : Application to beryllium, Int. J. Plast. 49 (2013) 185–198. https://doi.org/10.1016/j.ijplas.2013.03.008.

[29] A.S. Khan, J. Liu, J. Whan, R. Nambori, Strain rate effect of high purity aluminum single crystals : Experiments and simulations, Int. J. Plast. 67 (2015) 39–52. https://doi.org/10.1016/j.ijplas.2014.10.002.

[30] M. Ardeljan, I.J. Beyerlein, M. Knezevic, Journal of the Mechanics and Physics of Solids A dislocation density based crystal plasticity finite element model : Application to a two-phase polycrystalline HCP / BCC composites, J. Mech. Phys. Solids. 66 (2014) 16–31. https://doi.org/10.1016/j.jmps.2014.01.006.

[31] M. Knezevic, H.F. Al-harbi, S.R. Kalidindi, Crystal plasticity simulations using discrete Fourier transforms, Acta Mater. 57 (2009) 1777–1784. https://doi.org/10.1016/j.actamat.2008.12.017.

[32] P. Hu, Y. Liu, Y. Zhu, L. Ying, Crystal plasticity extended models based on thermal mechanism and damage functions : Application to multiscale modeling of aluminum alloy tensile behavior, Int. J. Plast. 86 (2016) 1–25. https://doi.org/10.1016/j.ijplas.2016.07.001.

[33] J. Ha, J. Lee, J. Hoon, M. Lee, Investigation of plastic strain rate under strain path changes in dual-phase steel using microstructure-based modeling d e, 93 (2017). https://doi.org/10.1016/j.ijplas.2017.02.005.

[34] X. Shang, H. Zhang, Z. Cui, M.W. Fu, J. Shao, A multiscale investigation into the effect of grain size on void evolution and ductile fracture : Experiments and crystal plasticity modeling, (2019). https://doi.org/10.1016/j.ijplas.2019.09.009.

[35] K.S. Choi, W.N. Liu, X. Sun, M.A. Khaleel, Microstructure-based constitutive modeling of TRIP steel: Prediction of ductility and failure modes under different loading conditions, Acta Mater. 57 (2009) 2592–2604. https://doi.org/10.1016/j.actamat.2009.02.020.

[36] C.C. Tasan, J.P.M. Hoefnagels, M. Diehl, D. Yan, F. Roters, D. Raabe, Strain localization and damage in dual phase steels investigated by coupled in-situ

deformation experiments and crystal plasticity simulations, Int. J. Plast. 63 (2014) 198–210. https://doi.org/10.1016/j.ijplas.2014.06.004.

[37] K. Alharbi, H. Ghadbeigi, P. Efthymiadis, M. Zanganeh, S. Celotto, R. Dashwood, C. Pinna, Damage in dual phase steel DP1000 investigated using digital image correlation and microstructure simulation, Model. Simul. Mater. Sci. Eng. 23 (2015). https://doi.org/10.1088/0965-0393/23/8/085005.

[38] B. Berisha, C. Raemy, C. Becker, M. Gorji, P. Hora, Multiscale modeling of failure initiation in a ferritic – pearlitic steel, Acta Mater. 100 (2015) 191–201. https://doi.org/10.1016/j.actamat.2015.08.035.

[39] B. Erice, C.C. Roth, D. Mohr, Mechanics of Materials Stress-state and strain-rate dependent ductile fracture of dual and complex phase steel, Mech. Mater. 116 (2018) 11–32. https://doi.org/10.1016/j.mechmat.2017.07.020.

[40] X. Sun, K.S. Choi, A. Soulami, W.N. Liu, M.A. Khaleel, On key factors influencing ductile fractures of dual phase (DP) steels, Mater. Sci. Eng. A. 526 (2009) 140–149. https://doi.org/10.1016/j.msea.2009.08.010.

[41] X. Sun, K.S. Choi, W.N. Liu, M.A. Khaleel, Predicting failure modes and ductility of dual phase steels using plastic strain localization, Int. J. Plast. 25 (2009) 1888–1909. https://doi.org/10.1016/j.ijplas.2008.12.012.

[42] A. Ramazani, M. Abbasi, S. Kazemiabnavi, S. Schmauder, R. Larson, U. Prahl, Development and application of a microstructure-based approach to characterize and model failure initiation in DP steels using XFEM, Mater. Sci. Eng. A. 660 (2016) 181–194. https://doi.org/10.1016/j.msea.2016.02.090.

[43] J. Kadkhodapour, S. Schmauder, D. Raabe, S. Ziaei-Rad, U. Weber, M. Calcagnotto, Experimental and numerical study on geometrically necessary dislocations and non-homogeneous mechanical properties of the ferrite phase in dual phase steels, Acta Mater. 59 (2011) 4387–4394. https://doi.org/10.1016/j.actamat.2011.03.062.

[44] J. Kadkhodapour, A. Butz, S. Ziaei-Rad, S. Schmauder, A micro mechanical study on failure initiation of dual phase steels under tension using single crystal plasticity model, Int. J. Plast. 27 (2011) 1103–1125. https://doi.org/10.1016/j.ijplas.2010.12.001.

[45] D. Kim, E. Kim, J. Han, W. Woo, S. Choi, Effect of microstructural factors on void formation by ferrite / martensite interface decohesion in DP980 steel under uniaxial tension, Int. J. Plast. 94 (2017) 3–23. https://doi.org/10.1016/j.ijplas.2017.04.019.

[46] A. Das, S. Tarafder, S. Sivaprasad, D. Chakrabarti, Materials Science & Engineering A In fl uence of microstructure and strain rate on the strain partitioning behaviour of dual phase steels, Mater. Sci. Eng. A. 754 (2019) 348–360. https://doi.org/10.1016/j.msea.2019.03.084.

[47] T. Matsuno, C. Teodosiu, D. Maeda, A. Uenishi, Mesoscale simulation of the early evolution of ductile fracture in dual-phase steels, Int. J. Plast. 74 (2015) 17–34. https://doi.org/10.1016/j.ijplas.2015.06.004.

[48] A.C. Darabi, H.R. Chamani, J. Kadkhodapour, A.P. Anaraki, A. Alaie, M.R. Ayatollahi, Mechanics of Materials Micromechanical analysis of two heat-treated dual phase steels : DP800 and DP980, 110 (2017) 68–83.

[49] J. Hoon, D. Kim, F. Barlat, M. Lee, Crystal plasticity approach for predicting the Bauschinger effect in dual-phase steels, Mater. Sci. Eng. A. 539 (2012) 259–270. https://doi.org/10.1016/j.msea.2012.01.092.

[50] C.C. Roth, T.F. Morgeneyer, Y. Cheng, L. Helfen, D. Mohr, Ductile damage mechanism under shear-dominated loading : In-situ tomography experiments on dual phase steel and localization analysis, Int. J. Plast. 109 (2018) 169–192. https://doi.org/10.1016/j.ijplas.2018.06.003.

[51] N. Fujita, N. Ishikawa, F. Roters, C.C. Tasan, D. Raabe, Experimental-numerical study on strain and stress partitioning in bainitic steels with martensite-austenite constituents, Int. J. Plast. 104 (2018) 39–53. https://doi.org/10.1016/j.ijplas.2018.01.012.

[52] U. Liedl, S. Traint, E.A. Werner, An unexpected feature of the stress–strain diagramof dual-phase steel, 25 (2002) 122–128.

[53] Z. Zhao, M. Ramesh, D. Raabe, A.M. Cuitiño, R. Radovitzky, Investigation of three-dimensional aspects of grain-scale plastic surface deformation of an aluminum oligocrystal, Int. J. Plast. 24 (2008) 2278–2297. https://doi.org/10.1016/j.ijplas.2008.01.002.

[54] L. Wang, R.I. Barabash, Y. Yang, T.R. Bieler, M.A. Crimp, P. Eisenlohr, W. Liu, G.E. Ice, Experimental characterization and crystal plasticity modeling of heterogeneous deformation in polycrystalline α-Ti, Metall. Mater. Trans. A Phys. Metall. Mater. Sci. 42 (2011) 626–635. https://doi.org/10.1007/s11661-010-0249-8.

[55] S.-H. Choi, E.-Y. Kim, W. Woo, S.H. Han, J.H. Kwak, The effect of crystallographic orientation on the micromechanical deformation and failure behaviors of DP980 steel during uniaxial tension, 45 (2013) 85–102. https://doi.org/10.1016/j.ijplas.2012.11.013.

[56] D. Cédat, O. Fandeur, C. Rey, D. Raabe, Polycrystal model of the mechanical behavior of a Mo-TiC30vol.% metal-ceramic composite using a 3D microstructure map obtained by a dual beam FIB-SEM, Acta Mater. 60 (2012) 1623–1632.

[57] J. Kang, Y. Ososkov, J.D. Embury, D.S. Wilkinson, Digital image correlation studies for microscopic strain distribution and damage in dual phase steels, Scr. Mater. 56 (2007) 999–1002. https://doi.org/10.1016/j.scriptamat.2007.01.031.

[58] H. Ghadbeigi, C. Pinna, S. Celotto, J.R. Yates, Local plastic strain evolution in a high strength dual-phase steel, Mater. Sci. Eng. A. 527 (2010) 5026–5032. https://doi.org/10.1016/j.msea.2010.04.052.

[59] M. Kapp, T. Hebesberger, O. Kolednik, A micro-level strain analysis of a high-strength dual-phase steel, Int. J. Mat. Res. 102 (2011) 687–691.

[60] J. Marteau, H. Haddadi, S. Bouvier, Investigation of Strain Heterogeneities Between Grains in Ferritic and Ferritic-Martensitic Steels, Exp. Mech. 53 (2013) 427–439. https://doi.org/10.1007/s11340-012-9657-6.

[61] C.C. Tasan, J.P.M. Hoefnagels, M.G.D. Geers, Microstructural Banding Effects Clarified Through Micrographic Digital Image Correlation, Scr. Mater. 62 (2010) 835–838. https://pure.mpg.de/pubman/item/item_2015292_2 (accessed November 15, 2018).

[62] G. Martin, C.W. Sinclair, R.A. Lebensohn, Microscale plastic strain heterogeneity in slip dominated deformation of magnesium alloy containing rare earth, Mater. Sci. Eng. A. 603 (2014) 37–51. https://doi.org/10.1016/j.msea.2014.01.102.

[63] H. Lim, J.D. Carroll, C.C. Battaile, T.E. Buchheit, B.L. Boyce, C.R. Weinberger, Grain-scale experimental validation of crystal plasticity finite element simulations of tantalum oligocrystals, Int. J. Plast. 60 (2014) 1–18. https://doi.org/10.1016/j.ijplas.2014.05.004.

[64] C.C. Tasan, M. Diehl, D. Yan, C. Zambaldi, P. Shanthraj, F. Roters, D. Raabe, Integrated experimental-simulation analysis of stress and strain partitioning in multiphase alloys, Acta Mater. 81 (2014) 386–400. https://doi.org/10.1016/j.actamat.2014.07.071.

[65] F. Roters, P. Eisenlohr, C. Kords, D.D. Tjahjanto, M. Diehl, D. Raabe, DAMASK: the Düsseldorf Advanced MAterial Simulation Kit for studying crystal plasticity using an FE based or a spectral numerical solver, Procedia IUTAM. 3 (2012) 3–10. https://doi.org/10.1016/j.piutam.2012.03.001.

[66] R.A. Lebensohn, A.D. Rollett, P. Suquet, Fast fourier transform-based modeling for the determination of micromechanical fields in polycrystals, Jom. 63 (2011) 13–18. https://doi.org/10.1007/s11837-011-0037-y.

[67] H.-S. Yang, Design of Low-Carbon, Low-Temperature Bainite, 2011.

[68] O. Hajizad, A. Kumar, Z. Li, R.H. Petrov, J. Sietsma, Influence of Microstructure on Mechanical Properties of Bainitic Steels in Railway Applications, (2019) 1–19.

[69] A.W. Wilson, J.D. Madison, G. Spanos, Determining phase volume fraction in steels by electron backscattered diffraction, Scr. Mater. 45 (2001) 1335–1340. https://doi.org/10.1016/S1359-6462(01)01137-X.

[70] J. Wu, P.J. Wray, C.I. Garcia, M. Hua, A.J. Deardo, Image quality analysis: A new method of characterizing microstructures, ISIJ Int. 45 (2005) 254–262. https://doi.org/10.2355/isijinternational.45.254.

[71] R. Hill, Elastic properties of reinforced solids: Some theoretical principles, J. Mech. Phys. Solids. 11 (1963) 357–372. https://doi.org/10.1016/0022-5096(63)90036-X.

[72] A. Kumar, A. Dutta, S.K. Makineni, M. Herbig, R.H. Petrov, J. Sietsma, In-situ observation of strain partitioning and damage development in continuously cooled carbide-free bainitic steels using micro digital image correlation, Mater. Sci. Eng. A. 757 (2019) 107–116. https://doi.org/10.1016/j.msea.2019.04.098.

[73] M. Latypov, S. Shin, B. De Cooman, H. Kim, Micromechanical finite element analysis of strain partitioning in multiphase medium manganese TWIP+TRIP steel, 2016. https://doi.org/10.1016/j.actamat.2016.02.001.

[74] R.-M. Rodriguez, I. Gutiérrez, Unified Formulation to Predict the Tensile Curves of Steels with Different Microstructures, Mater. Sci. Forum. 426–432 (2003) 4525–4530. https://doi.org/10.4028/www.scientific.net/MSF.426-432.4525.

[75] Y. Bergström, A dislocation model for the stress-strain behaviour of polycrystalline α-Fe with special emphasis on the variation of the densities of mobile and immobile dislocations, Mater. Sci. Eng. 5 (1970) 193–200. https://doi.org/10.1016/0025-5416(70)90081-9.

[76] Y. Estrin, H. Mecking, A unified phenomenological description of work hardening and creep based on one-parameter models, Acta Metall. 32 (1984) 57–70. https://doi.org/10.1016/0001-6160(84)90202-5.

[77] J.G. Sevillano, No Title, in: H. Mughrabi (Ed.), Plast. Deform. Fract. Mater. Mater. Sci. Technol. Vol. 6, Weinheim, Germany, 1993: p. 19.

[78] R.F. Hehemann, Phase Transformation, in: Am. Soc. Met., Metals Park, Ohio, 1970: p. 397.

[79] M.-X. Zhang, P.M. Kelly, Determination of Carbon Content in Bainitic Ferrite and Carbon Distribution in Austenite by Using CBKLDP, Mater. Charact. 40 (1998) 159–168. https://doi.org/https://doi.org/10.1016/S1044-5803(98)00005-9.

[80] A. Ramazani, P.T. Pinard, S. Richter, A. Schwedt, U. Prahl, Characterisation of microstructure and modelling of flow behaviour of bainite-aided dual-phase steel, Comput. Mater. Sci. 80 (2013) 134–141. https://doi.org/10.1016/j.commatsci.2013.05.017.

[81] H.K.D.H. Bhadeshia, Bainite in Steels: Transformations, Microstructure and Properties, Second, IOM Communications Ltd, London, 2001. https://books.google.co.id/books?id=sF5RAAAAMAAJ.

[82] K. Zhu, O. Bouaziz, C. Oberbillig, M. Huang, An approach to define the effective lath size controlling yield strength of bainite, Mater. Sci. Eng. A. 527 (2010) 6614–6619. https://doi.org/10.1016/j.msea.2010.06.061.

[83] A. Ramazani, K. Mukherjee, A. Abdurakhmanov, U. Prahl, M. Schleser, Materials Science & Engineering A Micro – macro-characterisation and modelling of mechanical properties of gas metal arc welded (GMAW) DP600 steel, 589 (2013) 1–14.

[84] G. Béres, Z. Weltsch, Estimation of Strength Properties from Microhardness Results in Dual Phase Steels with Different Martensite Volume Fraction, Period. Polytech. Transp. Eng. (2018) 1–7. https://doi.org/10.3311/PPtr.12113.

[85] C. Thomser, Modelling of the mechanical properties of dual phase steels based on microstructure, Aachen, Techn. Univ., 2009.

[86] A. Ramazani, Y. Chang, U. Prahl, Characterization and modeling of failure initiation in bainite-aided DP steel, Adv. Eng. Mater. 16 (2014) 1370–1380. https://doi.org/10.1002/adem.201300556.

[87] T. Gladman, D. Dulieu, I. McIvor, Structure–Property Relationships in High Strength Microalloyed Steels, in: Microalloying 75, New York, 1977.

[88] C. Cayron, ARPGE : a computer program to automatically reconstruct the parent grains from electron backscatter diffraction data , J. Appl. Crystallogr. 40 (2007) 1183–1188. https://doi.org/10.1107/s0021889807048777.

[89] A. Anthoine, Derivation of the in-plane elastic characteristics of masonry through homogenization theory, Int. J. Solids Struct. 32 (1995) 137–163. https://doi.org/10.1016/0020-7683(94)00140-R.

[90] V.G. Kouznetsova, Computational homogenization for the multi-scale analysis of multi-phase materials, 2002. https://doi.org/10.6100/IR560009.

[91] F. Roters, D. Raabe, G. Gottstein, Work hardening in heterogeneous alloys - a microstructural approach based on three internal state variables, Acta Mater. 48 (2000) 4181–4189. https://doi.org/10.1016/S1359-6454(00)00289-5.

[92] C. Reuber, P. Eisenlohr, F. Roters, D. Raabe, Dislocation density distribution around an indent in single-crystalline nickel: Comparing nonlocal crystal plasticity finite-element predictions with experiments, Acta Mater. 71 (2014) 333–348. https://doi.org/10.1016/j.actamat.2014.03.012.

[93] F. Roters, P. Eisenlohr, L. Hantcherli, D.D. Tjahjanto, T.R. Bieler, D. Raabe, Overview of constitutive laws, kinematics, homogenization and multiscale methods in crystal plasticity finite-element modeling: Theory, experiments, applications, Acta Mater. 58 (2010) 1152–1211. https://doi.org/10.1016/j.actamat.2009.10.058.

[94] D. Peirce, R.J. Asaro, A. Needleman, An analysis of nonuniform and localized deformation in ductile single crystals, Acta Metall. 30 (1982) 1087–1119. https://doi.org/10.1016/0001-6160(82)90005-0.

[95] G. Voronoi, Nouvelles applications des paramètres continus à la théorie des formes quadratiques. Deuxième mémoire. Recherches sur les parallélloèdres primitifs., J. Für Die Reine Und Angew. Math. 134 (1908) 198–287. http://eudml.org/doc/149291.

[96] D. Q. Bai, A. Di Chiro, S. Yue, Stability of Retained Austenite in a Nb Microalloyed Mn-Si TRIP Steel, 1998. https://doi.org/10.4028/www.scientific.net/MSF.284-286.253.

[97] C. Garcia-Mateo, F.G. Caballero, J. Chao, C. Capdevila, C. Garcia De Andres, Mechanical stability of retained austenite during plastic deformation of super high strength carbide free bainitic steels, J. Mater. Sci. 44 (2009) 4617–4624. https://doi.org/10.1007/s10853-009-3704-4.

[98] C. García-Mateo, F.G. Caballero, The role of retained austenite on tensile properties of steels with bainitic microstructures, Mater. Trans. 46 (2005) 1839–1846. https://doi.org/10.2320/matertrans.46.1839.

[99] A.S. Podder, I. Lonardelli, A. Molinari, H.K.D.H. Bhadeshia, Thermal stability of retained austenite in bainitic steel: An in situ study, Proc. R. Soc. A Math. Phys. Eng. Sci. 467 (2011) 3141–3156. https://doi.org/10.1098/rspa.2011.0212.

[100] W. Österle, H. Rooch, A. Pyzalla, L. Wang, Investigation of white etching layers on rails by optical microscopy, electron microscopy, X-ray and synchroton X-ray diffraction, Mater. Sci. Eng. A. 303 (2001) 150–157. https://doi.org/10.1016/S0921-5093(00)01842-6.

[101] W. Lojkowski, M. Djahanbakhsh, G. Bürkle, S. Gierlotka, W. Zielinski, H.J. Fecht, Nanostructure formation on the surface of railway tracks, Mater. Sci. Eng. A. 303 (2001) 197–208. https://doi.org/10.1016/S0921-5093(00)01947-X.

[102] M. Steenbergen, R. Dollevoet, On the mechanism of squat formation on train rails - Part I: Origination, Int. J. Fatigue. 47 (2013) 361–372. https://doi.org/10.1016/j.ijfatigue.2012.04.023.

[103] W. Solano-Alvarez, E.J. Pickering, H.K.D.H. Bhadeshia, Degradation of nanostructured bainitic steel under rolling contact fatigue, Mater. Sci. Eng. A. 617 (2014) 156–164. https://doi.org/10.1016/j.msea.2014.08.071.

5 Crystal plasticity modelling of strain partitioning in high strength carbide free bainitic steel and validation using *in-situ* tensile experiment‡

In this chapter, local strain distributions in the specially designed high strength carbide free bainitic steel (CFBS) are examined, using a combined numerical and experimental approach. To obtain a fully bainitic microstructure in this CFBS an isothermal heat treatment was employed.

The application of high strength bainitic steels with complex microstructure requires understanding of strain distribution and deformation localization at the microscopic scale. In order to do so, crystal plasticity material modeling was conducted with a spectral solver, together with realistic grain morphology and crystallographic orientation which was obtained through electron backscatter diffraction (EBSD). The simulations were performed using DAMASK (the Düsseldorf Advanced Material Simulation Kit).

The results from the micromechanical simulations were validated using *in-situ* tensile experiments. In order to capture the local von-Mises strain distribution maps, micro-digital image correlation (μDIC) in Scanning Electron Microscopy (SEM) was incorporated. There was reasonable correspondence between the numerical and experimental results although some deviations were observed. The results show significant reduction in the strain localization in the designed CFBS compared to a previously studied continuously cooled carbide-free bainitic steel with the same chemical composition but different microstructure.

‡ This chapter is based on an article submitted to a journal for publication.

5.1 Introduction

Rails are repetitively under high contact loads from wheels, which with time leads to rolling contact fatigue damage [1–4] and wear [5–7] of rails. This causes financial issues due to maintenance and replacement costs and also safety concerns. Therefore, with constant increase in vehicle speed and axle load, rail transportation is seeking new materials which are more resistant to damage formation under such working conditions. The majority of the steels used in rails are pearlitic. However, more recently bainitic steels have shown superior mechanical properties such as high strength and toughness which could make them good candidates for such applications [8–10].

Previous research shows that carbide free bainitic steels (CFBSs) offer better rolling contact fatigue (RCF) resistance than conventional pearlitic steels [11,12]. In these steels, the cementite precipitation during austenite decomposition is retarded by the addition of Si which results in absence of inter lath cementite in the bainitic microstructure [13]. These steels show great fatigue life during uniaxial fatigue tests [14–17] and also excellent abrasive and rolling-sliding wear resistance [18–22]. Because of these very good mechanical and rolling contact fatigue properties CFBSs are used to manufacture bearings, gears and rails [23–25]. These good properties are derived from the complex microstructures of CFBSs which depend on the chemical constituents and the heat treatment.

Grains are oriented differently and show different micromechanical lattice responses under applied macroscopic stress. As a result, elastic and plastic anisotropy due to the grain orientation dependence causes stress/strain partitioning. On the other hand, such complex alloys usually consist of different phases with different mechanical properties and this may lead to further non-uniform partition of stresses/strains among different phases. Severe stress/strain partitioning can later lead to initiation and propagation of (micro-) cracks. Therefore, taking into account the stress or strain localization regions in the microstructure is of crucial importance when investigating the damage initiation in steels [26,27]. This requires experimental and numerical investigations of damage initiation mechanisms at microstructure level. The gained information would help to design new microstructures with better mechanical properties [28,29].

The use of *in-situ* experiments in order to study the local deformation fields and their effects on damage in steels has been reported in many works [26,30–34]. During these experiments, microstructural imaging is performed to capture the local strain distribution. Numerical models can also be used in order to capture strain and stress fields. These models could incorporate a simplified geometry [35,36] or a more realistic one [37–46]. However a few researchers have performed both numerical and experimental analysis, using the same actual geometry to examine the deformation partitioning [47,48]. Most of these numerical and experimental studies have

investigated dual phase steels which consist of ferrite and martensite. Few damage initiation and strain partitioning studies have been performed on bainitic steels or steels which include bainite as a constitutive element [28,38]. There is still a need for further development of numerical models for complex bainitic microstructures.

According to our previous research [49], isothermally formed CFBS shows better mechanical properties compared to other bainitic grades (used in railway) and also continuously cooled CFBS. Fine bainitic ferrite laths together with the carbon-rich retained austenite films help to achieve high strength, toughness and hardness in this bainitic steel [50–52]. In order to understand the damage initiation behavior in isothermally formed CFBS (which we will name as B360-HT in this study), a strain partitioning analysis is performed on the microstructure of this steel. Numerical simulations were performed, taking into account the polycrystalline plasticity and a microstructure with details of realistic grain morphology and crystallographic orientations obtained through electron backscatter diffraction (EBSD). Strain maps captured from *in-situ* tensile experiments with micro-digital image correlation (μDIC) in Scanning Electron Microscopy (SEM) in combination with EBSD were used to check the validity of the numerical simulation results. Finally a discussion and the conclusions are presented.

5.2 Methodology

5.2.1 Material and heat treatment

The chemical composition of high strength CFBS (B360-HT) is measured using combined use of Optical Emission Spectrometry (OES) and X-ray Fluorescence Spectrometry (XRF) techniques and is shown in Table 5.1. The isothermal heat treatment used for this steel is illustrated in Figure 5.1. Using high concentration of silicon suppresses the carbide formation in the bainitic microstructure [53,54] and low carbon content would result in better weldability and fast bainitic formation kinetics [55].

Table 5.1. Chemical composition of B360-HT bainitic steel in wt%.

Steel Grade	C	Cr	Mn	Si	V	Mo
B360	0.269	0.51	1.547	1.36	0.033	0.148

In an earlier research it was shown that the strength and toughness of the bainitic rail steels, which were produced using continuous cooling, could be enhanced by employing the isothermal heat treatment [49]. During this heat treatment, the samples were first heated up to 900 °C and kept for 600 s (10 minutes), then transferred to a salt

bath with temperature 330 °C where they were held for 60 minutes (3600 s) and subsequently quenched in oil.

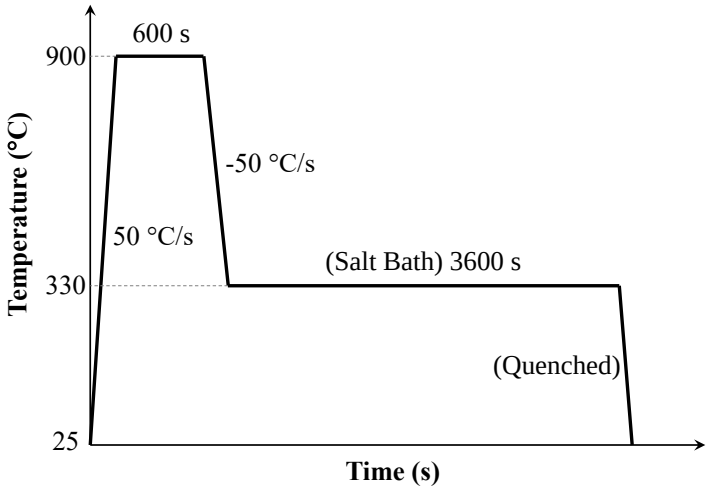

Figure 5.1. Isothermal heat treatment process performed on B360-HT steel.

5.2.1.1 EBSD analysis

The EBSD characterization was done by an FEI Quanta-450 SEM which utilizes a Field Emission Gun (FEG). In order to capture EBSD data, a Hikari-Pro EBSD detector with an EDAX-TSL OIM Data Collection software was used. Step size of 50 nm with a hexagonal scan grid and an accelerating voltage of 15 kV were chosen. TSL-OIM v. 7.0 software was further used to analyze the data. The points which had a confidence index less than 0.1 were removed from quantification as dubious.

The EBSD phase map and the image quality (IQ) with a phase map of retained austenite colored in green are shown in Figure 5.2(a), (b) respectively. The microstructure of the heat treated steel consist of fine bainitic ferrite laths with about 2.8% retained austenite situated between the laths.

The size of the blocky retained austenite (BRA) is significantly reduced in B360-HT compared to the microstructure which was known as B360-AR without applying the heat treatment [56].

According to [57–59] the smaller size of the blocky retained austenite offers a higher mechanical and thermal stability due to the carbon enrichment during bainitic transformation. Additionally, no martensite was formed during the quenching after bainitic treatment. Martensite phase is easy to identify as dark regions in the grey scale IQ maps and as it can be seen such regions does not exist in Figure 5.2(b).

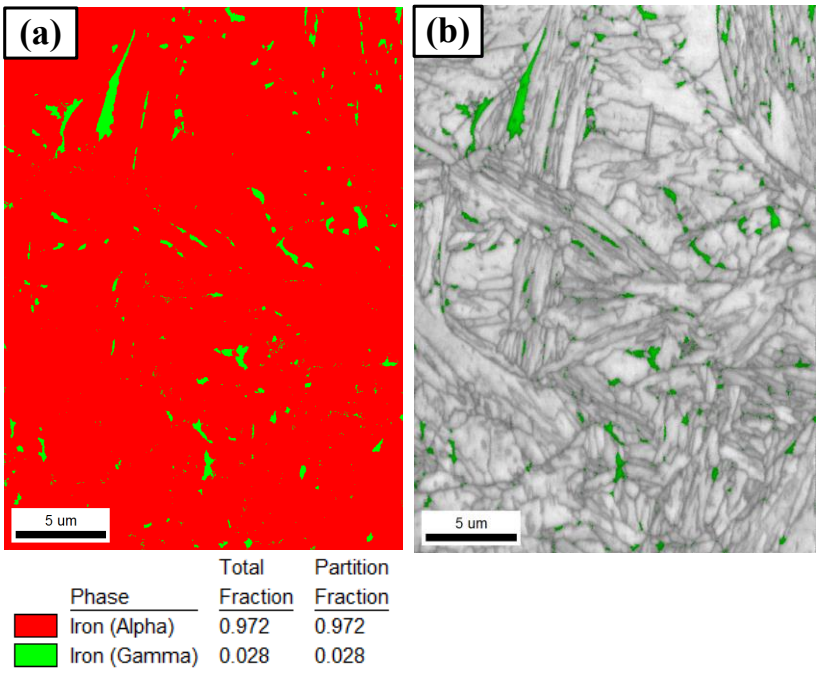

Figure 5.2. EBSD maps of B360-HT, (a) The phase map, (b) IQ and phase map indicating retained austenite in green.

5.2.2 Numerical modelling

To model the microstructure behavior under tensile loading, a crystal plasticity (CP) material model within the framework of the Düsseldorf Advanced Material Simulation Kit (DAMASK) [60] is used. The numerical modelling takes into account the tensile loading, CP material models, geometry and material microstructural features such as texture and phase distribution. which will be discussed in the following sections.

5.2.2.1 Representative volume element

Bainitic steels have an multiphase microstructure although generally they are considered as a homogenous material in most macroscale material models. Representative volume element (RVE) approach [61] was employed and a geometry was generated from the actual microstructure of the B360-HT. This 2D RVE was created using EBSD data which can be seen in Figure 5.2. Using the information gained from the EBSD maps, grain orientation and phase distribution data were input into DAMASK.

Due to the very low fraction of retained austenite in the microstructure and its negligible effect on the deformation localization and strain partitioning in the microstructure the B360-HT is simplified as a homogeneous microstructure consisting of only bainitic ferrite (carbide free bainite). The negligible small effect of the retained

austenite on the strain localization and strain partitioning was confirmed by *in-situ* tests. This will be discussed in details in sections 5.2.3 and 5.3.2. This bainite is an aggregate of thin film retained austenite (TFRA) and bainitic ferrite. TFRA (between the bainite lamellas) however cannot be indexed in the EBSD because of its limit of spatial resolution but its existence is proved by transmission electron microscopy [62].

5.2.2.2 Crystal plasticity (CP) material model

Crystal plasticity defines the behavior of an individual crystal in a polycrystalline material which helps describe the mechanical behavior of the polycrystalline aggregate as a result from the interaction of these individual crystals. Using CP, the local stress and strain fields can be evaluated through numerical simulations which cannot be achieved experimentally. In the current work, strain partitioning in B360-HT was modelled using CP incorporating a fast Fourier transform solver (CPFFT) [63]. CP analysis considers the plastic deformation to be along certain directions on specific slip planes [64]. In this work, a phenomenological material model was employed [65] and the most important relations of this constitutive model are presented in the following paragraphs [64].

The deformation gradient $\boldsymbol{F}$ is multiplicatively decomposed into elastic and plastic parts:

$$\boldsymbol{F} = \boldsymbol{F}_e \boldsymbol{F}_p \tag{5.1}$$

where $\boldsymbol{F}_e$ is the elastic deformation gradient which considers the elastic distortion of the lattice and $\boldsymbol{F}_p$ is the plastic deformation gradient which considers the cumulative effect of dislocation motion on the active slip systems in the crystal.

The plastic deformation evolves as:

$$\dot{\boldsymbol{F}}_p = \boldsymbol{L}_p \boldsymbol{F}_p \tag{5.2}$$

The plastic velocity gradient $\boldsymbol{L}_p$ is presented as a sum of all shear slips on n slip systems:

$$\boldsymbol{L}_p = \sum_{\alpha=1}^{n} \dot{\gamma}^{\alpha} (\boldsymbol{m}^{\alpha} \otimes \boldsymbol{n}^{\alpha}) \tag{5.3}$$

where $\dot{\gamma}$ is the reference shear strain rate and α is the index for slip system and $\boldsymbol{m}^{\alpha}$ and $\boldsymbol{n}^{\alpha}$ are unit vectors which represent the slip direction and the normal to the slip plane, respectively.

Phenomenological power law uses the critical shear stress τ_c^{α} as state variable for each slip system α. The evolution of material state on slip system α is formulated as function of total shear γ and shear rate $\dot{\gamma}^{\alpha}$. The shear rate on each slip system is defined as follows:

$$\dot{\gamma}^{\alpha} = \dot{\gamma}_0 \text{sgn}\,(\tau^{\alpha})(\frac{|\tau^{\alpha}|}{R^{\alpha}})^{m} \tag{5.4}$$

where $\dot{\gamma}_0$ is reference shear rate, m is the strain rate exponent, τ^{α} is resolved shear stress (component of shear stress in the direction of slip) and R^{α} is current slip resistance of slip system α.

The resolved shear stress (on slip system α) is determined as follows:

$$\tau^{\alpha} = \boldsymbol{F}_e^T \boldsymbol{F}_e \boldsymbol{S}.(\boldsymbol{m}^{\alpha} \otimes \boldsymbol{n}^{\alpha}) \tag{5.5}$$

where $\boldsymbol{S}$ is the second Piola-Kirchhoff stress.

For metallic materials the elastic deformation is small, and equation (5.5) is usually approximated as:

$$\tau^{\alpha} = \boldsymbol{S}.(\boldsymbol{m}^{\alpha} \otimes \boldsymbol{n}^{\alpha}) \tag{5.6}$$

The slip resistance parameter τ_c^{α} is defined as follows:

$$\dot{R}^{\alpha} = \sum_{\alpha=1}^{n} \dot{\gamma}^{\alpha} h_0 \left|1 - \frac{R^{\alpha}}{R_S^{\alpha}}\right|^{a} \text{sgn}\left(1 - \frac{R^{\alpha}}{R_S^{\alpha}}\right) h_{\alpha\beta} \tag{5.7}$$

where R_S^{α} is the saturation slip resistance, h_0 is the initial hardening rate, $h_{\alpha\beta}$ is the interaction parameter which is the increase rate of deformation resistance on slip system α due to shearing on slip system β and a is a fitting parameter. In this formula, h_0, a, R_S^{α} are slip hardening parameters which are assumed to be the same for all slip systems.

5.2.2.3 Parameter calibration for the material model

In order to estimate the material model parameters for the aforementioned phenomenological material model, the stress-strain response from the macroscopic uniaxial tensile test on B360-HT was used [49]. An RVE was considered and the same load as the macroscopic tensile test was applied on it. The CP material model parameters were chosen so that the average response of the RVE fits with the one from the macroscopic tensile test.

In order to create the representative geometry and texture, a three dimensional Voronoi algorithm was applied for the simulations to determine the model parameters [66]. Using this algorithm a set of randomly distributed points are used in order to partition the space into regions called Voronoi cells. Suitable number of grains were chosen so that the different random texture of the microstructure does not have influence on the average response of the representative volume element. A uniaxial tensile strain rate of 6×10^{-4} s^{-1} was applied on the RVE with the size of 100×100×100 μm^3 and the resolution of 32×32×32.

The material model parameters include initial and saturation flow stresses (R_0^α, R_s^α) which influence mostly the yielding and ultimate strength and also the initial hardening rate (h_0) and hardening exponent (a) which control the hardening behavior.

The calibrated material parameters are presented in Table 5.2 and the resulting average stress-strain response from DAMASK simulation is compared with the uniaxial tensile experiment which is shown in Figure 5.3. These estimated material model parameters will be used to model the material behavior during the strain partitioning simulations of B360-HT (which will be discussed in section 5.3.1).

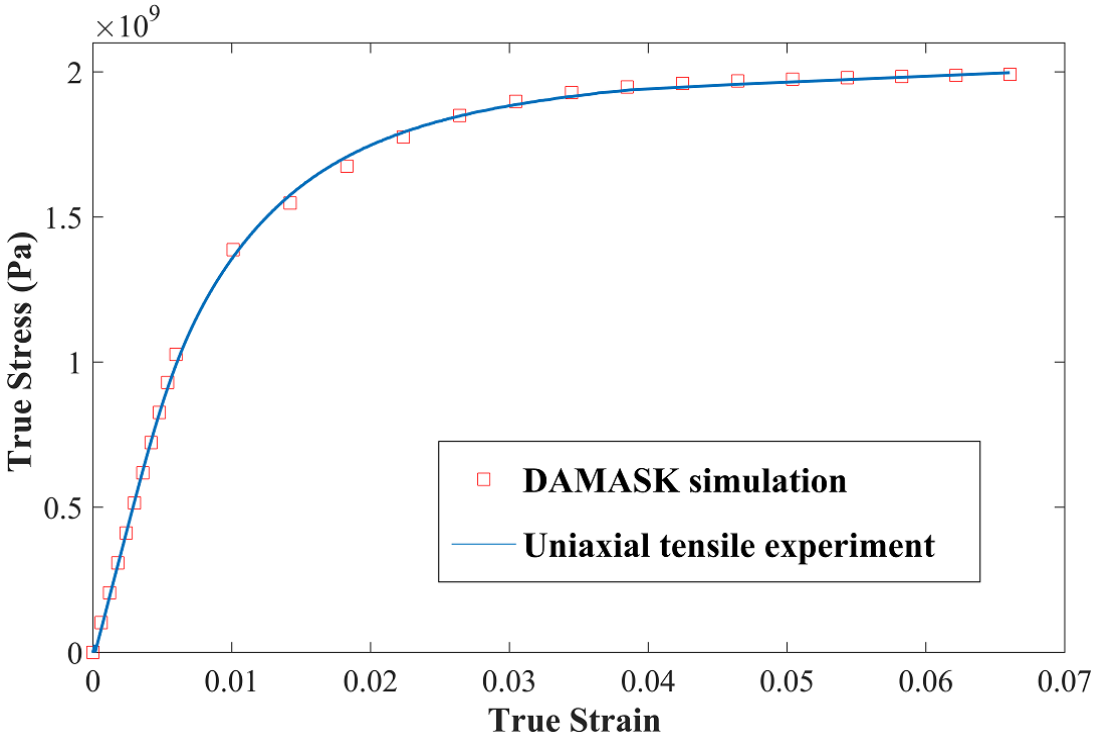

Figure 5.3. Comparison of tensile average stress-strain response (for the B360-HT bainitic steel) from DAMASK simulation with the uniaxial tensile experiment.

Table 5.2. The calibrated material model parameters for bainite used in phenomenological power law model.

Material parameters	Description	Value
C_{11}	Elastic constant	229.5 × 10^3 MPa
C_{12}	Elastic constant	98.4 × 10^3 MPa
C_{44}	Elastic constant	65.6 × 10^3 MPa
$\dot{\gamma}_0$	Reference shear strain rate	0.001 m s^{-1}
R_0^α	Initial slip resistance	610 MPa
R_s^α	Saturation slip resistance	820 MPa
h_0	Initial hardening rate	12000 MPa
$h_{\alpha\beta}$	Interaction parameter	1
m	Strain rate exponent	20
a	Hardening exponent	0.5

5.2.3 In-situ tensile experiments

Von Mises micro-strain partitioning in high strength carbide free bainitic B360-HT steel after an isothermal heat treatment was measured using *in-situ* tensile experiments [62]. Specimens with gauge dimensions of 1 mm × 0.5 mm × 0.5 mm were deformed in-situ up to 8% global strain [67]. Colloidal silica with 10-50 nm particle size was used for polishing the surfaces of specimen. Then the specimen was prepared using regular grinding, polishing and etching. The regions of interest (ROI) were identified using initial EBSD measurements and then was marked using focused ion beam (FIM) milling. In order to avoid ion beam damage the FIB markers were kept away from the corners of the ROI. Afterwards, a monolayer of SiO_2 particles was dispersed on the sample surface to measure the local strains in the in-situ μDIC tensile experiment. A KAMMRATH & WEISS stage inside the ZEISS Crossbeam XB 1540 microscope was used for the experiment. Tensile loading was applied on the specimens at a cross head speed of 3 μm/sec, which results in an initial strain rate of 6 × 10^{-4} s^{-1}. High resolution images were captured using In-lens secondary electron (SE) detector at 1.5 kV acceleration voltage. ARAMIS software (V6.3.0, GOM GmbH) with a facet size of 150 nm and facet overlap of 20% ~ 25% was used to analyse the von Mises strains from these recorded images. The results of this in-situ tensile experiment are discussed in section 5.3.2.

5.3 Results

5.3.1 Crystal plasticity (CP) simulation

B360-HT steel after isothermal heat treatment includes around 97.2% bainite and 2.8% BRA. The RVE was chosen as mentioned in section 5.2.2.1, single phase of bainite was considered and 2.8% of retained austenite was neglected since this small amount of stable retained austenite did not have significant influence on the experimental *in-situ* strain partitioning results (this will be further discussed in section 5.3.2). The tensile loading is applied with strain rate of 6×10^{-4} s^{-1} up to total strain of 8% in x-direction (Figure 5.4). The calibrated material model properties (Table 5.2) were assigned to the phenomenological material model. The simulation was performed on 2D RVE with the mentioned boundary conditions and local strain partitioning map was captured at 4% and 8% of global strain as illustrated in Figure 5.4(a), (b).

Various strain bands were formed oriented at 45° to the tensile axis with maximum von Mises strain observed in the bainitic laths oriented in the same direction. The maximum local von Mises strain captured in the simulations was 27.7% for 8% global strain. The locations with the highest localized strain is shown with solid-line arrows and the ones with moderately high strains with dashed-line arrows (Figure 5.4(b)). The distribution of the local strains is also shown in Figure 5.4(c) which approximately follows a log-normal distribution. The majority of the microstructure endures von Mises strains of 4% to 9%. The mean value of this distribution is 7.0% and the standard deviation 1.5%.

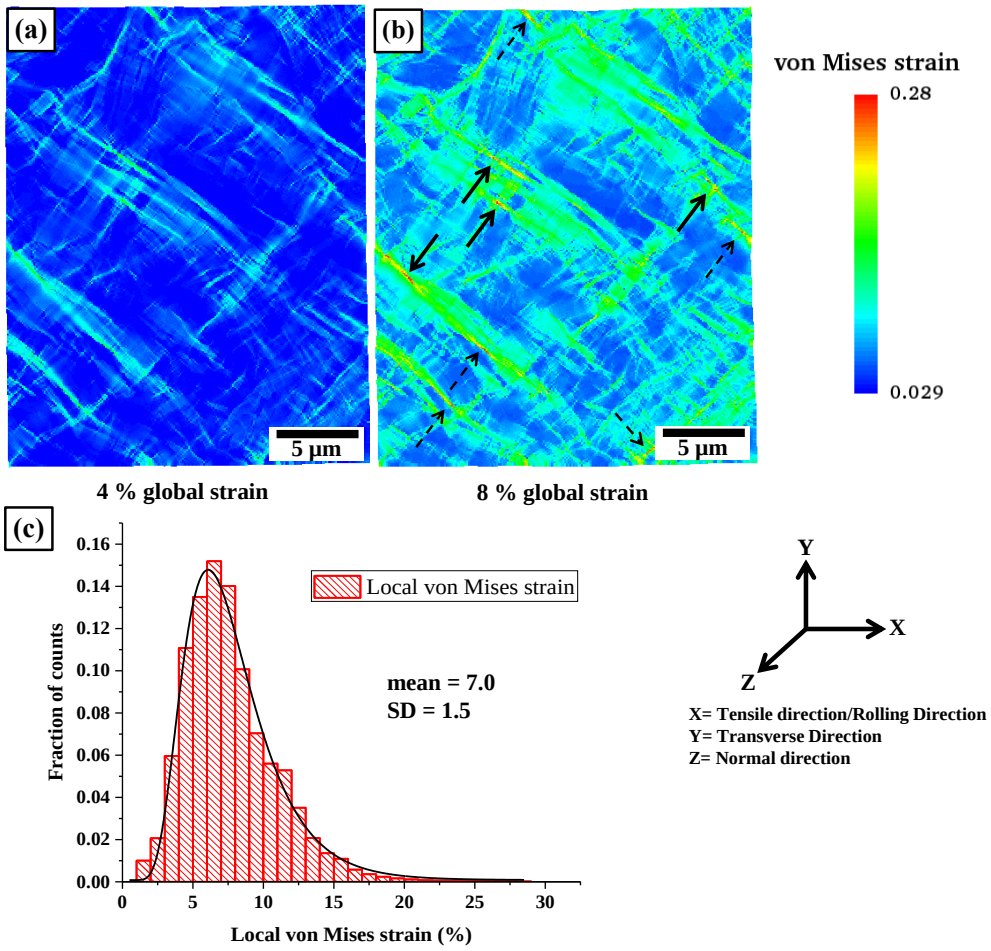

Figure 5.4. Von Mises strain partitioning in B360-HT resulted from DAMASK simulations, (a) von Mises strain partitioning at global strain of 4%, (b) von Mises strain partitioning at global strain of 8%, (c) the distribution of local von Mises strain at 8% tensile global strain.

5.3.2 Validation using in-situ µ-DIC tests

Micro-digital image correlation (µDIC) calculates the displacement fields and the resulting strain maps. Figure 5.5 shows the von Mises strain partitioning results after 4% and 8% global strain. The maximum von Mises strain observed at 8% global strain was 25% which compared well to the numerical estimation of 27.7%. Like in the CP simulation, strain bands form with orientation of 45° to the tensile axis. Maximum von Mises strain is observed in the bainitic laths oriented in the same direction. The severe strain concentration locations are shown in Figure 5.5(b) with black arrows and dashed black arrows indicate the moderate strain concentration locations. These locations could be possible candidates for initiation of cracks upon further increase of the load.

Numerical simulation could roughly approximate these locations (from the experiment), although some deviations were observed between the two methods. The strain distribution is shown in Figure 5.5(c). This distribution shows that the von Mises strain approximately follows a log-normal distribution function. The mean value of

this distribution is 7.3% (compared to the numerical results of 7.0%) with a standard deviation of 1.4%.

The numerical simulation shows a satisfactory correlation with the *in-situ* test results. A few deviations are observed between the experimental and simulation strain partitioning data. This can be because of the approximation of a 2D geometry for a 3D phenomenon, i.e. the texture and phase distribution from the layers above and below this 2D layer were neglected by using a 2D model. The 2.8% of retained austenite present in the microstructure didn't have significant influence in the strain partitioning results. By analyzing the locations around retained austenite blocks, it was shown that there was no clear indication of strain localization in the vicinity of this constituent. This is the reason why retained austenite blocks were neglected in the numerical modelling and were considered as bainite.

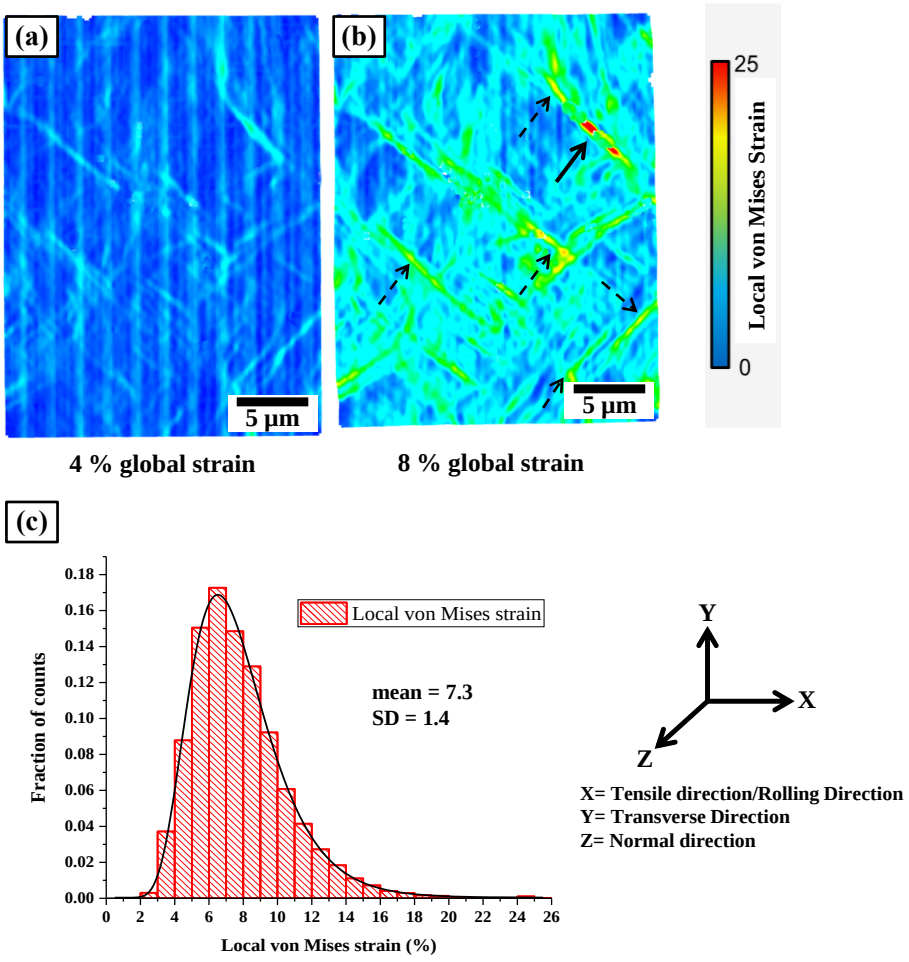

Figure 5.5. *In-situ* tensile experiments results on B360-HT, (a) DIC results of von Mises strain partitioning at global strain of 4%, (b) DIC results of von Mises strain partitioning at global strain of 8%, (c)The distribution of local von Mises strain at 8% tensile strain.

5.4 Discussion

The heterogeneous local strain distribution in high strength carbide free bainitic steel (CFBS) after a proposed heat treatment (B360-HT) was characterized experimentally using *in-situ* tensile tests [62] and numerically, using the crystal plasticity (CP) numerical modelling. The resulting numerical strain map and the strain localization at certain global strain are predicted well by the numerical simulations. The strain bands which form at an angle of 45° to the tensile axis were observed in both numerical simulations and experimental *in-situ* tests. The maximum von Mises strain of 25% at 8% global strain was predicted numerically within 10% error.

This study was performed as a continuation of another study which investigated the strain partitioning and damage initiation in a continuously cooled CFBS (B360-AR) [56,62]. Comparing the results of this study with the previous one shows that both the numerical simulations and the experiments show a less severe strain partitioning after using an isothermal heat treatment process. One of the reasons for this improvement is that the isothermal heat treatment eliminates the formation of relatively large martensitic islands in the microstructure. During continuous cooling the big part of large and unstable blocky austenite in the B360-AR microstructure transforms into martensite [56,67]. Due to more complete transformation during isothermal heat treatment (compared to continuous cooling), large retained austenite islands do not occur and instead, smaller blocky retained austenite (BRA) is present in the microstructure, which are more carbon rich and therefore more mechanically and thermally stable. Another reason is that, during isothermal heat treatment the microstructure is very fine bainite (lower bainite) with better mechanical properties (strength-toughness balance) compared to the continuously cooled as-received bainitic steel (B360-AR). In the continuously cooled rails the microstructure contains coarse bainite which is a combination of upper and lower bainite [49]. These are the main reasons behind better performance of the high strength CFBS after isothermal heat treatment (B360-HT).

The numerical simulation using CP material models available in DAMASK enables sufficiently accurate prediction of the strain partitioning in the microstructure. This saves time and costs by replacing the time consuming *in-situ* tensile tests with CP numerical simulations for a variety of microstructures of not only bainitic steels and but also other types of steels.

Using the information gained from strain partitioning analysis, the possible microstructural features which could later initiate damage in the steel are investigated and reported. However, we should take into account that damage is not just a matter of the highest strain, but strain in combination with microstructure. This means the areas of high strain localization can be judged as possible damage initiation areas and not necessarily the exact damage initiating locations.

Comparing the strain maps obtained from simulation and in-situ experiment, we observe that the locations with high local strain have some deviations between the two methods; this could be due to the 2D modelling of the 3D phenomenon. The realistic phenomena of strain partitioning happens in 3D with strain paths in three dimensions, which would result in lower stress and strain localizations compared to the 2D simulation in DAMASK (which is using a columnar grain structure) with strain paths happening in two dimensions. This could be the reason behind the slightly higher local strains captured from the numerical simulation. On the other hand, this could influence the locations of these high strain localizations. The effect of the grains below and above a certain location in the 2D-RVE was neglected in the 2D simulation while this could influence the strain localization at that certain location.

In order to have a better estimation of the micromechanical strain partitioning, the numerical simulations must have a good accuracy. The accuracy of the simulations relies on the accuracy of geometry, i.e. good imaging tools to reflect more details of the real microstructure (phase morphologies, texture, etc.). Additionally the accuracy of material model parameters (mechanical properties and damage characteristics) should be considered with a reasonable accuracy. More detailed representation of the carbide-free bainitic microstructure (by using a higher resolution imaging) which is a lamellar (composite) structure of bainitic ferrite and austenite could result in more accurate strain partitioning and damage initiation characterization. Using a 3D-RVE could capture more details of the damage initiation happening in the microstructure. In order to capture the mechanical behavior of the different phases accurately, recently nano-indentation experiments were successfully performed [26] which could help capturing the phase properties with an improved accuracy.

Hence as recommendation for future work and to achieve a more realistic damage initiation analysis in steels, there is a need of more detailed geometrical modelling such as three dimensional model instead of two dimensional simplification and also better imaging resolution to include more microstructural features such as the lath structure. More detailed microstructure geometry requires accurate material model parameter calibration for different phases/constituents in the microstructure. Mechanical properties such as initial and saturation flow stress, hardening behavior as well as damage properties are captured more accurately using more advanced methods such as nano-indentation experiments. Using these recommendations, the models could reflect more details of what is happening in the reality which leads to material damage and failure.

5.5 Summary and conclusions

The strain partitioning in high strength CFBS after isothermal heat treatment (B360-HT) was simulated and compared with the results of *in-situ* experimental tensile tests. The results show a good correlation between the experimental and numerical results.

1. The start of strain localization and the strain bands, was predicted by the model and observed experimentally at 45° with respect to the tensile axis.
2. These strain localizations create locations with high von Mises strain, which can be initiation points for damage at higher strain. These locations were also predicted reasonably by the numerical simulations.
3. The low amount of stable retained austenite had negligible influence on this observed strain localization. The von Mises strain distribution is also predicted well by the numerical simulations in the microstructure and the maximum von Mises strain is predicted around 27.7% compared to the 25% resulted from *in-situ* experiments (9.7% error). However the exact locations of these strain localizations captured in the simulations have some deviation from the experimental results which could be the result of geometrical simplifications (2D model instead of a 3D RVE).
4. The combination of numerical and experimental methods used in this work provides valuable information regarding damage initiation in high strength isothermally transferred CFBS B360-HT.

5.6 References

[1] P. Clayton, M.B.P. Allery, Metallurgical Aspects of Surface Damage Problems in Rails, Can. Metall. Q. 21 (1982) 31–46. https://doi.org/10.1179/cmq.1982.21.1.31.

[2] R.P.B.J. Dollevoet, Design of an anti head check profile based on stress relief, University of Twente, 2010. https://doi.org/10.3990/1.9789036530736.

[3] R. Dollevoet, Z. Li, O. Arias-Cuevas, A Method for the Prediction of Head Checking Initiation Location and Orientation under Operational Loading Conditions, Proc. Inst. Mech. Eng. Part F J. Rail Rapid Transit. 224 (2010) 369–374. https://doi.org/10.1243/09544097JRRT368.

[4] Z. Li, X. Zhao, C. Esveld, R. Dollevoet, M. Molodova, An investigation into the causes of squats-Correlation analysis and numerical modeling, Wear. 265 (2008) 1349–1355. https://doi.org/10.1016/j.wear.2008.02.037.

[5] P.J. Bolton, P. Clayton, Rolling—sliding wear damage in rail and tyre steels, Wear. 93 (1984) 145–165. https://doi.org/10.1016/0043-1648(84)90066-8.

[6] W.J. Jiang, C. Liu, C.G. He, J. Guo, W.J. Wang, Q.Y. Liu, Investigation on impact

wear and damage mechanism of railway rail weld joint and rail materials, Wear. 376–377 (2017) 1938–1946. https://doi.org/10.1016/j.wear.2017.02.035.

[7] R. Lewis, R.S. Dwyer-Joyce, Wear mechanisms and transitions in railway wheel steels, Proc. Inst. Mech. Eng. Part J J. Eng. Tribol. 218 (2004) 467–478. https://doi.org/10.1243/1350650042794815.

[8] K.M. Lee, A.A. Polycarpou, Wear of conventional pearlitic and improved bainitic rail steels, Wear. 259 (2005) 391–399. https://doi.org/10.1016/j.wear.2005.02.058.

[9] R. Devanathan, P. Clayton, Rolling-sliding wear behavior of three bainitic steels, Wear. 151 (1991) 255–267. https://doi.org/10.1016/0043-1648(91)90253-Q.

[10] H.A. Aglan, Z.Y. Liu, M.F. Hassan, M. Fateh, Mechanical and fracture behavior of bainitic rail steel, J. Mater. Process. Technol. 151 (2004) 268–274. https://doi.org/10.1016/j.jmatprotec.2004.04.073.

[11] K.-H. Kim, J.-S. Lee, On microstructure and properties of Si modified 100Cr6 bearing steels, Mater. Sci. Technol. 28 (2012) 50–54. https://doi.org/10.1179/1743284711Y.0000000053.

[12] X. Gui, K. Wang, G. Gao, R.D.K. Misra, Z. Tan, B. Bai, Rolling contact fatigue of bainitic rail steels: The significance of microstructure, Mater. Sci. Eng. A. 657 (2016) 82–85. https://doi.org/10.1016/j.msea.2016.01.052.

[13] Y. Wang, F. Zhang, Z. Yang, B. Lv, C. Zheng, Rolling contact fatigue performances of carburized and high-C nanostructured bainitic steels, Materials (Basel). 9 (2016) 1–12. https://doi.org/10.3390/ma9120960.

[14] T. Teeri, C. Garcia-Mateo, E. Vuorinen, T. Sourmail, F.G. Caballero, V. Smanio, R. Elvira, A. Leiro, C. Ziegler, M. Kuntz, Evaluation of potential of high Si high C steel nanostructured bainite for wear and fatigue applications, Mater. Sci. Technol. 29 (2013) 1166–1173. https://doi.org/10.1179/1743284713y.0000000242.

[15] X.Y. Feng, F.C. Zhang, J. Kang, Z.N. Yang, X.Y. Long, Sliding wear and low cycle fatigue properties of new carbide free bainitic rail steel, Mater. Sci. Technol. 30 (2014) 1410–1418. https://doi.org/10.1179/1743284713y.0000000474.

[16] M.J. Peet, P. Hill, M. Rawson, S. Wood, H.K.D.H. Bhadeshia, Fatigue of extremely fine bainite, Mater. Sci. Technol. 27 (2010) 119–123. https://doi.org/10.1179/026708310x12688283410244.

[17] J. Zhao, H. Ji, T. Wang, High-cycle, push-pull fatigue fracture behavior of high-C, Si-Al-rich nanostructured bainite steel, Materials (Basel). 11 (2017). https://doi.org/10.3390/ma11010054.

[18] T.S. Wang, J. Yang, C.J. Shang, X.Y. Li, B. Lv, M. Zhang, F.C. Zhang, Sliding friction surface microstructure and wear resistance of 9SiCr steel with low-

temperature austempering treatment, Surf. Coatings Technol. 202 (2008) 4036–4040. https://doi.org/10.1016/j.surfcoat.2008.02.013.

[19] P. Zhang, F.C. Zhang, Z.G. Yan, T.S. Wang, L. Qian, Wear property of low-temperature bainite in the surface layer of a carburized low carbon steel, 2011. https://doi.org/10.1016/j.wear.2010.12.025.

[20] A. Leiro, A. Kankanala, E. Vuorinen, B. Prakash, Tribological behaviour of carbide-free bainitic steel under dry rolling/sliding conditions, 2011. https://doi.org/10.1016/j.wear.2011.03.025.

[21] J. Yang, T.S. Wang, B. Zhang, F. C. Zhang, Sliding wear resistance and worn surface microstructure of nanostructured bainitic steel, Wear. s 282–283 (2012) 81–84. https://doi.org/10.1016/j.wear.2012.02.008.

[22] A. Leiro, E. Vuorinen, K.G. Sundin, B. Prakash, T. Sourmail, V. Smanio, F.G. Caballero, C. Garcia-Mateo, R. Elvira, Wear of nano-structured carbide-free bainitic steels under dry rolling–sliding conditions, Wear. 298–299 (2012) 42–47. https://doi.org/10.1016/j.wear.2012.11.064.

[23] D.V.E. H. K. D. H. Bhadeshia, Bainite in Silicon Steels New Composition - Property Approach Part 1 .Pdf, Met. Sci. 17 (1983) 411–419.

[24] X.Y. Long, J. Kang, B. Lv, F.C. Zhang, Carbide-free bainite in medium carbon steel, Mater. Des. 64 (2014) 237–245. https://doi.org/10.1016/j.matdes.2014.07.055.

[25] Y.H. Wang, F.C. Zhang, T.S. Wang, A novel bainitic steel comparable to maraging steel in mechanical properties, Scr. Mater. 68 (2013) 763–766. https://doi.org/10.1016/j.scriptamat.2012.12.031.

[26] C.C. Tasan, J.P.M. Hoefnagels, M. Diehl, D. Yan, F. Roters, D. Raabe, Strain localization and damage in dual phase steels investigated by coupled in-situ deformation experiments and crystal plasticity simulations, Int. J. Plast. 63 (2014) 198–210. https://doi.org/10.1016/j.ijplas.2014.06.004.

[27] K. Alharbi, H. Ghadbeigi, P. Efthymiadis, M. Zanganeh, S. Celotto, R. Dashwood, C. Pinna, Damage in dual phase steel DP1000 investigated using digital image correlation and microstructure simulation, Model. Simul. Mater. Sci. Eng. 23 (2015). https://doi.org/10.1088/0965-0393/23/8/085005.

[28] N. Fujita, N. Ishikawa, F. Roters, C.C. Tasan, D. Raabe, Experimental-numerical study on strain and stress partitioning in bainitic steels with martensite-austenite constituents, Int. J. Plast. 104 (2018) 39–53. https://doi.org/10.1016/j.ijplas.2018.01.012.

[29] C.C. Tasan, M. Diehl, D. Yan, C. Zambaldi, P. Shanthraj, F. Roters, D. Raabe, Integrated experimental-simulation analysis of stress and strain partitioning in multiphase alloys, Acta Mater. 81 (2014) 386–400.

https://doi.org/10.1016/j.actamat.2014.07.071.

[30] J. Kang, Y. Ososkov, J.D. Embury, D.S. Wilkinson, Digital image correlation studies for microscopic strain distribution and damage in dual phase steels, Scr. Mater. 56 (2007) 999–1002. https://doi.org/10.1016/j.scriptamat.2007.01.031.

[31] C.C. Tasan, J.P.M. Hoefnagels, M.G.D. Geers, Microstructural Banding Effects Clarified Through Micrographic Digital Image Correlation, Scr. Mater. 62 (2010) 835–838. https://pure.mpg.de/pubman/item/item_2015292_2 (accessed November 15, 2018).

[32] H. Ghadbeigi, C. Pinna, S. Celotto, J.R. Yates, Local plastic strain evolution in a high strength dual-phase steel, Mater. Sci. Eng. A. 527 (2010) 5026–5032. https://doi.org/10.1016/j.msea.2010.04.052.

[33] M. Kapp, T. Hebesberger, O. Kolednik, A micro-level strain analysis of a high-strength dual-phase steel, Int. J. Mat. Res. 102 (2011) 687–691.

[34] J. Marteau, H. Haddadi, S. Bouvier, Investigation of Strain Heterogeneities Between Grains in Ferritic and Ferritic-Martensitic Steels, Exp. Mech. 53 (2013) 427–439. https://doi.org/10.1007/s11340-012-9657-6.

[35] U. Liedl, S. Traint, E.A. Werner, An unexpected feature of the stress–strain diagramof dual-phase steel, 25 (2002) 122–128.

[36] J. Kadkhodapour, S. Schmauder, D. Raabe, S. Ziaei-Rad, U. Weber, M. Calcagnotto, Experimental and numerical study on geometrically necessary dislocations and non-homogeneous mechanical properties of the ferrite phase in dual phase steels, Acta Mater. 59 (2011) 4387–4394. https://doi.org/10.1016/j.actamat.2011.03.062.

[37] J. Kadkhodapour, A. Butz, S. Ziaei-Rad, S. Schmauder, A micro mechanical study on failure initiation of dual phase steels under tension using single crystal plasticity model, Int. J. Plast. 27 (2011) 1103–1125. https://doi.org/10.1016/j.ijplas.2010.12.001.

[38] K.S. Choi, W.N. Liu, X. Sun, M.A. Khaleel, Microstructure-based constitutive modeling of TRIP steel: Prediction of ductility and failure modes under different loading conditions, Acta Mater. 57 (2009) 2592–2604. https://doi.org/10.1016/j.actamat.2009.02.020.

[39] F. Delaire, J.L. Raphanel, C. Rey, Plastic heterogeneities of a copper multicrystal deformed in uniaxial tension: Experimental study and finite element simulations, Acta Mater. 48 (2000) 1075–1087. https://doi.org/10.1016/S1359-6454(99)00408-5.

[40] D. Raabe, M. Sachtleber, Z. Zhao, F. Roters, S. Zaefferer, Micromechanical and macromechanical effects in grain scale polycrystal plasticity experimentation

and simulation, Acta Mater. 49 (2001) 3433–3441. https://doi.org/10.1016/S1359-6454(01)00242-7.

[41] Z. Zhao, M. Ramesh, D. Raabe, A.M. Cuitiño, R. Radovitzky, Investigation of three-dimensional aspects of grain-scale plastic surface deformation of an aluminum oligocrystal, Int. J. Plast. 24 (2008) 2278–2297. https://doi.org/10.1016/j.ijplas.2008.01.002.

[42] X. Sun, K.S. Choi, A. Soulami, W.N. Liu, M.A. Khaleel, On key factors influencing ductile fractures of dual phase (DP) steels, Mater. Sci. Eng. A. 526 (2009) 140–149. https://doi.org/10.1016/j.msea.2009.08.010.

[43] X. Sun, K.S. Choi, W.N. Liu, M.A. Khaleel, Predicting failure modes and ductility of dual phase steels using plastic strain localization, Int. J. Plast. 25 (2009) 1888–1909. https://doi.org/10.1016/j.ijplas.2008.12.012.

[44] L. Wang, R.I. Barabash, Y. Yang, T.R. Bieler, M.A. Crimp, P. Eisenlohr, W. Liu, G.E. Ice, Experimental characterization and crystal plasticity modeling of heterogeneous deformation in polycrystalline α-Ti, Metall. Mater. Trans. A Phys. Metall. Mater. Sci. 42 (2011) 626–635. https://doi.org/10.1007/s11661-010-0249-8.

[45] S.-H. Choi, E.-Y. Kim, W. Woo, S.H. Han, J.H. Kwak, The effect of crystallographic orientation on the micromechanical deformation and failure behaviors of DP980 steel during uniaxial tension, 45 (2013) 85–102. https://doi.org/10.1016/j.ijplas.2012.11.013.

[46] D. Cédat, O. Fandeur, C. Rey, D. Raabe, Polycrystal model of the mechanical behavior of a Mo-TiC30vol.% metal-ceramic composite using a 3D microstructure map obtained by a dual beam FIB-SEM, Acta Mater. 60 (2012) 1623–1632.

[47] G. Martin, C.W. Sinclair, R.A. Lebensohn, Microscale plastic strain heterogeneity in slip dominated deformation of magnesium alloy containing rare earth, Mater. Sci. Eng. A. 603 (2014) 37–51. https://doi.org/10.1016/j.msea.2014.01.102.

[48] H. Lim, J.D. Carroll, C.C. Battaile, T.E. Buchheit, B.L. Boyce, C.R. Weinberger, Grain-scale experimental validation of crystal plasticity finite element simulations of tantalum oligocrystals, Int. J. Plast. 60 (2014) 1–18. https://doi.org/10.1016/j.ijplas.2014.05.004.

[49] O. Hajizad, A. Kumar, Z. Li, R.H. Petrov, J. Sietsma, R. Dollevoet, Influence of Microstructure on Mechanical Propertiesof Bainitic Steels in Railway Applications, Metals (Basel). 9 (2019) 778. https://doi.org/https://doi.org/10.3390/met9070778.

[50] H.K.D.H. Bhadeshia, Nanostructured bainite, Proc. R. Soc. A Math. Phys. Eng. Sci. 466 (2010) 3–18. https://doi.org/10.1098/rspa.2009.0407.

[51] H.K.D.H. Bhadeshia, The first bulk nanostructured metal, Sci. Technol. Adv. Mater. 14 (2013). https://doi.org/10.1088/1468-6996/14/1/014202.

[52] F.G. Caballero, C. Garcia-Mateo, M.K. Miller, Design of novel bainitic steels: Moving from ultrafine to nanoscale structures, Jom. 66 (2014) 747–755. https://doi.org/10.1007/s11837-014-0908-0.

[53] H.K.D.H. Bhadeshia, D. V. Edmonds, The bainite transformation in a silicon steel, Metall. Trans. A. 10 (1979) 895–907. https://doi.org/10.1007/BF02658309.

[54] E. Kozeschnik, H.K.D.H. Bhadeshia, Influence of silicon on cementite precipitation in steels, Mater. Sci. Technol. 24 (2008) 343–347. https://doi.org/10.1179/174328408x275973.

[55] J. Zhu, X. Sun, G. Barber, H. Qin, Effect of Carbon Content on Bainite Transformation Kinetics and Microstructure of 4140 / 4150 Steels, 15 (2019) 518–535. https://doi.org/10.19044/esj.2019.v15n9p518.

[56] O. Hajizad, A. Kumar, Z. Li, R.H. Petrov, J. Sietsma, R. Dollevoet, Strain partitioning and damage initiation in a continuously cooled carbide free bainitic steel [Unpublished manuscript], (n.d.).

[57] H.K.D.H. Bhadeshia, J.W. Christian, Bainite in steels, Metall. Trans. A. 21 (1990) 767–797. https://doi.org/10.1007/BF02656561.

[58] A.S. Podder, I. Lonardelli, A. Molinari, H.K.D.H. Bhadeshia, Thermal stability of retained austenite in bainitic steel: An in situ study, Proc. R. Soc. A Math. Phys. Eng. Sci. 467 (2011) 3141–3156. https://doi.org/10.1098/rspa.2011.0212.

[59] C. García-Mateo, F.G. Caballero, The role of retained austenite on tensile properties of steels with bainitic microstructures, Mater. Trans. 46 (2005) 1839–1846. https://doi.org/10.2320/matertrans.46.1839.

[60] F. Roters, P. Eisenlohr, C. Kords, D.D. Tjahjanto, M. Diehl, D. Raabe, DAMASK: the Düsseldorf Advanced MAterial Simulation Kit for studying crystal plasticity using an FE based or a spectral numerical solver, Procedia IUTAM. 3 (2012) 3–10. https://doi.org/10.1016/j.piutam.2012.03.001.

[61] R. Hill, Elastic properties of reinforced solids: Some theoretical principles, J. Mech. Phys. Solids. 11 (1963) 357–372. https://doi.org/10.1016/0022-5096(63)90036-X.

[62] A. Kumar, S.K. Makineni, A. Dutta, C. Goulas, M. Steenbergen, R.H. Petrov, J. Sietsma, Design of high-strength and damage-resistant carbide-free fine bainitic steels for railway crossing applications, Mater. Sci. Eng. A. (2019). https://doi.org/10.1016/j.msea.2019.05.043.

[63] R.A. Lebensohn, A.D. Rollett, P. Suquet, Fast fourier transform-based modeling for the determination of micromechanical fields in polycrystals, Jom. 63 (2011)

13–18. https://doi.org/10.1007/s11837-011-0037-y.

[64] F. Roters, P. Eisenlohr, L. Hantcherli, D.D. Tjahjanto, T.R. Bieler, D. Raabe, Overview of constitutive laws, kinematics, homogenization and multiscale methods in crystal plasticity finite-element modeling: Theory, experiments, applications, Acta Mater. 58 (2010) 1152–1211. https://doi.org/10.1016/j.actamat.2009.10.058.

[65] D. Peirce, R.J. Asaro, A. Needleman, An analysis of nonuniform and localized deformation in ductile single crystals, Acta Metall. 30 (1982) 1087–1119. https://doi.org/10.1016/0001-6160(82)90005-0.

[66] G. Voronoi, Nouvelles applications des paramètres continus à la théorie des formes quadratiques. Deuxième mémoire. Recherches sur les parallélloèdres primitifs., J. Für Die Reine Und Angew. Math. 134 (1908) 198–287. http://eudml.org/doc/149291.

[67] A. Kumar, A. Dutta, S.K. Makineni, M. Herbig, R.H. Petrov, J. Sietsma, In-situ observation of strain partitioning and damage development in continuously cooled carbide-free bainitic steels using micro digital image correlation, Mater. Sci. Eng. A. 757 (2019) 107–116. https://doi.org/10.1016/j.msea.2019.04.098.

6 Conclusion and recommendation for future work

The complex loading condition on the rails during wheel-rail contact (and especially the crossing nose due to the impact loading) makes it quite complicated to analyse the damage phenomena which is a combination of RCF and wear. Von Mises stress theory mentions that a ductile material yields when the elastic energy of distortion per unit volume reaches a critical value called distortion energy per unit volume, which is dependent on yield strength of the material. By using this theory and in order to find a suitable material for such complex loading, simple uniaxial tensile tests were performed. Hardness is another important material property when it comes to wear and RCF damage investigation.

In this work a combination of tensile experiments and hardness measurements were used to capture yield and ultimate strength, fracture strain, toughness, strain hardening and hardness. Then with the help of microscopy, the influence of the microstructure on these properties were investigated and finally a suitable steel for further analysis was chosen. Then, the strain localization which is a measure of damage initiation was further studied using a combination of micromechanical modelling and *in-situ* tensile experiments. Using the information gained from these studies, a modified microstructure (using a proposed heat treatment) was recommended to be used in the Dutch railway network (with especial focus on crossing nose).

The conclusions from these analysis are listed below:

- The bainitic steels perform better than the pearlitic R350HT steel regarding tensile strength, ductility and hardness.
- By using low bainitic transformation temperature and providing enough time, nearly complete bainitic transformation can be resulted which means finer bainitic microstructure with smaller-size blocky retained austenite (BRA), with almost no martensite. This results in better mechanical properties.
- Isothermal heat treatment on B1400-HT and CrB-HT bainitic grades results in smaller size of carbides (in comparison to the as-received steel), which are closely

placed to each other (mainly inside the bainite laths). This helps achieve higher yield strength in heat-treated grades compared to as-received steels.

- The hardness of bainitic steels increases with the suitable heat treatment because of larger fraction of lower bainite, which is finer therefore stronger and harder than upper bainite.
- Bainitic B360 steel after the isothermal heat treatment has the highest strength, ductility and toughness among all the steels. This is due to the absence of carbides and martensite, formation of fine bainitic microstructure and smaller homogeneously distributed BRA.
- The partitioning of the local strain in the microstructure and its interaction with the microstructural features gives valuable information regarding damage initiation of steels. Hence, strain partitioning in the steel microstructure was used to investigate the damage initiation characteristics of the carbide free bainitic steel (B360).
- In order to investigate the microscopic damage initiation in steels, numerical modelling was used. A realistic Representative Volume Element (RVE) captured using EBSD was employed to represent the microstructure of the steel.
- Two different numerical models were used: A von Mises plastic finite element model (VPFEM) using Abaqus and a phenomenological crystal plasticity with a fast Fourier transfer solver (CPFFT) utilizing DAMASK.
- Although there were some deviations between the simulation results and the experiment, both simulations give reasonable estimation of the strain localization map and distribution and also the maximum local strain concentration.
- CPFFT model gives better estimation of the local strain partitioning (than VPFEM model) in reference to the *in-situ* experiments.
- In order to increase the accuracy of numerical models, there is a need for more accurate geometry (considering a three dimensional (3D) geometry instead of a two dimensional (2D) one) and precise material behaviour modelling. More accurate material characterization for each phase can be achieved by using more advanced methods such as nano-indentation.
- Factors such as martensite/bainitic ferrite interfaces, interface orientation with respect to tensile direction, spatial distribution of phases, phase fraction and morphology influence the strain partitioning and damage initiation in the carbide free bainitic B360 steel.
- However, the main damage mechanism in this steel is strain localization in the narrow channels of bainite which are located in between the martensitic islands and in the interfaces of bainite with martensite. During the application of higher loads, these high strain localizations in combination with microstructural features could create voids and eventually cracks leading to the fracture of martensitic islands.
- Isothermal heat treatment helps to eliminate the large BRA and the martensitic islands. During this heat treatment, the samples are first heated up to 900 °C (for 10

minutes), then transferred to a salt bath (with temperature 330 ˚C and held for 60 minutes) and subsequently quenched in oil.

- The strain partitioning analysis performed on the B360 after isothermal heat treatment (B360-HT) shows much less strain localization in this steel compared to one prior to the isothermal heat treatment.
- Numerical modeling with a phenomenological crystal plasticity material model, gives good estimation of the von Mises strain distribution in the microstructure of B360-HT.
- Strain bands in this steel mainly form in 45° to the tensile axis and create high local strain which could later start cracks.
- The maximum von Mises strain was predicted around 27.7% compared to the 25% from the in-situ experiments (9.7% error).
- The exact locations of some these strain localizations captured in the simulations deviate from the experimental results, which could be due to geometrical simplifications (2D RVE instead of a 3D one).
- For future work there is a need of more accurate geometrical modelling such as 3D model instead of 2D RVE, which could also benefit from better imaging resolution in order to include more microstructural features such as the lath structure of the bainite.
- Using a more accurate technique such as nano-indentation in order to capture the mechanical properties of the bainite (which is a composite microstructure of bainitic ferrite and thin film retained austenite) could also help for improving the accuracy of the numerical modelling.
- Using these recommendations, the models could reflect more details of what is happening in the reality which leads to material damage and failure.
- For the future research, the damage propagation (after being initiated) should be investigated as well. The crack growth rate which depends on material properties such as fracture toughness gives a good estimate of how the crack will evolve in near future. This would help designing a more efficient railway maintenance schedules.
- More field or laboratory tests must be performed on the proposed B360-HT steel in order to validate the results of this research in realistic working condition.

7 Curriculum Vitæ

Omid Hajizad

14, October, 1986 — Born in Urmia, Iran

Education

May, 2014 - Feb, 2019 — **PhD candidate**
Technical University of Delft (TUD), Delft, Netherlands
Railway Group, Civil Engineering and Geosciences Department
Project topic: "The interaction between macroscopic loading modes and micro-scale mechanisms in railway switches"
Promoters: Prof. Zili Li, Prof. Rolf Dollevoet

September 2013 — **M.Sc. in Computational Mechanics**
Technical University of Munich (TUM), Munich, Germany
Thesis topic: "Evaluation of Different Modeling Approaches for Process Induced Deformations (PID) due to Tool Part Interaction (TPI) during Composite Processing"

September 2010 — **B.Sc. in Mechanical Engineering**
Sharif University of Technology (SUT), Tehran, Iran
Thesis topic: "Numerical Simulation for Energy Absorption of Monolithic and Double-Layered Steel Plates under normal and inclined Impact"

8 Scientific Publications

O. Hajizad, A. Kumar, Z. Li, R. H. Petrov, J. Sietsma, R. Dollevoet, Influence of Microstructure on Mechanical Properties of Bainitic Steels in Railway Applications. *Metals* **2019**, *9*, 778.

O. Hajizad, A. Kumar, Z. Li, R. H. Petrov, J. Sietsma, R. Dollevoet, Strain partitioning and damage initiation in a continuously cooled carbide free bainitic steel. Submitted for publication.

O. Hajizad, A. Kumar, Z. Li, R. H. Petrov, J. Sietsma, R. Dollevoet, Crystal plasticity modelling of strain partitioning in high strength carbide free bainitic steel and validation using in-situ tensile experiment. Submitted for publication.